

Linköping Studies in Science and Technology
Dissertation No. 1452

Theoretical Descriptions of Complex Magnetism in Transition Metals and Their Alloys

Marcus Ekholm



Linköpings universitet
INSTITUTE OF TECHNOLOGY

Department of Physics, Chemistry and Biology (IFM)
Linköping University, SE-581 83 Linköping, Sweden

Linköping 2012

ISBN 978-91-7519-885-9
ISSN 0345-7524

Printed by LiU-Tryck, Linköping 2012

Большое спасибо

Abstract

In this thesis, various methods for studying solids by simulations of quantum-mechanical equations, have been applied to transition metals and their alloys. Transition metals such as Fe, Ni, and Mn, are not only cornerstones in modern technology, but also key components in the very fabric of the Earth interior. Such systems show highly complex magnetic properties. As shown within this thesis, to understand and predict their properties from a microscopic level, is still a highly demanding task for the the quantum theory of solids. This is especially crucial at elevated temperature and pressure.

It is found that the magnetic degrees of freedom are inseparable from the structural, elastic and chemical properties of such alloy systems. This requires theoretical descriptions capable of handling this interplay. Such schemes are discussed and demonstrated.

Furthermore, the importance of the description of Coulomb correlation effects is demonstrated by DFT calculations and also by going beyond the one-electron description by the LDA+DMFT method.

It is also shown how magnetic interactions in the half-metallic compound NiMnSb can be manipulated by alloying. The stability of these alloys is also evaluated in calculations, and verified by experimental synthesis at ambient conditions.

Populärvetenskaplig sammanfattning

Denna avhandling handlar om teoretiska metoder för att beräkna strukturella, kemiska och magnetiska egenskaper hos fasta material — i synnerhet övergångsmetallerna, såsom järn, nickel och mangan, samt legeringar mellan dessa. Den teknologiska betydelsen av dessa metaller kan knappast överskattas.

Beräkningar av det slag som behandlas kallas *grundprincipsbereäkningar*, eftersom de utgår ifrån de mest grundläggande egenskaper hos de ingående atomerna. Den mest framgångsrika teorin för hur atomer och elektroner beter sig på atomär nivå är kvantmekaniken, och det är på denna teori som grundprincipsbereäkningar direkt bygger.

Elektroner har förutom sin laddning också en annan kvantmekanisk egenskap som kallas *spin*. Detta gör att elektronerna i ett material inte rör sig oberoende av varandra, utan uppvisar ett korrelerat beteende. På grund av dess stora antal blir de kvantmekaniska ekvationerna som ska lösas oerhört komplexa, vilket gör att man måste ta till diverse approximationer. Giltigheten hos sådana approximationer testas genom att jämföra resultat med experiment.

När detta teoretiska fält utvecklades under mitten av förra seklet, visade det sig att även om det korrelerade beteendet hos elektronerna gör problemet oerhört komplext, så möjliggör samma egenskaper faktiskt en beskrivning som bygger på svagt interagerande kvasipartiklar. Detta blev en grundpelare för utveckling av beräkningsmetoder som bygger på oberoende partiklar med en lokal potential som innehåller alla interaktioner. Senare forskning har dock visat att beräkningar som bygger på denna metodik har sina problem med att beskriva vissa system. Detta har i många fall kunnat förbättras genom att använda metoder som inte har sin utgångspunkt i oberoende partiklar. Dock är den senare typen mycket svårtillämplig och tidskrävande.

Beräkningar inom den här avhandlingen pekar på kopplingen mellan magnetiska och kemiska frihetsgrader, som måste behandlas tillsammans. Teoretiska scheman diskuteras där grundprincipsbereäkningar kan användas till att beskriva dessa effekter vid höga temperaturer och tryck.

Preface

The subject of this thesis is theoretical methods of describing the magnetism of transition metals at a microscopic level. Transition metals are an interesting subject for theory, since they are of high technological interest, and their magnetic properties are highly non-trivial.

The thesis is organised in three parts. In Part I, some key concepts within the fields of magnetism and materials science are introduced. In Part II, theoretical methods for performing calculations are briefly outlined. The aim is not a complete review, but only to set the stage for the discussion of the results in Part III and the articles. As an aid to the reader, an index of abbreviations is found at the end.

I want thank my supervisor, professor Igor Abrikosov, for accepting me as a PhD student, and giving me plenty of opportunities to make the most of it. My assistant supervisors: Dr Sergei Simak, has always been there to answer the most diverse questions, and share countless anecdotes about life in science, and I want to thank Dr Leonid Pourovskii for trying to teach me DMFT and letting me participate in interesting projects.

In the work on this thesis I have enjoyed several nice collaborations with very talented scientists: Dr Björn Alling, Dr Ferenc Tasnádi, Dr Arkady Mikhaylushkin and Olga Vekilova in the Theoretical Physics group; professor Ulf Helmersson and Petter Larsson in the Plasma & Coatings Physics group at Linköping University. At the Université de Rouen I am happy and grateful to have collaborated with professor Héléna Zapolsky. I also want to thank Dr Thomas Gebhardt and professor Denis Music from Aachen University for the collaboration. I am very grateful to professor Andrei Ruban at KTH for sharing his vast knowledge, kindly helping out with running the codes, and teaching us to do honest science.

I want to thank professor Antoine Georges for letting me visit his group at the École Polytechnique in Paris, and professor Silke Biermann for interesting discussions. I also want to thank Dr Rickard Armiento in the Theoretical Physics group for useful discussions. I want to thank Lejla Kronbäck, Ingegärd Andersson and Anna-Karin Stål, for doing such a good job with all administration.

It has been very interesting during this time to teach, and I want to thank my

director of studies, Dr Magnus Boman, for running this operation smoothly, and sharing his experience. I have also appreciated discussions with Dr. Lars Wilzén, professor Kenneth Järrendahl, and professor Hans Arwin.

I am grateful to have received support from the Göran Gustafsson foundation for Research in Natural Sciences and Medicine, the Swedish e-science Research Centre (SeRC), and the Swedish Foundation for Strategic Research (SSF) programs SRL grant 10-0026.

I would not have made it this far without the support of my friends, family, and colleagues. Especially, I want to thank Roger at Applied Optics, and all the members of the Computational Physics group, in particular the members of the motorised lunch-club: Patrick, Bo, Sven, Mathieu, Jonas S, Olle, Thomas, Jonas B, Elham, Joanna, Mattias, Cecilia, Paulo, Sébastien and Davide for all the nice and ever surprising lunches and “fika”-breaks (especially on Thursdays). I also want to thank the members of the Plasma & Coatings Physics Group, for a nice and helpful atmosphere. Of course, I want to thank all my friends in the Theoretical Physics group who have been an inseparable part of these years, Tobias, Christian, Olle, Peter, Hans, Weine, Nina and Magnus. I am grateful that I had the opportunity to meet Rolf and Eyvaz, who unfortunately had to leave us all much too soon.

I want to thank Johanna for standing by me when things were tough, as well as the rest of my family for supporting me.

Finally, I want to thank *you* for reading my thesis. I hope you will enjoy reading it as much as I have enjoyed writing it!

Marcus Ekholm
Linköping, May 2012

Contents

I	Introduction	1
1	Computational Materials Science	3
1.1	From the beginning	3
1.2	Crystal lattice	4
1.3	Chemical ordering	4
1.4	Phase stability	6
2	The electron liquid	9
2.1	Electron correlations	9
2.1.1	The Fermi surface	11
2.2	The quasiparticle picture	11
3	Magnetism	15
3.1	The electron magnetic moment	15
3.2	Atomic magnetism	16
3.2.1	Effects of the crystal field	16
3.3	Transition metal magnetism	16
3.3.1	Collective electron ferromagnetism	17
3.3.2	Ferromagnetic metals	17
3.3.3	Hyperfine interactions	22
3.4	Magnetic order	23
3.4.1	Ferromagnets	23
3.4.2	Antiferromagnets	23
3.4.3	Spin spirals	24
3.5	Influence of pressure	24
3.6	Finite temperature magnetism	24
3.6.1	Excitations in the ordered regime	27
3.6.2	The paramagnetic state	29

II	Methodology	31
4	An <i>ab initio</i> approach	33
4.1	The interacting many-body quantum system	33
4.2	The external potential	33
4.3	Electron interactions	34
4.3.1	The uniform electron liquid	34
4.4	Electronic Structure Calculations	37
5	Spin Density Functional Theory	41
5.1	The Kohn-Sham equations	42
5.2	Exchange and correlation approximations	43
5.2.1	Local spin density approximation	45
5.2.2	Generalised gradient approximations	45
5.3	Relativistic forms	46
5.4	Non-zero temperature	48
5.5	Performance of exchange-correlation functionals	48
5.5.1	Equilibrium properties	48
5.5.2	Finite temperature	49
5.5.3	Strong correlations	51
6	Computational Methods for the Kohn-Sham Equations	53
6.1	Hamiltonian-based methods	54
6.1.1	Augmented Plane Waves	54
6.1.2	Projector Augmented Waves	55
6.2	Green's function method	58
6.2.1	Exact Muffin-Tin Orbitals	60
6.3	Modelling random alloy potentials	64
6.3.1	Special quasirandom structures	64
6.3.2	Coherent Potential Approximation	65
6.3.3	Locally Self-Consistent Green's function method	67
7	Dynamical Mean Field Theory	69
7.1	Quantum impurity model	69
7.1.1	The local Green's function	69
7.1.2	The impurity Green's function	70
7.1.3	Self-consistency cycle	73
7.2	LDA+DMFT	73
8	Model Hamiltonians for finite temperature simulations	75
8.1	Statistical simulations of configurations	75
8.2	The Heisenberg Hamiltonian	76
8.2.1	Disordered Local Moments	78
8.3	Cluster expansion of configurational energy	78
8.3.1	Screened Generalised Perturbation Method	80

III Discussion	83
9 Results	85
9.1 Fe-Mn	86
9.1.1 Elastic properties FeMn alloys	87
9.2 Fe-Ni	92
9.2.1 Influence of the local environment on hyperfine fields	92
9.2.2 Magnetic excitations and chemical phase stability	94
9.2.3 High pressure	96
9.3 NiMnSb	102
9.3.1 Stability of (Ni,Mn)MnSb-alloys	103
10 Conclusions and outlook	109
A Units	111
B Computational details of unpublished calculations	113
B.1 Charge density and DOS	113
B.2 Comparing LSDA and PBE for Fe	113
C Spin matrices	115
Bibliography	117
Index	129
List of Publications	133
Article I	
Structural and magnetic ground-state properties of γ -FeMn alloys from <i>ab initio</i> calculations	137
Article II	
Influence of chemical composition and magnetic effects on the elastic properties of fcc Fe-Mn alloys	155
Article III	
<i>Ab initio</i> lattice stability of fcc and hcp Fe-Mn random alloys	167
Article IV	
The influence of additions of Al and Si on the lattice stability of fcc and hcp Fe-Mn random alloys	175
Article V	
Elastic properties of fcc Fe-Mn- X ($X = \text{Al, Si}$) alloys studied by theory and experiment	185

Article VI	
Supercell Calculations of Hyperfine Interactions in Transition Metal Alloys	199
Article VII	
Importance of Thermally Induced Magnetic Excitations in First- principles Simulations of Elastic Properties of Transition Metal Alloys	211
Article VIII	
Influence of the Magnetic State on the Chemical Order-Disorder Transition Temperature in Fe-Ni Permalloy	219
Article IX	
Importance of correlation effects in hcp iron revealed by a pressure-induced electronic topological transition	227
Article X	
Configurational thermodynamics of Fe-Ni alloys at Earth's core conditions	255
Article XI	
Energetics and magnetic impact of 3d-metal doping of the half-metallic ferromagnet NiMnSb	275
Article XII	
<i>Ab initio</i> calculations and synthesis of the off-stoichiometric half-Heusler phase $\text{Ni}_{1-x}\text{Mn}_{1+x}\text{Sb}$	287

Part I

Introduction

Chapter 1

Computational Materials Science

1.1 From the beginning

Physics is an experimental science. In our pursuit to explain the nature of solids, and to tailor functional materials, a microscopic theory of the solid state of matter can make macroscopic interpretations and predictions even at conditions where experiments are neither available nor feasible. A microscopic theory of solids, that is based directly on quantum mechanics, is said to be *ab initio* — meaning “from the beginning.”

Making quantitative predictions from the laws of a quantum solid-state theory results in daunting equations to be solved, which follows already from the sheer size of the problem. In addition, quantum mechanics, by its very nature, does not speak to our everyday intuition, as expressed by Werner Heisenberg during the infancy of the modern quantum theory [1]:

“Many of the abstractions that are characteristic of modern theoretical physics are to be found discussed in the philosophy of past centuries. At that time, these abstractions could be disregarded as mere mental exercises by those scientists whose only concern was with reality, but today we are compelled by the refinements of experimental art to consider them seriously.”

As will be made clear, the preferred strategy is to handle these equations by numerical simulations, based on pragmatic approximations. Since the initial calculations in the 1930’s [2], these simulations have been successively refined along with the advancement in high-performance machine computing. The accuracy of solid state theory, and the validity of underlying approximations, are assessed by comparing its predictions to experiments. In the interplay between theoretical predictions and experimental observations, *ab initio* theory advances materials science.

1.2 Crystal lattice

In *ab initio* theory, materials are modelled as a system of electrons and ions (atomic nuclei). In the solid materials studied within this thesis, the ions vibrate around equilibrium positions, which display long-range order — i.e., order over many interatomic separations. An ordered array of atoms is called a crystal lattice, which is described by translation vectors of the form:

$$\mathbf{R} = \sum_{i=1,2,3} n_i \mathbf{a}_i, n_i \in \mathbb{Z}; \quad (1.1)$$

connecting the unit cells of the crystal structure. The unit cell contains a number of atoms, N_Ω , in positions described by the basis vectors:

$$\mathbf{b} = \sum_{j=1,2,3} \eta_j \mathbf{a}_j, \eta_j \in \{\mathbb{R} : |\eta| < 1\}; \quad (1.2)$$

so that the entire lattice is specified by an expression such as:

$$\sum_{\mathbf{R}} \left(\mathbf{R} + \sum_{\varsigma=1}^{N_\Omega} \mathbf{b}_\varsigma \right). \quad (1.3)$$

The most compact unit cell that can be formed is called the Wigner-Seitz (WS) cell (polyhedron) [2, 3].¹

The sets of vectors $\{\mathbf{a}\}$ — spanning one of the 14 Bravais lattices — and $\{\mathbf{b}\}$, determine the type of the crystal lattice, such as body- or face-centred cubic (bcc, fcc), hexagonal close packed (hcp), etc. In cubic systems, $|\mathbf{a}_{1,2,3}| = a$, but in hexagonal or tetragonal systems, $|\mathbf{a}_{1,2}| = a$ and $|\mathbf{a}_3| = c \neq a$, in terms of the so-called lattice constants, a and c . In reality, a crystal is never perfect, and an atom may occupy a position not described by (1.3). However, if long-range order persists, the lattice description remains meaningful.

The same material may exist in several different *phases*, with a particular crystal structure, as external pressure and temperature is varied. Such phases are conventionally labelled as α , β , γ , etc.

1.3 Chemical ordering

In materials composed of several atomic species, many macroscopic properties are determined by how atoms arrange themselves on the underlying lattice. This is shown in Figure 1.1 where two extremal cases can be distinguished: segregation and mixing. For a binary system of A - and B -atoms, segregation means that atoms of the one kind will cluster together, so that two phases will co-exist, as in Figure 1.1(c).

Mixing can be classified depending on the amount of order between the mixed atoms. Figures 1.1(a) and 1.1(b) show an ordered and a disordered system. A

¹In multicomponent systems, this is called the *Voronoi* polyhedra [3].

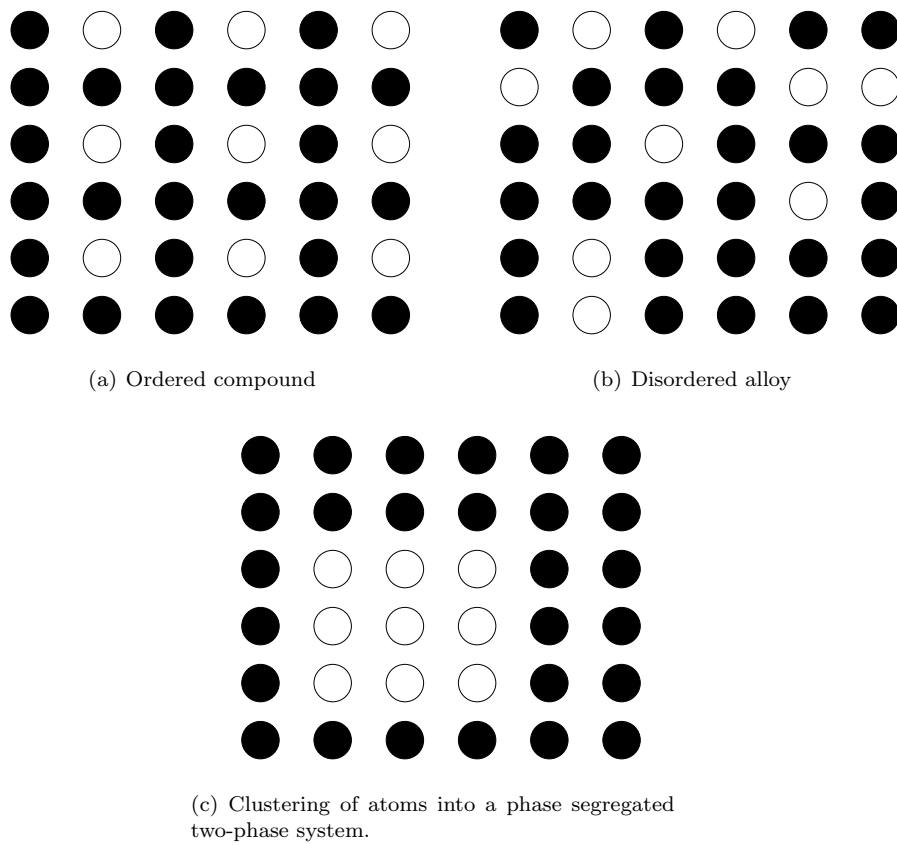


Figure 1.1. Two-dimensional illustration of various types of ordering in a binary A_3B system.

mixed system is considered chemically disordered if the long-range chemical order disappears, although some short-range order may persist. Short-range order can be defined in terms of the Warren-Cowley short-range order parameter [4]:

$$\alpha_i^{AB} = 1 - \frac{P_i(B)}{c^B}, \quad (1.4)$$

composed of the conditional probability of finding a B -atom in the i :th co-ordination shell of an A -atom, divided by the concentration of B -atoms in the alloy. $\alpha_i = 0$ thus indicates complete disorder in the i :th coordination shell.

The significance of short-range order is that it changes the *local* chemical environment of the atoms. In a completely disordered alloy, each atom is in a “unique” environment. This opens the door to local environment effects, such as local relaxations of ion positions away from the ideal positions in Equation (1.3). which may additionally change the physics of the material.

1.4 Phase stability

A single component system may have several different phases of uniform crystal structure. The relative stability of such phases will depend on temperature and pressure. In an alloy system, there is the added dimension of various possible phases of different chemical orderings.

The various regimes of a particular system may be summarised in a phase diagram, such as the one shown in Figure 1.2 for the Fe-Ni system. It is seen here that not only do phases of different orderings, but also magnetic transformations, depend on the composition and temperature. In pure Fe, the bcc-based α -phase is seen to be stable up to 912°C, where it transforms into the fcc-based γ -phase. This structural transformation takes place only 142°C above the magnetic transformation temperature from the ferromagnetic to the paramagnetic state. From 1394°C, the bcc-based δ -phase is present up to the melting point.

In pure Ni, the fcc-phase is seen to be stable all the way up to the melting point. Mixing Fe and Ni results in an fcc-based alloy system which is stable even with large amounts of Fe. At low temperature, several ordered phases of the mixture can be seen, which become disordered closely below the magnetic transformation temperature.

For theoretical materials science, the goal is to understand and predict properties such as crystal structure, chemical ordering, and magnetism; which are far from independent of each other [5]. Within the quantum theory of solids, such considerations start from the behaviour of the electrons in the system, the electronic structure. For the systems considered within this thesis, typical time scales are for:

- thermal ion vibrations $\sim 10^{-12}$ s
- magnetic reorientations $\sim 10^{-13}$ s
- electron hopping $\sim 10^{-15}$ s

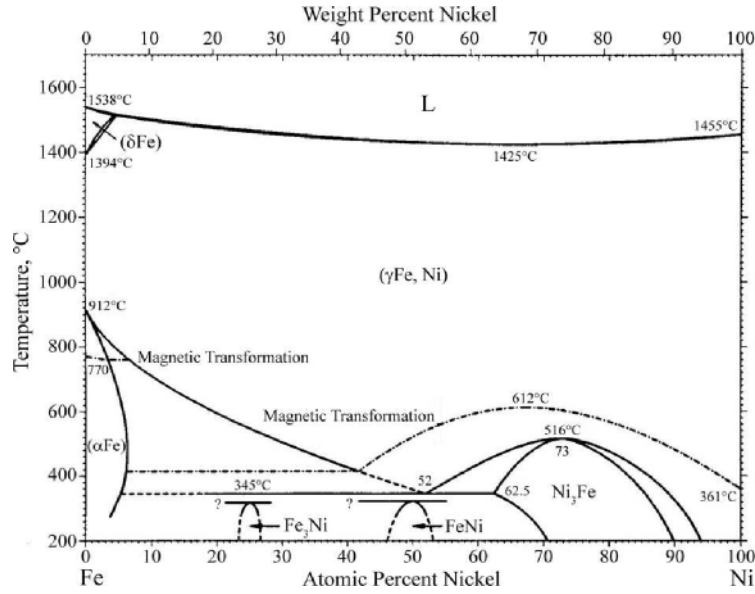


Figure 1.2. Experimental phase diagram for the Fe-Ni system. Figure from Ref. [7]. Copyrighted by the American Society for Metals.

which thus span several orders of magnitude [6]. A natural length scale may be taken as the typical interatomic distance, which is a few Ångström (Å).² Thus, for a microscopic theory to make predictions, it needs to simultaneously concern itself with very different scales. This is called multi-scale modelling.

²See Appendix A.

Chapter 2

The electron liquid

Properties such as chemical bonding and magnetism originate in the mutual interactions of the electrons. Figure 2.1 illustrates the radial electron density, $n(r)$, around a lattice site in bcc-Fe. It is seen how the valence part is extended in space, in contrast to the core electrons, which display a higher degree of localisation and atomic-like character. The electrons thus form a subsystem which may be called the *electron liquid*,¹ under the influence of the enclosed lattice of positively charged atom cores.

2.1 Electron correlations

Due to their charge, the N indistinguishable electrons in the electron liquid will repel each other *pair-wise* via the Coulomb interaction potential:²

$$\frac{1}{|\mathbf{r}_1 - \mathbf{r}_2|}, \quad (2.1)$$

which only depends on the separation between the position coordinates \mathbf{r}_1 and \mathbf{r}_2 . Thus, the motion of each electron is *correlated* [9] with the other $N - 1$ electrons, since Equation (2.1) couples the spatial coordinates.

Furthermore, according to the Pauli exclusion principle, the total quantum mechanical wave function of the system of indistinguishable electrons must be antisymmetric if two sets of coordinates are interchanged. This restriction imposes an additional type of correlation in the movement of the electrons called *exchange*, which has no classical analogue. The Coulomb repulsion energy:

$$U = \frac{1}{2} \int \int \frac{P(\mathbf{r}_1, \mathbf{r}_2)}{|\mathbf{r}_1 - \mathbf{r}_2|} d\mathbf{r}_1 d\mathbf{r}_2 \quad (2.2)$$

¹Following Ref. [8], the term “liquid” is used in this thesis for the interacting electron system, and the term “gas” is preferred in reference to the non-interacting system. In some texts, the liquid is defined to be uniform, but here may be non-uniform.

²Hartree atomic units are used for equations. See Appendix A.

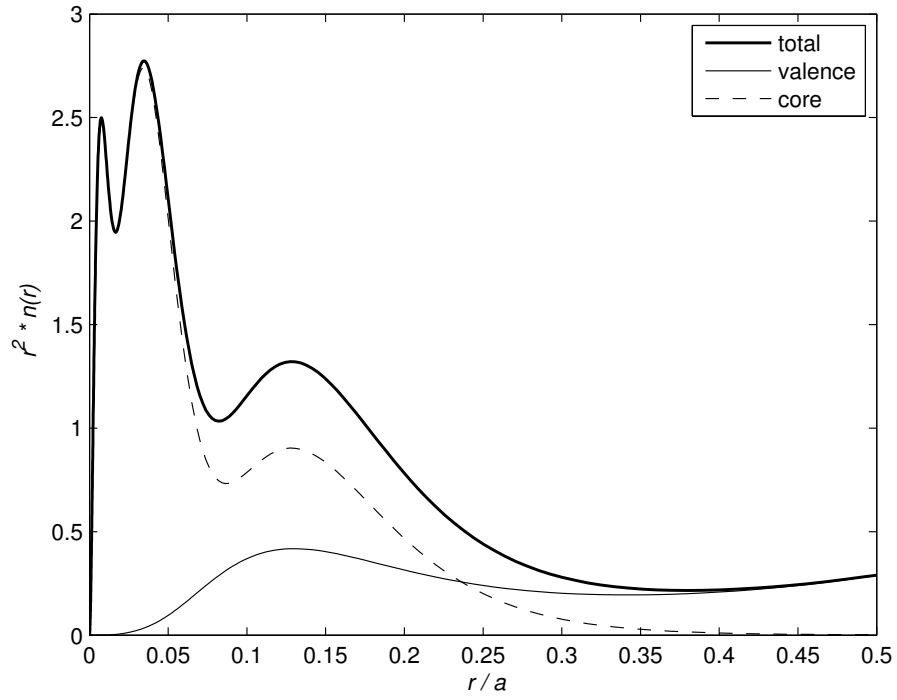


Figure 2.1. Charge density of bcc-Fe as a function of the radial coordinate r , in terms of the lattice constant a , and resolved into core (1st, 2nd shells and $3s3p$) and valence ($3d4s$) electrons. The first two peaks to the left correspond to filling of the 1st and 2nd shells. See Appendix B for computational details.

is thus a functional of the pair-density distribution, P , such that

$$P(\mathbf{r}_1, \mathbf{r}_2) d\mathbf{r}_1 d\mathbf{r}_2 \quad (2.3)$$

is the probability of simultaneously finding one electron in the region $d\mathbf{r}_1$ around \mathbf{r}_1 , and a second one in the region $d\mathbf{r}_2$ around \mathbf{r}_2 . However, the correlated motion implies that $P(\mathbf{r}_1, \mathbf{r}_2)$ is not simply a product of the electron density at these points:

$$P(\mathbf{r}_1, \mathbf{r}_2) d\mathbf{r}_1 d\mathbf{r}_2 \neq n(\mathbf{r}_1) n(\mathbf{r}_2) d\mathbf{r}_1 d\mathbf{r}_2, \quad (2.4)$$

as it would be if the particles were completely uncorrelated [10], but can be expected to have a highly complicated structure.

It has become an established picture that for an electron at \mathbf{r}_1 , exchange and correlation effects induce a region of depletion in the electronic charge density around \mathbf{r}_1 , exposing the positive ion background and thus lowering Coulomb repulsion energy [11]. The positively charged region is known as the *exchange-correlation hole*, with density denoted as \bar{n}_{xc} ,³ with opposite sign compared to the electronic density. As the electron moves through the liquid, the hole reacts back on the electron, changing its energy by an amount Σ , the *self-energy* [12].

2.1.1 The Fermi surface

Due to the Pauli exclusion principle, the energy levels of the electron liquid form bands. In metals, the population of the levels as a function of crystal momentum, $\Gamma(\mathbf{p})$, goes through a discontinuous drop at the so-called Fermi level, \mathbf{p}_F , of the height:

$$\mathcal{Z}_p = \left(1 - \lim_{\omega \rightarrow 0} \frac{\partial}{\partial \omega} \text{Re} \Sigma(p_F, \omega) \right)^{-1}, \quad (2.5)$$

where $\mathcal{Z}_p \leq 1$ [13, 14, 15]. This is demonstrated in Figure 2.2 for the case of sodium [16].

The total energy of the system, \mathcal{E} , is then a complicated functional of the crystal momentum distribution, $\mathcal{E} = E[\Gamma]$, except for the simple case of the non-interacting electron gas, $\Gamma^{(0)}$, indicated by the dashed line in Figure 2.2. The energy of the Fermi level constitutes a surface in momentum space called the Fermi surface, ε_F , that can be described as:

$$\varepsilon_F = \mu_0 - \Sigma(\mathbf{p}_F, 0), \quad (2.6)$$

in terms of the chemical potential, $\mu_0 = \partial \mathcal{E} / \partial N$ taken at 0 K [17], and the self-energy evaluated at the Fermi surface.

2.2 The quasiparticle picture

The positive charge induced by the electron in its vicinity will partially compensate its own charge, and screen its electrostatic field at large distances [8]. The

³ This notation, involving a bar sign, should not be confused with the system- and coupling-constant averaged hole, which will carry a different notation in later chapters.

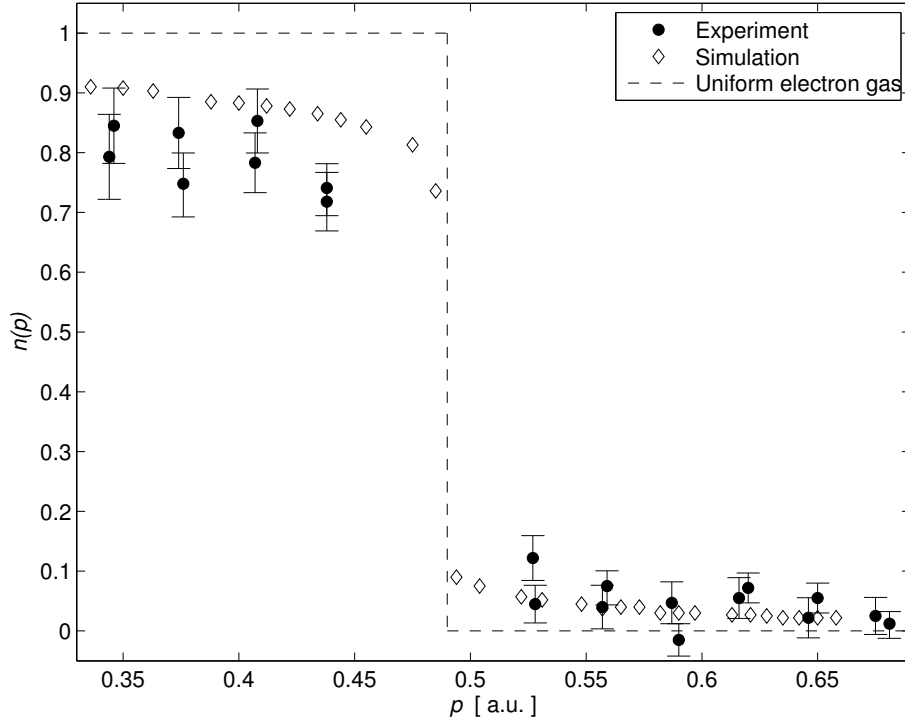


Figure 2.2. Momentum distribution per spin state, $\Gamma(p)$, in sodium (Na) as a function of momentum, replotted from the combined theoretical and experimental work by Huotari et al. [16]. The open diamonds correspond to quantum Monte Carlo simulations, and filled circles are experimental data along with reported errorbars. For comparison, the dashed line indicates the ground state distribution function of the non-interacting electron gas at 0 K. At the Fermi level, p_F , the occupation goes through a discontinuous drop of height $Z_p < 1$. Figure adapted with permission from Ref. [16]. Copyrighted by the American Physical Society.

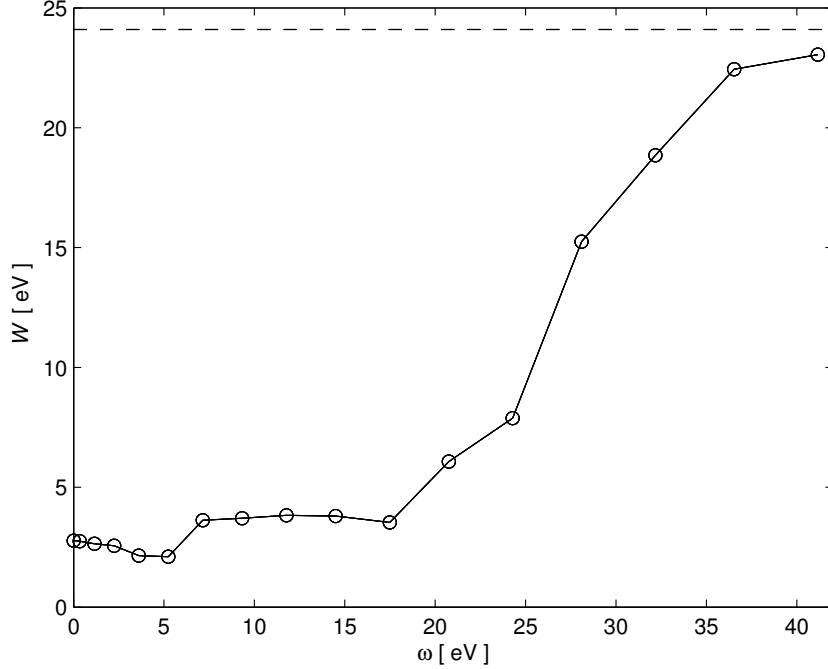


Figure 2.3. Screened Coulomb interaction (circles) as a function of frequency in paramagnetic fcc-Ni, calculated by Miyake et al. [18]. At high frequency, the interaction is comparable to that of free atoms, shown by the dashed line. In the static limit, $\omega \rightarrow 0$, the Coulomb interaction is reduced due to screening. Figure adapted with permission from Ref. [18]. Copyrighted by the American Physical Society.

magnitude of the Coulomb interaction is thus significantly reduced in the metallic state as compared to the atomic state. This is illustrated in Figure 2.3 for fcc-Ni, in the calculations by Miyake et al. [18].

As screening reduces the range of Coulomb interactions in the electron liquid, the states can be described in terms of weakly interacting *quasiparticles*, with a finite life-time:

$$\tau_{\mathbf{p}}(\omega) = -\frac{1}{2\mathcal{Z}_p(\omega)\text{Im}\Sigma(\mathbf{p}, \omega)}. \quad (2.7)$$

related to the discontinuity at the Fermi level. If τ is infinite, as in the gas of non-interacting electrons, the dispersion of possible energy values within a band, ε , with the electron wavevector, \mathbf{k} , shows a well defined relationship. Consequently, the function, $\varepsilon(\mathbf{k})$, is called band structure. Mutual interactions influence its shape, as does the periodic background potential. If τ is very small, the bands loose their structure and the spectral weight of the states becomes distributed around \mathbf{k}

The features of $\varepsilon(\mathbf{k})$, especially around the Fermi level, determine many properties. By applying pressure, the topology of the Fermi surface can be drastically

altered. This is called *electronic topological transitions* (ETTs) [19]. An ETT may lead to anomalies in the thermodynamic and kinetic characteristics of a metal [20].

In the work by Landau, Pines, Nozières, Bohm, and several others [21, 8, 17], a theory was developed for what was called normal Fermi liquids. In such systems, the behaviour of Σ close to the Fermi level is such that τ is long enough for the bands to be well defined in this region, and the quasiparticle description is then valid there. A microscopic theory of solids thus needs to be concerned with this quantum-mechanical many-body problem associated with the correlated electrons. In Part II of this thesis, the problem is more precisely defined, and the methods used for approaching it are outlined.

Chapter 3

Magnetism

It was not until the advent of quantum mechanics when a consistent microscopic theory of magnetism could be constructed. A classical theory, based solely on moving charges, cannot yield a net magnetic moment at thermal equilibrium [22]. Especially, magnetism was found to be intimately connected with an intrinsic magnetic moment of the electron.

3.1 The electron magnetic moment

The experiments initiated by Gerlach and Stern in 1922 demonstrated quantisation of atomic magnetic moments in an external magnetic field [23, 24]. These measurements could be quantitatively explained by the suggestions of Goudsmit and Uhlenbeck in 1925:¹ that the electron carries an intrinsic angular momentum, unrelated to its motion around the nucleus, which became known as the *spin*, $s = 1/2$ [31, 32].

The component of the electron spin measured along an axis ξ is restricted to the values $\sigma = \pm s$, which implies the possible projected values of magnetic moment:

$$\mathbf{M} = -\sigma g_e \mu_B \hat{\mathbf{e}}_\xi, \quad (3.1)$$

where μ_B is called the Bohr magneton and the constant g_e is the spin gyromagnetic ratio of the electron. The former has the numerical value $\frac{1}{2}$ in atomic units,² and the latter has been measured to $g_e = 2.00$ [33, 34].

¹ There are historical documents (e.g. Ref [25]) strongly indicating that Ralph Kronig actually formulated the notion of the electron spin a year before the Goudsmit and Uhlenbeck publications, but did not dare to publish it after being ridiculed by Wolfgang Pauli [26, 27]. Following the work of Edmund C. Stoner [28], Pauli incorporated the spin as a quantum number to explain the atomic shell structure [29, 30].

²See Appendix A.

3.2 Atomic magnetism

In a partially filled subshell, ℓ , of an atom (or ion), the electrons will combine the angular momenta associated with their spatial orbitals into a *total* orbital angular momentum of the atom, \mathbf{L} . The corresponding orbital magnetic moment of the atom is:

$$\mathbf{M}_L = -g_L \mu_B \mathbf{L}. \quad (3.2)$$

However, \mathbf{L} and \mathbf{S} are not independent of each other, but are coupled in what is known as the *spin-orbit interaction*. Furthermore, neither \mathbf{L} or \mathbf{S} are constants of the motion. Only the combination of the two, the total angular momentum of the atom, \mathbf{J} , will be a constant of the motion, and determine the magnetic moment of the atom:

$$\mathbf{M}_J = -g_J \mu_B \mathbf{J}, \quad (3.3)$$

where the number g_J is called the Landé-factor.

Empirically, it has been found that the ground state configuration is given by Hund's rules: maximum spin S , maximum L compatible with S ; and $J = |L - S|$ or $J = L + S$ depending on if the valence shell is less than half filled or not.

3.2.1 Effects of the crystal field

As discussed in Chapter 2, when a solid is formed the neutral atoms become ionised to some extent. The ions on the crystal lattice sites produce a non-uniform electric field called the crystal field. The crystal field counteracts the spin-orbit coupling between \mathbf{L} and \mathbf{S} , so that the states are not longer classified by \mathbf{J} .

In the absence of spin-orbit coupling, the electrons can be classified according to their orbital- and spin-angular momenta, as $\ell = s, p, d, f, \dots$, and $\sigma = \pm 1/2$. However, in contrast to the free atom, electrons with the same ℓ , but different angular probability distributions, will have different energy in the non-uniform crystal field.

3.3 Transition metal magnetism

In this thesis, the transition metals of the 3d-series are the main focus. It is common for these materials to have a cubic crystal structure. For the case of cubic symmetry, the crystal field acts to lift the 5-fold degeneracy of the d -subshell, so that these states become divided into the 3-fold degenerate t_{2g} and the 2-fold degenerate e_g states. This implies that provided that the spin-orbit coupling is small, the total orbital momentum, \mathbf{L} , is quenched, so that the magnetic moment is caused entirely by the electron spins. Each electron then contributes with 1 μ_B , as seen in Equation (3.1).

However, the total magnetic moment per atom in a transition metal is rarely an integral multiple of μ_B . This cannot be explained in terms of atomic states and Hund's rules [35]. Thus, the magnetism of transition metals is understood as being a collective phenomenon, due to correlated *itinerant* valence d -electrons

with an imbalance, ζ , between the number of spin up and down electrons, called spin polarisation:

$$\zeta = \frac{n^\uparrow - n^\downarrow}{n^\uparrow + n^\downarrow}. \quad (3.4)$$

3.3.1 Collective electron ferromagnetism

As pointed out already by J. C. Slater [36] that out of the valence electrons in metals, the $3d$ -electrons show a higher degree of localisation than the sp -electrons. For the $3d$ -electrons, which also participate in the conduction bands, the Coulomb interaction is thus stronger than for the more itinerant sp -electrons [37]. The total Coulomb repulsion energy of the system can be reduced if the electrons surrounding an electron at \mathbf{r}_1 with spin σ_1 align their spins in parallel to σ_1 . By the Pauli exclusion principle, this will keep them farther apart, and thus deepening the exchange-correlation hole and reducing the pair distribution function, P . However, this is at the expense of increased kinetic energy, and the balance between these effects will determine ζ , the fraction of aligned spins.

This mechanism was demonstrated phenomenologically by E. C. Stoner in the later half of the 1930's [38, 39]. Little was then known about the electronic band structure of transition metals [39], and Stoner assumed parabolic³ bands to calculate kinetic energy, and accounted for exchange-correlation effects by postulating an internal molecular magnetic field, created by the spin imbalance. Each electron experiences the same field strength, which is proportional to ζI . The parameter I is called the Stoner parameter, which characterises the effectiveness of the exchange-correlation mechanism.

Self-consistent solutions for ζ are then obtained as shown in Figure 3.1 in terms of the product $Ig(\varepsilon_F)$, where the function $g(\varepsilon)$ is the number of states in the interval $[\varepsilon, \varepsilon + d\varepsilon]$, called the density of states (DOS). The condition for spontaneous magnetism:

$$Ig(E_F) > 1, \quad (3.5)$$

is called the Stoner condition. The Stoner parameter can be calculated with modern electronic structure methods, and the Stoner condition can be rederived without any assumptions regarding the form of the quasiparticle bands [40]. Calculations of the exchange-correlation parameter, I , and $g(E_F)$ for the transition metal series correctly predict only Fe, Co and Ni to be ferromagnetic in the ground state [41].

3.3.2 Ferromagnetic metals

Figure 3.2 shows calculated⁴ DOS for a nonmagnetic metal, Cu, as well as three different ferromagnets: Fe, Ni, and NiMnSb. In fcc-Cu (a), the spin-up and spin-down DOS are identical. It is also seen that the d -bands are more narrow than the sp -bands. An Fe atom has the valence configuration $3d^6 4s^2$. In bcc-Fe (b) the up- and down-bands appear split in energy by an amount Δ , as compared to

³I.e, free-electron bands of the uniform electron gas (see Section 4.3.1).

⁴See Appendix B for details of the calculations.

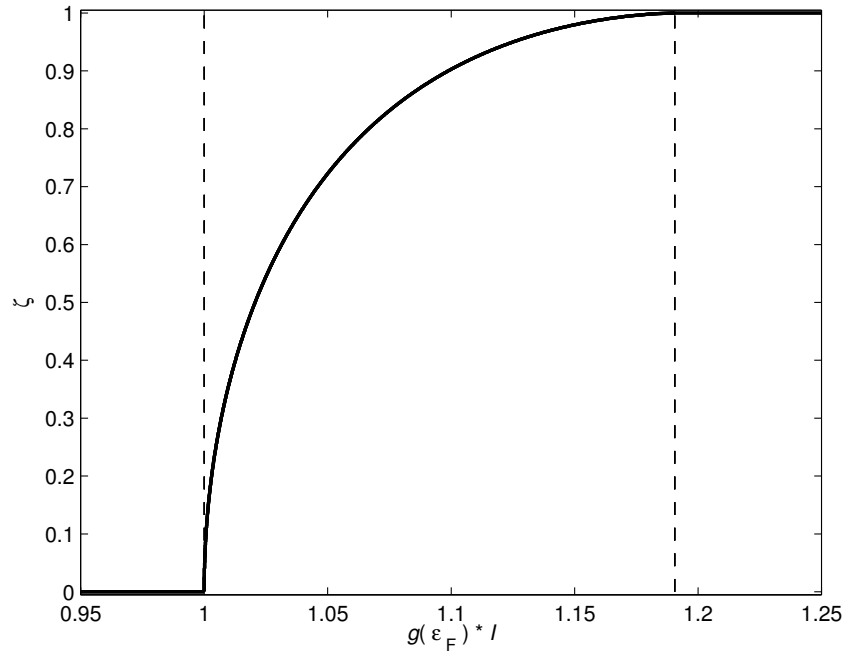


Figure 3.1. Fractional spin polarisation, ζ , of the uniform electron liquid as a function of the Stoner product, $g(E_F)I$, where g is the density of states and I is the Stoner molecular field parameter.

Table 3.1. Basis vectors, \mathbf{b} , of the Heusler crystal structure, resolved in Cartesian components and scaled in terms of the lattice constant, a . In the full Heusler structure ($L2_1$) sublattice A and C are occupied by the same atomic species, while in the half-Heusler structure ($C1_b$) sublattice C is empty, as shown in Figure 3.3.

	b_x	b_y	b_z
	a	a	a
A	0	0	0
B	0.25	0.25	0.25
C	0.50	0.50	0.50
D	0.75	0.75	0.75

a non-magnetic calculation due to the exchange-correlation mechanism described in Section 3.3.1. Instead of having 3.0 d -electrons occupying each spin direction, approximately 0.8 d -electrons are moved from the down band to the up band. Furthermore, 0.6 sp -electrons are taken in practically equal proportions from up- and down-bands and are added to the spin-up d -band. This means that in the d -band, there are 4.4 spin-up electrons and 2.2 spin-down electrons, giving the magnetic moment $2.2 \mu_B$. Ni has the configuration $3d^8 4s^2$, and in fcc-Ni (c), 4.0 d -electrons are kept in the spin down band, and 0.6 sp -electrons are added to the spin up d -band. This results in the magnetic moment $0.6 \mu_B$. fcc-Ni is usually called a saturated (or strong) ferromagnet, while bcc-Fe could be called unsaturated (or weak) [41].

Figure 3.2(d) shows the DOS for the compound NiMnSb. This material belongs to a different class: *half-metallic* ferromagnets (HMFMs) [42, 43]. One of the spin bands, in this case taken as spin down, is semi-conducting, or insulating, and the other one is metallic. These materials thus show $\zeta \rightarrow 1$ for electrons close to the Fermi level, whilst the total number of spin up (and down) electrons in the unit cell are integers. It then follows that the total magnetic moment of the unit cell is also an integer.

Half-metallicity was predicted theoretically by Robert de Groot et al. in 1983 [42] in a study on NiMnSb and PtMnSb. The crystal structure of these compounds is called half-Heusler structure, or $C1_b$ in the *Strukturbericht*-designation. This structure, which is shown in Figure 3.3 for the NiMnSb compound, is closely related to the *full* Heusler structure, $L2_1$, [44, 45] which may be described by the fcc primitive translation vectors, \mathbf{R} , and the basis vectors, \mathbf{b} , listed in Table 3.1. In the half-Heusler structure, sublattice C can be considered empty.

In NiMnSb, 18 of the valence electrons are distributed equally in the spin up and spin down bands, and the rest is found in the spin up band. As the valency is 22 in this compound, the magnetic moment is $4 \mu_B$ per unit cell. As discussed in Refs. [43, 46], half-metallicity is an idealised state obtainable only with the neglect of spin-orbit coupling and at $T = 0$ K. Nevertheless, due to the prospect of obtaining high spin polarisation of the conduction electrons, half-metals continue to be the subject of very active research for use in spin-based

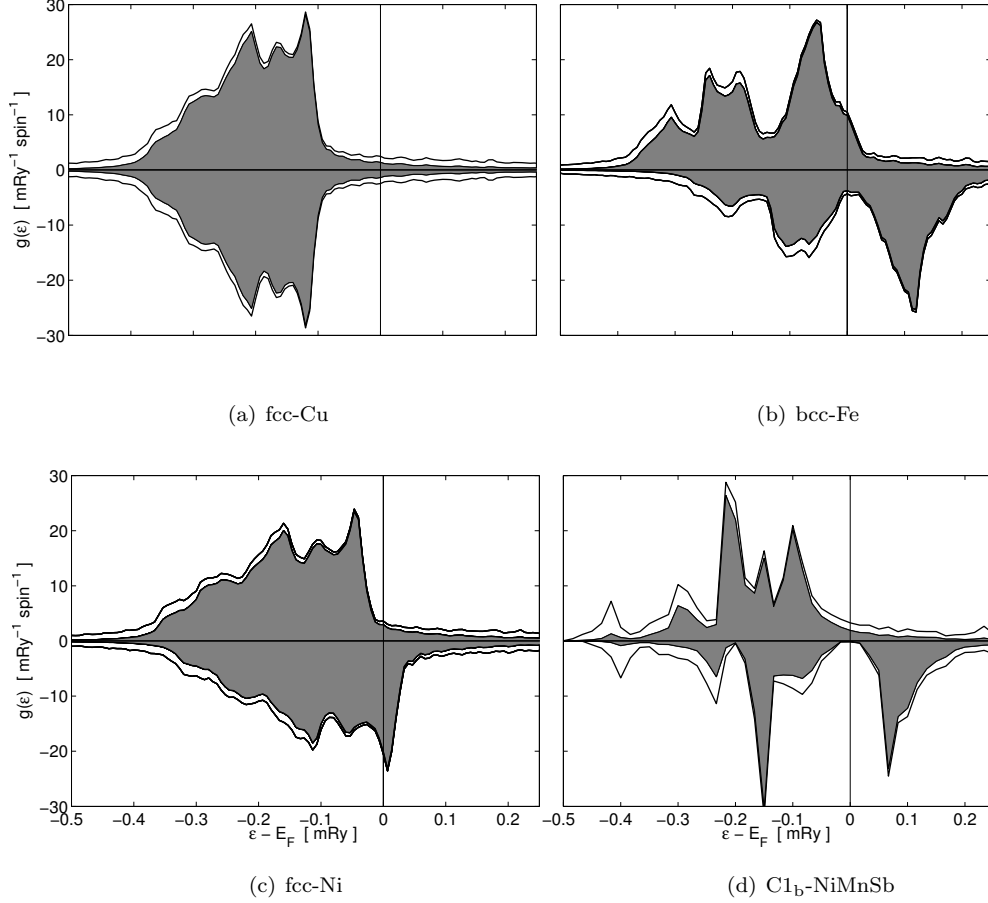


Figure 3.2. Calculated spin-resolved DOS for four prototypical systems: fcc-Cu (a), bcc-Fe (b), fcc-Ni (c), and C1_b-NiMnSb (d). Total DOS is shown by black lines, and the *d*-band DOS is shown by the shaded areas. The difference in occupied majority (positive) and minority (negative) bands is the magnetisation. fcc-Cu is nonmagnetic, as seen by the almost identical DOS for both spin-bands. In bcc-Fe and fcc-Ni, the minority and majority DOS appear shifted up and down in energy by $\Delta/2$, so that the bands are split by Δ , usually called the exchange splitting. This is in contrast to the half-metallic density of states in (d). One of the spin channels has a gap around the Fermi level, ε_F , while the other one is metallic. The occupied majority and minority parts both correspond to an integer number of electrons.

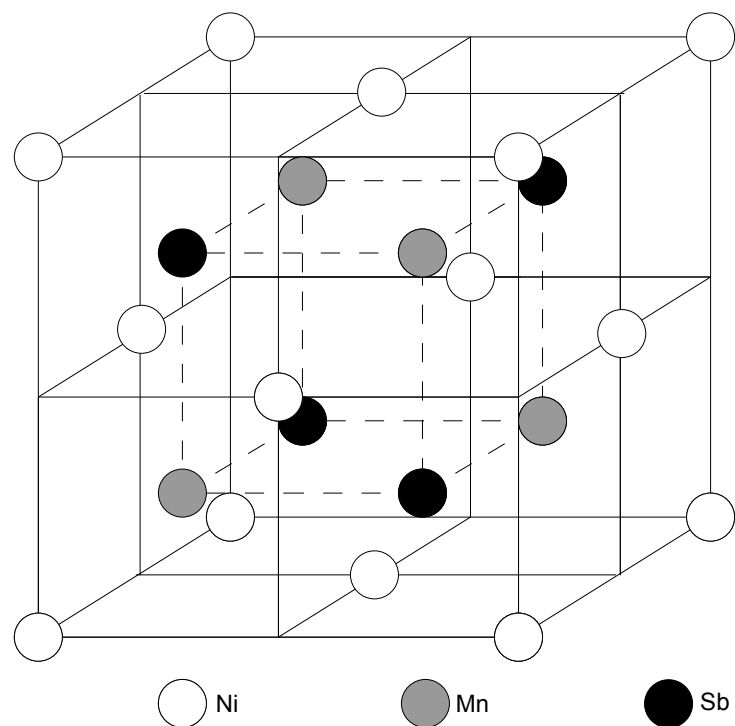


Figure 3.3. The half-Heusler (C1_b) crystal-structure. Sublattice occupancies are shown for the prototypical NiMnSb-compound.

electronics — also known as *spintronics* [47]. Although many systems have been confirmed to have this property at very low temperature (a few K), half-metallicity at room temperature so far seems to remain elusive. In NiMnSb, experiments have been interpreted as showing a crossover at $T^* = 70\text{--}100$ K into an ordinary ferromagnetic metallic state [48].

3.3.3 Hyperfine interactions

Since the s -electron wave function has a non-zero amplitude at the origin, the electrons reach the nucleus. The interaction between the electrons and the nucleus is called the Fermi contact interaction [49].

Isomer shifts

The Coulomb interaction between the contact charge and the nuclear charge, Z , gives rise to a hyperfine shift of the nuclear energy levels. By Mössbauer spectroscopy [50], one can measure the energy levels of the nucleus as it undergoes γ -radiative transitions between different excited states, isomers. Hyperfine shifts can be detected by letting the emitter and the detector be in relative motion, thus modulating the photon energy by altering the speed. The contact charge then gives rise to a shift of the entire spectrum by a small amount, δ^C , called the central shift. It can be decomposed in two terms as:

$$\delta^C = \delta^{\text{IS}} + \delta^{\text{SOD}}, \quad (3.6)$$

where the first term of the right is called isomer shift, and the second one is the relativistic second-order Doppler shift of the photon.

Hyperfine splittings

If the nucleus has a non-zero spin magnetic moment, \mathbf{M}_N , and if there is a magnetic field, \mathbf{H} , acting on the nucleus, there will be a hyperfine Zeeman-splitting of the nuclear levels, with the Hamiltonian:

$$\mathcal{H} = -\mathbf{H} \cdot \mathbf{M}_N. \quad (3.7)$$

In the absence of an external applied field, the main component of the magnetic field is due to the spin polarisation of the contact charge, corresponding to the so-called contact field, H_S [50]. Studies based on *ab initio* calculations indicate that the contact field is not only due to valence s -electrons reaching the nucleus, but the major contribution actually comes from the core electrons [51, 52]. Although the core electrons form closed shells with zero net spin, they become polarised locally through exchange-interaction with valence electrons. Measurements of these hyperfine fields can be used to determine the magnetic *order* in a material [50].

3.4 Magnetic order

The magnetisation density, which is defined in terms of the spin-resolved electron density as:

$$m(\mathbf{r}) = n^\uparrow(\mathbf{r}) - n^\downarrow(\mathbf{r}), \quad (3.8)$$

has been found to show a wave-like variation in space, even on the length scale of an atom, and not only in magnitude but also in the direction of the axis ξ [53]. In transition metal systems, it has also been found that the variation is largest in the interstitial region [54], where the magnitude of the magnetisation is also at its smallest [55, 56]. It is therefore a reasonable starting point to describe magnetisation in terms of non-integer atomic magnetic moments even in transition metals, which are related to the averaged magnetisation density:

$$\mathbf{M}_\zeta = \int_{\Xi_\zeta} m(\mathbf{r}) \hat{\mathbf{e}}_\zeta d\mathbf{r}, \quad (3.9)$$

where the region of integration, Ξ_ζ , can be chosen to be an atomic sphere, centred on the lattice site ζ . The direction of the local axis, $\hat{\mathbf{e}}_\zeta$, is then assumed only to change on the *inter*-atomic scale. This is called the atomic sphere approximation, (ASA) [40], or atomic moment approximation [54].

In terms of local magnetic moments at the lattice sites, one may distinguish several types of magnetic order, as discussed below. In turn, one may define the total magnetisation per atom as:

$$\mathcal{M} = \lim_{P \rightarrow \infty} \frac{1}{P} \sum_{i=1}^P \mathbf{M}_i, \quad (3.10)$$

in terms of the crystal lattice sites, P .

3.4.1 Ferromagnets

The term ferromagnetism (FM) may refer to a system showing spontaneous spin polarisation in the absence of a magnetic field, as in Section 3.3, or to a state of parallel magnetic moments, as shown in Figure 3.4(a). If the chemical unit cell consists of several non-equivalent atoms, the magnetic moments are not likely to be equal, and sometimes one then speaks of a *ferrimagnetic* state [57].

3.4.2 Antiferromagnets

Antiferromagnetic (AFM) order refers to an ordered configuration where the local magnetic moments, \mathbf{M}_i are arranged so that the total magnetisation in Equation (3.10) is cancelled out.⁵ There are several different kinds of AFM order. The simplest kind is called 1Q and can be described by two sublattices stacked in alternating layers, having magnetic moments oriented in opposite directions, as shown

⁵ If the magnetic moments of the site are non-equal, one sometimes speaks of anti-*ferrimagnetic* order.

in Figure 3.4(b) on the fcc lattice. AFM order can also be noncollinear, as in the 2Q and 3Q states, shown in Figures 3.4(c) and 3.4(d). These configurations can be described more generally as a superposition of spin spirals.

3.4.3 Spin spirals

Figure 3.5 illustrates a spin spiral configuration. Each magnetic moment deviates by the angle, θ , from the global quantisation axis, as shown in Figure 3.5(b). Moving through space, the direction of the moments goes through a wave-like variation, with the propagation vector \mathbf{q} . The local magnetic moment at a site at \mathbf{R} can be described by [40]:

$$\mathbf{M} = M \begin{pmatrix} \cos(\mathbf{q} \cdot \mathbf{R} + \Delta\varphi_\zeta) \sin \theta \\ \sin(\mathbf{q} \cdot \mathbf{R} + \Delta\varphi_\zeta) \sin \theta \\ \cos \theta \end{pmatrix}, \quad (3.11)$$

where \mathbf{R} denotes a translation on the lattice, and $\Delta\varphi_\zeta$ is a relative phase factor. Between the sites, the magnetic moments are thus rotated by the angle $\mathbf{q} \cdot \Delta\mathbf{R}$ around the (0,0,1)-axis.

It should be noted that if q/a is not a rational number, the spiral state will be incommensurate with the lattice, in the sense that two sites never show moments with the same direction.

3.5 Influence of pressure

As the unit cell is compressed, the electronic bands are widened, which means that $g(E_F)$ decreases. Above a certain critical pressure, P_c , the Stoner criterion, Equation (3.5) may be expected to be violated, leading to a non-magnetic state. This is expected to occur in all transition metals at sufficiently high pressure [40]. However, due the particular features of the band structure, ferromagnets may go through several complicated phases as pressure is applied [58, 59].

3.6 Finite temperature magnetism

Going from a ferromagnetic ground state at $T = 0$ K, the total magnetisation, \mathcal{M} , decreases with increasing temperature. In ferromagnets, spontaneous magnetisation disappears at the so-called Curie temperature, T_C :

$$\mathcal{M}(T) = 0, \quad T \geq T_C. \quad (3.12)$$

The analogue in antiferromagnets is called the Néel temperature, T_N , where (in principle) there is no change in net magnetisation, but the ordered arrangement is lost.

Above the Curie or Néel temperature, the magnetic state is referred to as the *paramagnetic* state. The appropriate description of the road from the ground state to this regime, and the microscopic nature of the paramagnetic state has long been

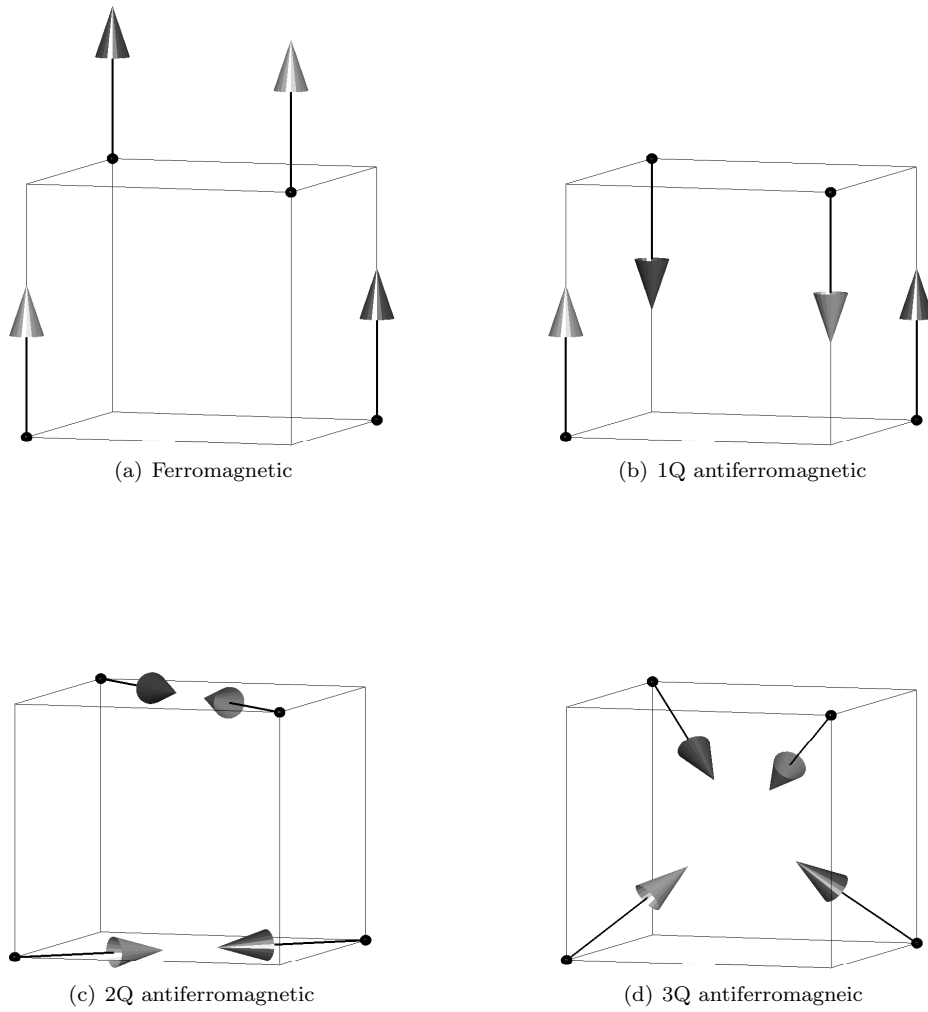


Figure 3.4. Different ordered magnetic states shown on the fcc-lattice. (a) and (b) show ferromagnetic and 1Q anti-ferromagnetic arrangements, which are collinear. In the non-collinear 2Q configuration (c), magnetic moments in alternating planes point toward a common center within the plane. In 3Q (d) all four moments in the magnetic unit cell point toward a common center.

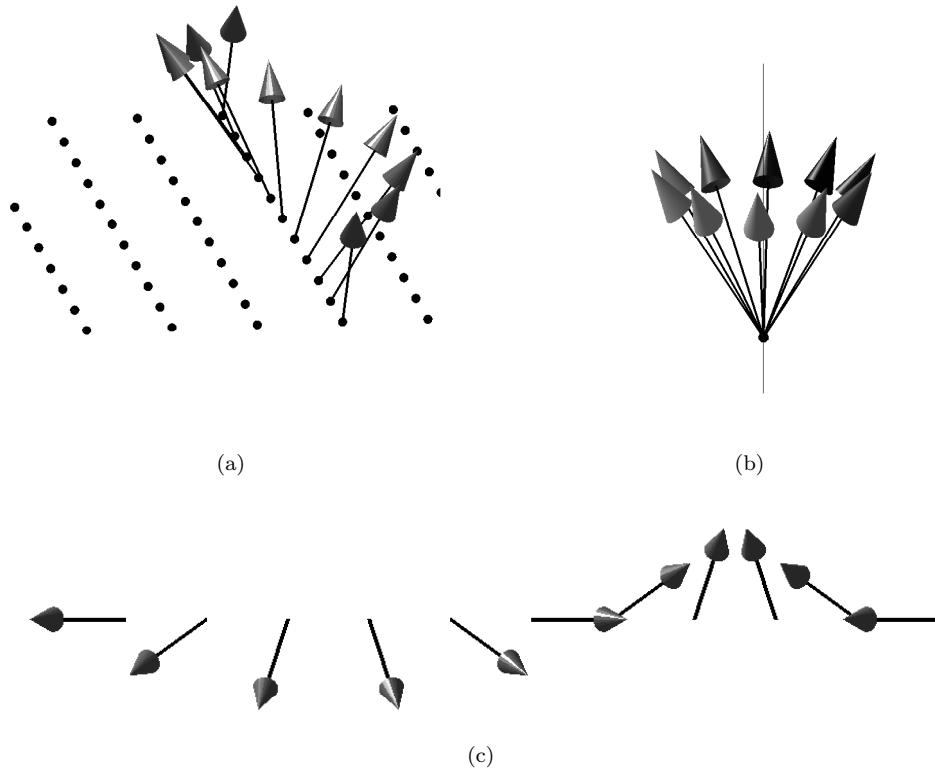


Figure 3.5. Illustration of a spin spiral. The lattice sites are connected by a translation vector with length a , and the spiral is described by a wave vector $|\mathbf{q}| = 0.2\pi/a$. Between neighbouring lattice sites, the magnetic moment is rotated by the angle $\pi/5$. (a) shows a tilted view of the spiral, and (b) shows the same magnetic moments drawn with a common origin, forming a cone around the global quantisation axis (vertical line). Each magnetic moment deviates the angle $\theta = 0.2\pi$ from the vertical axis, and has the same magnitude. In (c), the same spin spiral is shown from above.

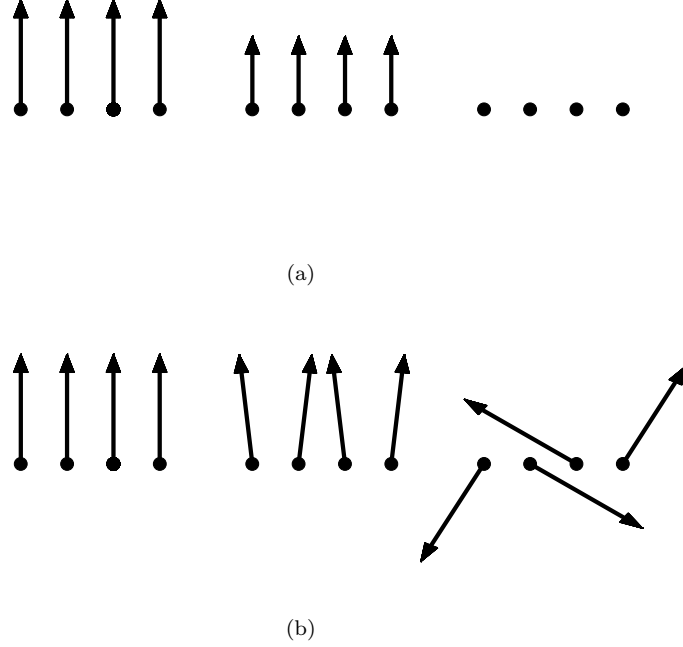


Figure 3.6. Two models of magnetic excitations in ferromagnets at finite temperature T , relative to the Curie temperature, T_C , in terms of local moments at the lattice sites. Left part shows the ferromagnetic ground state at $T = 0$, middle part shows excitations occurring at $0 < T < T_C$, and the right part shows the paramagnetic state at $T > T_C$.

debated in theory. Two mutually opposed pictures have emerged: the Stoner and the Heisenberg pictures, which are illustrated in Figure 3.6, and will be further discussed in Sections 3.6.1 and 3.6.2.

3.6.1 Excitations in the ordered regime

Although the appearance of ferromagnetism in the ground states of Fe, Co and Ni is correctly predicted by Stoner's theory at $T = 0$ K, its extension to $T > 0$ K fails badly, predicting extremely high Curie temperatures [40]. In this regime, these systems show many characteristics associated with the Heisenberg model of localised magnetic moments. The fractional change of magnetisation at low temperature, with respect to the 0 K value, \mathcal{M}_0 , has been verified experimentally to obey:

$$\mathcal{M}(T) = \mathcal{M}_0 \left(1 - \left(\frac{T}{T_C} \right)^{3/2} \right) \quad (3.13)$$

called the Bloch $T^{3/2}$ law [41]. Stoner theory fails to reproduce the Bloch law of Equation (3.13), which has been confirmed for these materials.

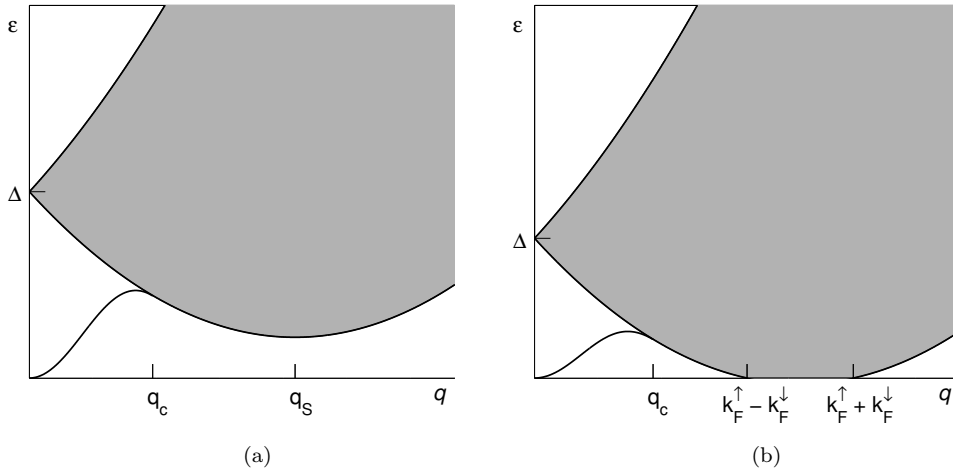


Figure 3.7. Illustration of possible magnetic excitations in a ferromagnetic system, in terms of energy (ε) and momentum (q), in the absence of a magnetic field [60, 61, 62, 63] In a strong ferromagnet (a), the low-energy excitations are spin waves with wave vectors q . A spin wave dispersion is drawn from the origin, intersecting the Stoner continuum (grey area) at the momentum q_c . The minimal energy needed for a Stoner excitation is denoted by q_s . In a weak ferromagnet (b), the lower bound of Stoner excitations coincides with the ground state energy for a certain range, given by the spin-up and spin-down Fermi momenta as: $k_F^\uparrow - k_F^\downarrow < q < k_F^\uparrow + k_F^\downarrow$. For $q = 0$, the different types of excitations are separated by the exchange splitting, Δ .

The Stoner picture of an electron in state \mathbf{k}^\uparrow being excited into the state $\mathbf{k}^\downarrow + \mathbf{q}$, thus reducing the net magnetisation, is illustrated in Figure 3.7, which shows the required energy in terms of free-electron bands. What is missing in Stoner's theory is excitations of lower energy than the exchange splitting, Δ , which are collective transverse spin-wave excitations [64, 60] of the local magnetisation [40]. The difference between these Heisenberg and Stoner excitations is illustrated in Figure 3.7. It has been shown that such excitations indeed are capable of reproducing Equation (3.13) [64]. The energy required is illustrated and compared to Stoner excitations in Figure 3.7, corresponding to the solid line intersecting the origin.

In the Heisenberg model, such excitations are described as a single spin being reversed, but this is shared among a great number of lattice sites in a spin-wave with wave vector \mathbf{q} . These spin-waves can be quantised and are then called *magnons*. The spin spiral state, shown in Figure 3.5, can be seen as a snapshot of such a magnon.

Following the work by Mook et al., it is nowadays well established that there is a frequency in the spin-wave dispersion where the spin waves suddenly decrease in intensity [65, 66]. The drop in intensity is associated with the intersection of the spin-wave energy dispersion with the Stoner continuum at q_c [67]. This is the shortest wave-length and highest energy of spin waves before the decay into Stoner single-particle excitations, which is identified with the damping of magnons.

3.6.2 The paramagnetic state

As previously mentioned, the condition of Equation (3.12) may be satisfied in two ways, as depicted in Figure 3.6. Fe and Ni both have been found to show local moments, with some short-range order up to $1.2T_C$ and $2.0T_C$, respectively [40].

By assuming rigid local moments of the Heisenberg picture, one can derive the so-called Curie-Weiss law:

$$\chi(T) = \frac{C}{T - T_C} . \quad (3.14)$$

for the magnetic susceptibility:

$$\chi = \frac{\mathcal{M}}{H} , \quad (3.15)$$

where H is an external applied field, and C is called the Curie constant. The Curie constant is usually related to an effective local moment of the atoms as:

$$C = \frac{\mu_{\text{eff}}^2}{3} = \frac{S_{\text{eff}}(S_{\text{eff}} + 1)}{3} g^2 , \quad (3.16)$$

which may deviate from the saturation moment measured at low temperature, and show additional temperature dependence [68].

Part II

Methodology

Chapter 4

An *ab initio* approach

4.1 The interacting many-body quantum system

As mentioned in Part I, the concept of *ab initio* calculations of material properties refers to the practice of simulating the quantum-mechanical equations for solid-state systems yielding measurable properties. Calculation of thermodynamic properties for a macroscopic body requires knowledge of its energy level spectrum [69]. A task of the microscopic solid-state theory is thus to predict the energy spectrum, ε .

From the viewpoint of quantum mechanics, the solid-state system; consisting of N electrons and P nuclei, is completely described by the many-body wave function:

$$\Psi = \Psi(\mathbf{r}_1, \dots, \mathbf{r}_N, \mathbf{R}_1, \dots, \mathbf{R}_P), \quad (4.1)$$

where \mathbf{r}_i and \mathbf{R}_i are the positions of the electrons and nuclei respectively, and also contains spin degrees of freedom. The discrete energy levels of the system are then the eigenvalues of the Hamiltonian operator H ,

$$\mathcal{H}\Psi = \mathcal{E}\Psi, \quad (4.2)$$

consisting of a one-body kinetic energy operator, T , and two-body potential energy operators, V . The eigenvalues are given as a functional of the wave function:

$$\mathcal{E} = E[\Psi] = \langle \Psi | \mathcal{H} | \Psi \rangle. \quad (4.3)$$

Basic assumptions of the properties of \mathcal{H} will be discussed in the remainder of this chapter.

4.2 The external potential

The ions of the crystal lattice produce a time-dependent background potential, interacting with the electronic subsystem. However, the time scale of the ionic

movement is much longer than for the electrons, due to the large difference in mass, as discussed in Section 1.4. According to the work by Born and Oppenheimer [70], it may therefore be a reasonable approximation to consider the external potential acting on the electron-liquid as static, and with the periodicity of the equilibrium lattice positions:

$$V^{\text{ext}}(\mathbf{r} + \mathbf{R}) = V^{\text{ext}}(\mathbf{r}). \quad (4.4)$$

This approximation of an adiabatic electron system has been adopted throughout this thesis.

4.3 Electron interactions

As discussed in connection with Equation (2.2), the correlated motion of the electrons implies that the electronic interaction energy cannot be written as a simple product of densities. Hence, a calculation the Coulomb energy including a full description of how the electrons behave under their mutually repulsive Coulomb interaction and the Pauli principle is a highly non-trivial problem, in fact, the most difficult part of the *ab initio* treatment. The reason for this is easily articulated in the language of second-quantisation, where the interaction energy operator has the form:

$$V = \frac{1}{2} \sum_{\sigma_1 \sigma_2} \int d\mathbf{r}_1 \int d\mathbf{r}_2 \Psi_{\sigma_1}^\dagger(\mathbf{r}_1) \Psi_{\sigma_2}^\dagger(\mathbf{r}_2) \frac{1}{|\mathbf{r}_1 - \mathbf{r}_2|} \Psi_{\sigma_2}(\mathbf{r}_2) \Psi_{\sigma_1}(\mathbf{r}_1), \quad (4.5)$$

and reveals that the potential acting on each electron, with position vector \mathbf{r}_1 , depends on the position of every other electron in the system, at positions \mathbf{r}_2 .

The Coulomb force is long-ranged, which means that many electrons may affect a single one. However, as discussed in Chapter 2, the major physical effect of the collective electron behaviour is to screen the Coulomb interaction, reducing its range. It is a clever idea to decompose P in two parts:

$$P(\mathbf{r}_1, \mathbf{r}_2) = n(\mathbf{r}_1) [n(\mathbf{r}_2) + \bar{n}_{\text{xc}}(\mathbf{r}_1, \mathbf{r}_1 + \mathbf{u})], \quad (4.6)$$

where $\mathbf{u} = \mathbf{r}_2 - \mathbf{r}_1$ and \bar{n}_{xc} is the exchange-correlation hole introduced in Section 2.1. Inserting Equation (4.6) into Equation (2.2) yields two terms:

$$U = U_{\text{H}} + U_{\text{xc}}, \quad (4.7)$$

called the Hartree energy and the Coulomb exchange-correlation energy. This can be perceived as a separation of the Coulomb energy into a long-ranged and a short-ranged part. The properties of the exchange-correlation hole has been studied extensively in theoretical physics. The simplest system to study this with regards to solid-state systems is the uniform electron liquid.

4.3.1 The uniform electron liquid

By approximating the external potential as a uniform, smeared out positive background charge that cancels the total charge of the electrons, the electron interactions can be studied without the influence of the ions. By symmetry, this electron

liquid will be uniform, and characterised by its density, n , and the degree of spin polarisation, ζ . Although not existing in nature, it is a canonical system for studies of electron-electron interactions. As will be seen in Chapter 5, modern *ab initio* calculations of realistic systems rely on results obtained in this regime.

The uniform density is conveniently expressed in terms of the radius of the Seitz sphere:

$$r_s = \left(\frac{3}{4\pi n} \right)^{1/3}, \quad (4.8)$$

which contains exactly one electron on average [2]. Taking the uniform, positive background into account, the total energy per electron takes the form:

$$\begin{aligned} \epsilon(r_s, \zeta) &= t(r_s, \zeta) + u_{xc}(r_s, \zeta) \\ &= t_s(r_s, \zeta) + \epsilon_x(r_s, \zeta) + \epsilon_c(r_s, \zeta), \end{aligned} \quad (4.9)$$

where t_s is the average kinetic energy of the non-interacting electrons of the electron gas, ϵ_x is the interaction energy due to exchange, and ϵ_c is the correlation energy [9].

Kinetic energy

For a system of non-interacting electrons, the average kinetic energy per particle has the form:

$$t_s = \frac{C_t}{r_s^2} \varphi_5(\zeta), \quad (4.10)$$

where

$$C_t = \frac{3}{10} \left(\frac{9\pi}{4} \right)^{2/3} \text{Ha}, \quad (4.11)$$

and φ_5 belongs to the family of spin scaling functions [71]:

$$\varphi_k(\zeta) = \frac{(1 + \zeta)^{k/3} + (1 - \zeta)^{k/3}}{2}. \quad (4.12)$$

Figure 4.1 illustrates the spin-dependence of t_s .

Exchange energy

The part of potential energy of the electron liquid due to Pauli repulsion is called exchange energy. It can be evaluated analytically as a function of density and spin polarisation [37, 71], with the result :

$$\epsilon_x^{\text{hom}}(r_s, \zeta) = -\frac{C_x}{r_s} \varphi_4(\zeta), \quad (4.13)$$

where

$$C_x = \sqrt[3]{\frac{125}{18\pi^4}} C_t \approx \frac{C_t}{2.41}. \quad (4.14)$$

The spin-dependence is shown in Figure 4.1 along with that of t_s .

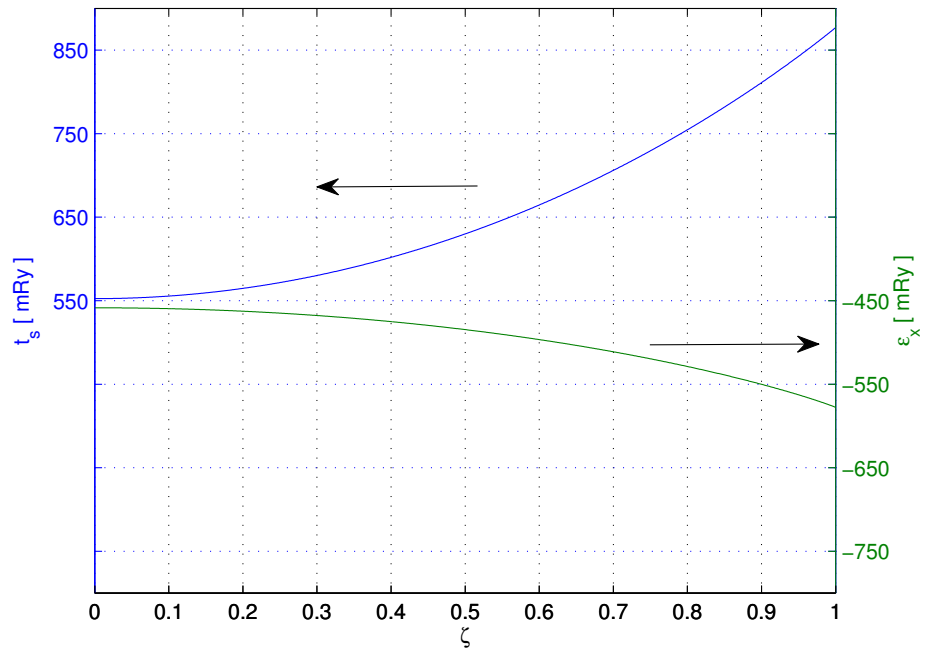


Figure 4.1. Spin scaling of the kinetic (t_s) and exchange- (ϵ_x) energy per particle in the uniform electron gas, drawn for the case $r_s = 2$ a.u.

Correlation energy

The correlation energy term can be thought of as a correction term which connects the non-interacting electron gas and the interacting electron liquid:

$$\begin{aligned}\epsilon_c &= t_c + u_c \\ &= t - t_s + u - \epsilon_x.\end{aligned}\tag{4.15}$$

In contrast to the kinetic- and exchange-energy parts, it is not possible to write an exact analytical expression for the correlation energy density, ϵ_c .

However, numerical simulations have been carried out by means of quantum Monte Carlo simulations, which was pioneered by Ceperly and Alder (CA) [72] for $r_s \in \{1, 2, 5, 10, 20, 50, 100\}$ and $\zeta \in \{0, 1\}$, and more recently in Refs. [73, 74]. Together with results obtained by, eg, the random phase approximation (RPA) to the self-energy in the $r_s \rightarrow \infty$ limit, analytical parametrisations have been constructed. Figure 4.2 shows such a parametrisation, the Perdew-Wang (PW) [75] form, for the unpolarised case.

Several other parametrisations have been suggested, among which the older Volko-Wilk-Nusair (VWN) [76] and Perdew-Zunger (PZ) [77], should be mentioned. Figure 4.3 compares the spin-scaling of the VWN,¹ PZ,² and PW-forms, which reveals the minute differences.

4.4 Electronic Structure Calculations

Based on the assumption discussed in the preceding sections, the Hamiltonian can then be written, within the additive constant of nuclear interaction energy, as:

$$\mathcal{H} = T + V + V^{\text{ext}}.\tag{4.16}$$

Proceeding from the full many-body wave function still quickly becomes impractical in the context of solid-state systems. To illustrate this point, one can imagine to use a wave function for a system of 50 particles, each particle having 3 degrees of freedom corresponding to the spatial dimension. If 100 grid points is used to resolve each dimension, $100^{3 \cdot 50}$ data points are needed to store information about the system [80]. Thus, the computational cost quickly becomes unmanageable.

One therefore needs to resort to theoretical methods which offer a reasonable balance between computational cost and accuracy. In Chapters 5 and 7, two methods used within this thesis are described, which differ in the level of approximation.

¹The VWN-curve corresponds form “V” in Ref. [76].

² It should be noted that in the PZ-parametrisation [77], the spin-scaling function suggested by von Barth and Hedin [78] is used, namely $\varphi_4(\zeta)$.

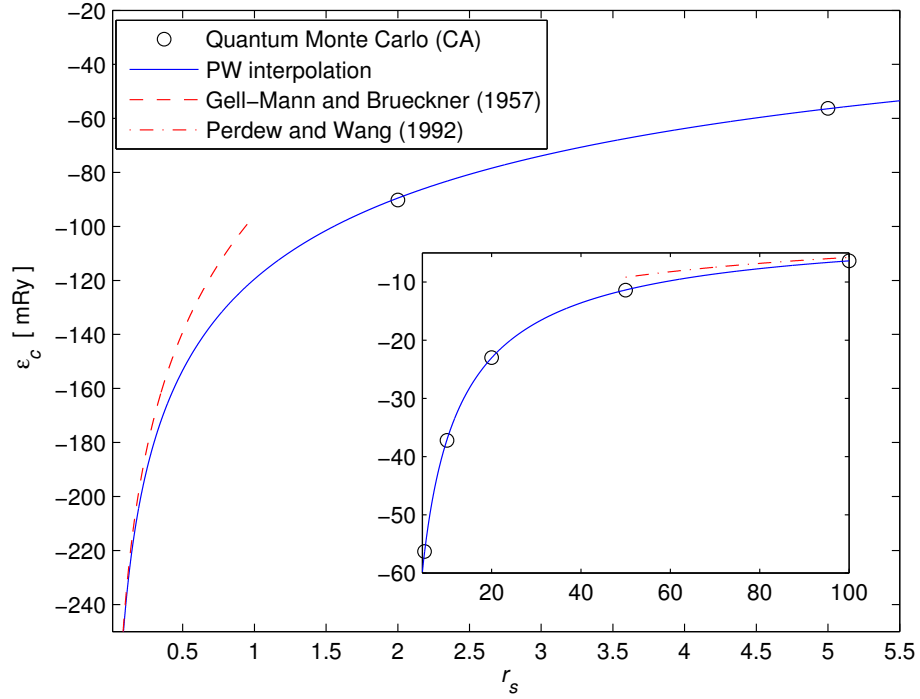


Figure 4.2. Density scaling of the uniform electron liquid correlation energy in the PW parametrisation. Results from QMC simulations [72] are shown as circles. The dashed curve corresponds to many-body calculations [79] which become exact as $r_s \rightarrow 0$. The dash-dotted curve shows the $r_s \rightarrow \infty$ limit as derived in Refs. [76, 75].

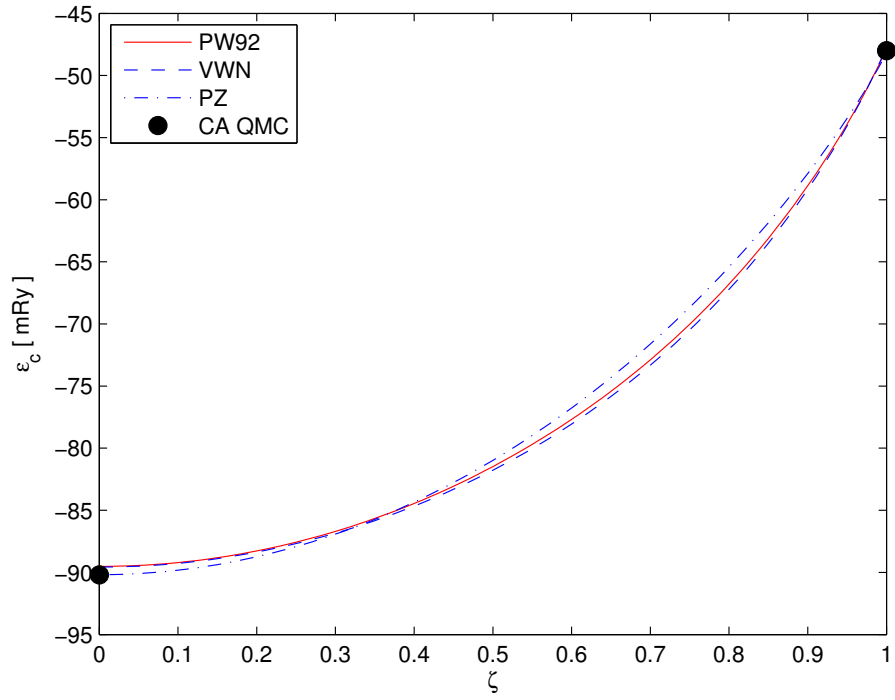


Figure 4.3. Spin scaling of the uniform electron gas exchange- and correlation energy. Circles indicate correlation energies extracted [76] from the quantum Monte-Carlo simulations by Ceperley-Alder [72] for the ground state energy. The interpolations by Perdew and Wang (PW) [75], Vosko-Wilkes-Nusair (VWN) [76], and Perdew-Zunger (PZ) [77].

Chapter 5

Spin Density Functional Theory

During the 1960's, Kohn, Hohenberg, and Sham presented a basis for treating the many-body problem using the electronic density instead of the many-body wave-function. This became known as density functional theory (DFT) [81, 82]. Following its subsequent generalisations [83, 78, 84], it is today synonymous with the band theory of electronic structure, and in 1998, Walter Kohn shared the Nobel prize in Chemistry for his work on DFT.

The essence of DFT is that the minimum energy in Equation (4.3), \mathcal{E}_0 , can be found by minimising a density functional:

$$E[n] = \int V_{\text{ext}}(\mathbf{r})n(\mathbf{r})d\mathbf{r} + F[n], \quad (5.1)$$

for fixed V_{ext} , and the functional F is a truly universal density functional, independent of the external potential and the same for every electronic structure problem [81]. Thus the density n can be used as the fundamental variable instead of the full many-body wave function, Ψ . Since the density depends on just three coordinates instead of $4N$ coordinates,¹ like the wave function does, this reformulation is a major simplification of the many-body problem.

In spin density functional theory (SDFT) [78] the density has explicit spin dependence and may be represented by a matrix, $\mathbf{n}(\mathbf{r})$, with the elements:

$$n_{\alpha\beta}(\mathbf{r}) = \langle \Psi | \Psi_{\beta}^{\dagger}(\mathbf{r}) \Psi_{\alpha}(\mathbf{r}) | \Psi \rangle, \quad (5.2)$$

where α and β are spin indices. The charge density is then given by:

$$n(\mathbf{r}) = \text{Tr } \mathbf{n}(\mathbf{r}). \quad (5.3)$$

The density matrix is in the general case non-diagonal. Off-diagonal elements are due to components of the magnetisation perpendicular to the global quantisation

¹ $3N$ space coordinates and 1 spin degree of freedom.

axis [85].² However, it may be diagonalised locally by a unitary transformation:

$$\sum_{\alpha\beta} U_{i\alpha}(\mathbf{r}) n_{\alpha\beta}(\mathbf{r}) U_{\beta j}^\dagger(\mathbf{r}) = \delta_{ij} n_i(\mathbf{r}), \quad (5.4)$$

involving the spin-1/2 rotation matrix² as:

$$\mathbf{U}(\mathbf{r}) = \mathbf{U}(\Delta\theta(\mathbf{r}), \Delta\varphi(\mathbf{r})), \quad (5.5)$$

and the functions $\Delta\theta$ and $\Delta\varphi$, are related to the elements of the non-diagonal matrix \mathbf{n} as:

$$\Delta\varphi(\mathbf{r}) = -\arctan \frac{\text{Im } n_{12}(\mathbf{r})}{\text{Re } n_{12}(\mathbf{r})}, \quad (5.6)$$

and

$$\Delta\theta(\mathbf{r}) = \arctan \frac{2\sqrt{(\text{Re } n_{12}(\mathbf{r}))^2 + (\text{Im } n_{12}(\mathbf{r}))^2}}{n_{11}(\mathbf{r}) - n_{22}(\mathbf{r})}, \quad (5.7)$$

which means that the transformation in Equation (5.4) can be thought of as rotations of the local magnetisation by angles the θ and ϕ described in Figure 3.5. Within the local frame at \mathbf{r} , the magnetisation density is obtained as:

$$m(\mathbf{r}) = \text{Tr } \{\sigma_z \mathbf{n}\} = n^\uparrow(\mathbf{r}) - n^\downarrow(\mathbf{r}) \quad (5.8)$$

in terms of the Pauli spin matrix² σ_z .

5.1 The Kohn-Sham equations

In the construction of E by Kohn and Sham [82], F is written as:

$$F = T_s + U + E_{xc} \quad (5.9)$$

where T_s and U are the kinetic and electrostatic energy of the non-interacting Kohn-Sham quasi-particles, defined to have the same ground state density as the real physical system. The density of the Kohn-Sham quasi-particles are given in terms of the lowest occupied independent-particle states:

$$n_{\beta\alpha}(\mathbf{r}) = \sum_{i=1}^N \psi_{i\beta}(\mathbf{r}) \psi_{i\alpha}^*(\mathbf{r}), \quad (5.10)$$

where

$$\psi_i = \begin{pmatrix} \phi_\uparrow(\mathbf{r}) \\ \phi_\downarrow(\mathbf{r}) \end{pmatrix} \quad (5.11)$$

The orbitals satisfy the set of equations:

$$\mathcal{H}^{\text{KS}} \psi_i = \varepsilon_i \psi_i, \quad (5.12)$$

²See Appendix C.

where the Kohn-Sham Hamiltonian has the form:

$$\mathcal{H}^{\text{KS}} = -\frac{1}{2}\nabla^2\mathbf{1} + \mathbf{v}^{\text{eff}}(\mathbf{r}), \quad (5.13)$$

with the effective one-electron potential:

$$V_{\alpha\beta}^{\text{eff}}(\mathbf{r}) = v^{\text{ext}}(\mathbf{r}) + \delta_{\alpha\beta} \int \frac{n(\mathbf{r}')}{|\mathbf{r} - \mathbf{r}'|} d\mathbf{r}' + v_{\alpha\beta}^{\text{xc}}(\mathbf{r}). \quad (5.14)$$

The second term on the right-hand side is the Coulomb energy of the electron gas, called Hartree energy. The third term is the exchange-correlation potential, which corrects the long-ranged Coulomb interaction with correlation effects.

$$v_{\alpha\beta}^{\text{xc}}(\mathbf{r}) = \frac{\delta E_{\text{xc}}[\mathbf{n}]}{\delta n_{\alpha\beta}(\mathbf{r})}. \quad (5.15)$$

The kinetic energy of the independent Kohn-Sham quasi-particles is given exactly as:

$$T_s = \frac{1}{2} \sum_{\alpha} \sum_{i=1}^N \int \nabla \psi_{i\alpha}^*(\mathbf{r}) \nabla \psi_{i\alpha}(\mathbf{r}) d\mathbf{r}. \quad (5.16)$$

Equations (5.10), (5.12) and (5.14) are called the Kohn-Sham equations, and may be solved self-consistently for the ground state effective potential and the corresponding density. Figure 5.1 shows the self-consistency scheme. The total energy functional can be written as:

$$E[\mathbf{n}] = \sum_i \varepsilon_i - \frac{1}{2} \iint \frac{n(\mathbf{r})n(\mathbf{r}')}{|\mathbf{r} - \mathbf{r}'|} d\mathbf{r}d\mathbf{r}' - \sum_{\alpha,\beta} \int v_{\alpha\beta}^{\text{xc}}(\mathbf{r}) n_{\beta\alpha}(\mathbf{r}) d\mathbf{r} + E_{\text{xc}}[\mathbf{n}]. \quad (5.17)$$

5.2 Exchange and correlation approximations

The exchange-correlation functional is thus aimed at correcting the non-interacting system energy. Formally, the exchange-correlation functional can be written in terms of the exchange-correlation hole, $\bar{n}_{\text{xc}}(\mathbf{r}, \mathbf{r} + \mathbf{u})$, which was introduced in Section 2.1, averaged over the coupling constant λ :

$$\langle \bar{n}_{\text{xc}} \rangle_{\lambda} = \int_0^1 d\lambda \bar{n}_{\text{xc}}^{\lambda}, \quad (5.18)$$

where λ linearly scales the electron charge, and connects the electron gas ($\lambda = 0$) and the electron liquid ($\lambda = 1$). The exchange-correlation energy can then be interpreted as the electrostatic energy:

$$E_{\text{xc}}[n] = \frac{1}{2} \iint d\mathbf{u} d\mathbf{r} \frac{n(\mathbf{r}) \langle \bar{n}_{\text{xc}}(\mathbf{r}, \mathbf{r} + \mathbf{u}) \rangle_{\lambda}}{|\mathbf{u}|}. \quad (5.19)$$

However, no exact analytical expression for the hole is known, and consequently not for the functional, E_{xc} , either. One must therefore find good approximate functionals. They may be divided into two classes, as described below.

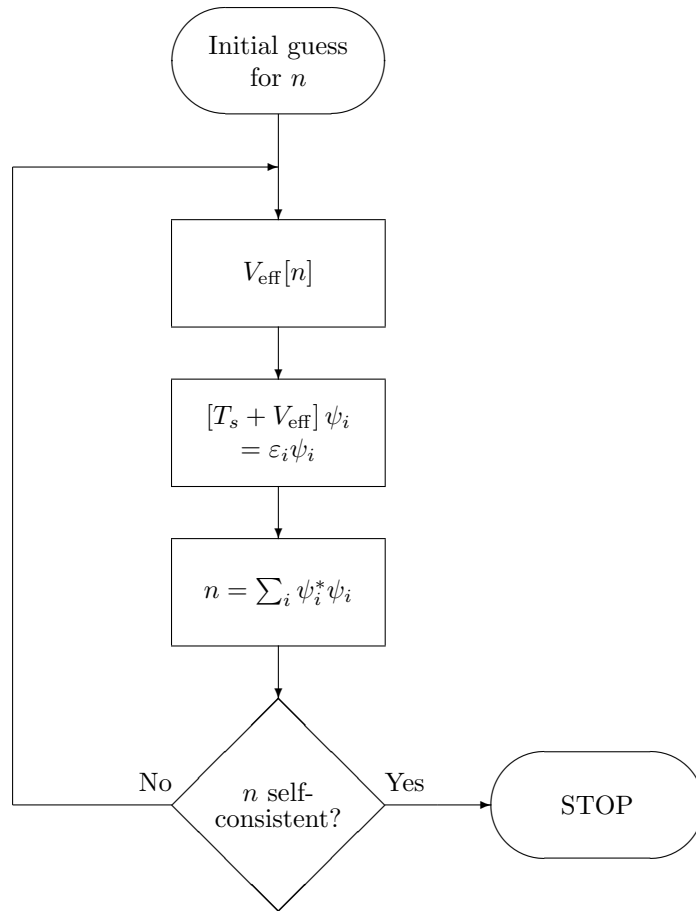


Figure 5.1. Flow chart showing the self-consistency procedure to solve the Kohn-Sham equations.

5.2.1 Local spin density approximation

In Equation (5.17), the long-ranged Coulomb interactions have been gathered in the Hartree term. As discussed earlier, the corrections to this can be expected to be quite local. Walter Kohn called this the principle of near-sightedness: the exchange-correlation hole at \mathbf{r} is largely determined by the effective potential (and chemical potential) near \mathbf{r} [86, 80]. Hence, a simple and reliable form of the exchange-correlation functional can be obtained by making a *local* approximation to the exchange-correlation energy per electron, ϵ_{xc} , at each point \mathbf{r} in space.

The exchange- and correlation-energy for electrons at \mathbf{r} then only depends on the spin-resolved density at the point \mathbf{r} , which is identical to that of an electron system with a uniform density, characterised by $r_s(\mathbf{r})$ and $\zeta(\mathbf{r})$, ie, the uniform electron liquid, which was discussed in Section 4.3.1. The corresponding functional is called the local spin density approximation² (LSDA) [82, 78], and can be written as:

$$E_{xc}^{\text{LSDA}}[n^\uparrow, n^\downarrow] = \int n(\mathbf{r}) \epsilon_{xc}^{\text{hom}}(r_s(\mathbf{r}), \zeta(\mathbf{r})) d\mathbf{r}. \quad (5.20)$$

As mentioned in Section 4.3.1, the correlation energy must be interpolated by an analytical formula, which means that although it is unambiguously defined, there are different parametrisations of the LSDA. Since it is fitted to a “real” system, the exchange-correlation hole satisfies several important analytical constraints by construction [87].

5.2.2 Generalised gradient approximations

For non-uniform systems, the LSDA may be perceived as the zeroth-order term in an expansion of the exchange-correlation energy in rising powers of the local density gradient, ∇n . By studying the response of the electron liquid to a perturbing potential, the coefficients of a second-order gradient expansion approximation (GEA) [88, 89, 90]. Subsequently, the truncated expansion has been generalised, and such functionals are thus called generalised gradient approximations (GGAs). They may be written on the form:

$$E_{xc}^{\text{GGA}}[n^\uparrow, n^\downarrow] = \int d\mathbf{r} n(\mathbf{r}) f(n^\uparrow, n^\downarrow, \nabla n^\uparrow, \nabla n^\downarrow), \quad (5.21)$$

where the function f takes the local density and the local gradient, as its arguments — thereby making the description of the interaction *semi-local*. The potential in Equation (5.15) takes the form [91]:

$$v_{xc, \text{GGA}}^{\uparrow, \downarrow} = \frac{\partial f}{\partial n^{\uparrow, \downarrow}} - \nabla \cdot \left(\frac{\partial f}{\partial \nabla n^{\uparrow, \downarrow}} \right). \quad (5.22)$$

There exist several non-empirical forms of f . Within this thesis, the GGAs proposed by Perdew and Wang (PW91), [75, 91] and Perdew, Burke and Enzerhof (PBE) [92] have been used. In addition, the recent PBEsol [93] functional has been

² The version of LSDA that only takes the total density, n , as input is called LDA [82].

tested, which was designed to fulfill conditions especially important for ground state properties of solids, such as the lattice parameter [94]. The function f can be written on the form:

$$f = F(s, \zeta) \epsilon_x^{\text{hom}}(r_s) + \epsilon_c^{\text{hom}}(r_s, \zeta) + H(t, r_s, \zeta), \quad (5.23)$$

where s is a dimensionless scaled gradient parameter and $t = t(s)$. It should be emphasised that in the limit of vanishing gradients:

$$F(s, \zeta) = \varphi_4(\zeta), \quad H(t(s), r_s, \zeta) = 0; \quad s \rightarrow 0, \quad (5.24)$$

so that the LSDA functional is recovered.

In Figure 5.2, the functions F and H are plotted for the unpolarised electron gas³ with $r_s = 2$ a.u., as a function of the gradient. The PBE- and PW91-parametrisations are seen to be very close. PBEsol is seen to deviate from the other two, especially in the form for F . Interestingly, for transition metals, this functional is known to yield almost identical results to the earlier GGA-functional suggested by Armiento and Mattsson (AM05) [95, 96, 97, 98], which has a very different form for F .⁴

5.3 Relativistic forms

Relativistic corrections can be expected to influence both the electron kinematics and the interactions [99]. Formally, relativistic density functional theory has been derived, which is based on that the ground-state energy is a unique functional of the four-current density, $J^\mu = (\mathbf{J}, n)$ [100, 101, 102]. Equation (5.12) is replaced by the Kohn-Sham Dirac equation:

$$\mathcal{H}^{\text{KSD}} \psi_i = \epsilon_i \psi_i, \quad (5.25)$$

where ψ are four-vectors for a non-interacting system, and \mathcal{H}^{KSD} is the Kohn-Sham Dirac single-particle Hamiltonian. Electronic-structure calculations typically employ a scalar effective potential, and use the non-relativistic form for E_{xc} .

It is common to employ the so-called scalar-relativistic approximation [103] to Equation (5.25) when treating valence electrons. The Hamiltonian is then divided in two parts:

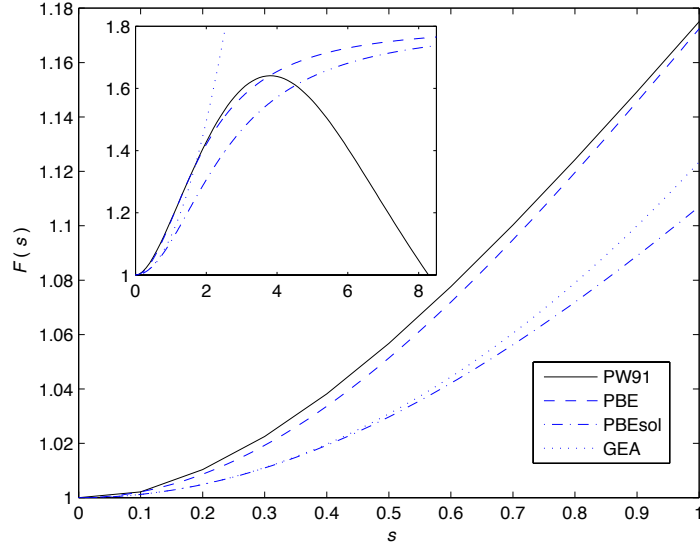
$$\mathcal{H}^{\text{KSD}} = \mathcal{H}' + \mathcal{H}^{\text{SO}}, \quad (5.26)$$

where \mathcal{H}' is called the scalar-relativistic Hamiltonian, and \mathcal{H}^{SO} is the spin-orbit Hamiltonian. In \mathcal{H}' , the quantum numbers L and S can be treated as good quantum numbers.

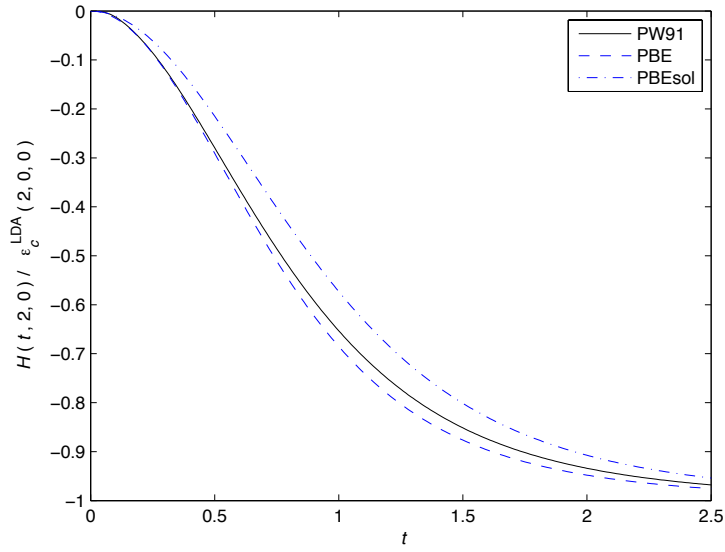
If spin-orbit coupling is expected to be important also for valence-electrons, \mathcal{H}^{SO} is typically added as a perturbation to scalar-relativistic wave functions [40]. Calculations that add spin-orbit coupling in this way for valence electrons are typically referred to as fully relativistic calculations.

³ For $r_s \lesssim 6$, the spin scaling of the PBE exchange energy density may be approximated as [91]: $\epsilon_c^{\text{PBE}}(r_s, \zeta, t) \approx \varphi_2^3 \epsilon_c^{\text{PBE}}(r_s, 0, t/\phi)$.

⁴See the Supplementary Material of Ref. [93] for a comparison of the F -functions.



(a)



(b)

Figure 5.2. (a) GGA correction to the LSDA exchange- and correlation energy densities for $(r_s, \zeta) = (2, 0)$, within the PW91, PBE, PBEsol and GEA forms. (b) shows the correction function to correlation energy density, H , relative to the $t \rightarrow \infty$ value.

5.4 Non-zero temperature

At equilibrium at non-zero temperature, the correct equilibrium \mathbf{n} minimises the functional $\Omega[\mathbf{n}]$, which is equal to the Gibbs's grand potential [84]. The functional has the form [40]:

$$\begin{aligned} \Omega[\mathbf{n}] = & -T \sum_{i=1}^{\infty} \ln[1 + e^{(\mu - \epsilon_i)/T}] - \frac{1}{2} \int \int \frac{n(\mathbf{r})n(\mathbf{r}')}{|\mathbf{r} - \mathbf{r}'|} d\mathbf{r} d\mathbf{r}' \\ & - \sum_{\alpha\beta} \int v_{\alpha\beta}^{\text{xc}}(\mathbf{r}) n_{\beta\alpha}(\mathbf{r}) d\mathbf{r} + \Omega_{\text{xc}}[\mathbf{n}], \end{aligned} \quad (5.27)$$

where μ is the chemical potential, and the elements of the density matrix are given by:

$$n_{\beta\alpha}(\mathbf{r}) = \sum_{i=1}^{\infty} \psi_{i\beta}(\mathbf{r}) \psi_{i\alpha}^*(\mathbf{r}) f_D(\epsilon_i, T), \quad (5.28)$$

ie, by including the Fermi-Dirac distribution function, $f_D = 1/(1 + e^{(\epsilon - \mu)/T})$. The exchange-correlation potential may formally be obtained as:

$$v_{\alpha\beta}^{\text{xc}}(\mathbf{r}) = \frac{\delta}{\delta n_{\beta\alpha}(\mathbf{r})} \Omega_{\text{xc}}[\mathbf{n}]. \quad (5.29)$$

5.5 Performance of exchange-correlation functionals

5.5.1 Equilibrium properties

In Figure 5.3, total energy is shown as a function of the unit cell volume in ferromagnetic bcc-Fe and non-magnetic fcc-Fe. The results are shown as obtained by both the LSDA and PBE-GGA functionals.⁵ As seen in the figure, LSDA somewhat underestimates the equilibrium volume of bcc-Fe. Even more interesting is that LSDA predicts the non-magnetic fcc-solution to be lower in energy at this volume. The equilibrium volume of the non-magnetic fcc-phase is smaller still.

Using instead the PBE-GGA functional, the equilibrium volumes of both the bcc- and fcc-phases are increased. For ferromagnetic bcc-Fe, the equilibrium volume is in fact in good agreement with experiment. At this volume, the bcc-solution is by far the most energetically favourable out of the two. However, it should be noted that close to the experimental volume, LSDA correctly agrees with PBE-GGA, that the magnetic solution is more favourable than the non-magnetic fcc. The magnetic moments obtained in the LSDA and PBE-GGA calculations are 2.15 and 2.23 μ_B , respectively. Thus, at fixed volume, LSDA can be expected to give an accurate description of magnetic systems.

It is also interesting to note, following the discussion in Ref. [6], the magnitude of the reduced gradients, s and t , in different parts of space. Figure 5.4(a) shows

⁵See Appendix B.2 for details of the calculation.

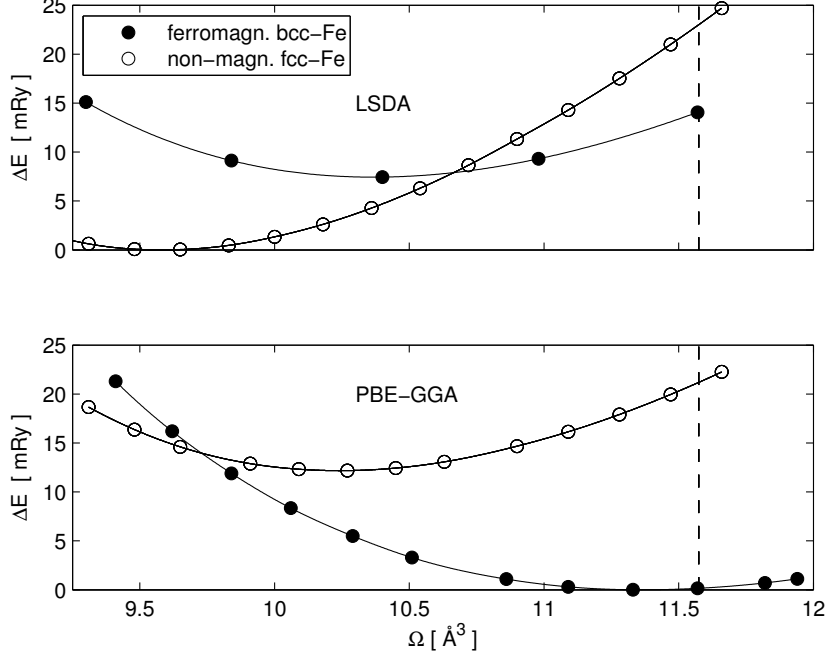


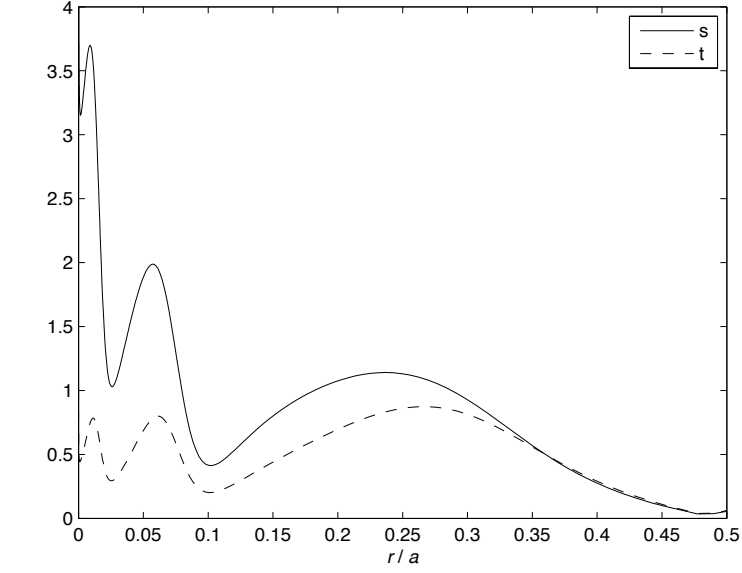
Figure 5.3. Energy versus unit cell volume, Ω , for ferromagnetic bcc-Fe and non-magnetic fcc-Fe obtained with LSDA (top panel) and GGA bottom panel). The vertical dashed lines indicate the experimental unit cell volume of bcc-Fe. See Appendix B for computational details.

those gradients in bcc-Fe, and Figure 5.4(b), shows the corresponding exchange- and correlation-energy densities. It is seen that the major corrections to the LSDA come from regions in space where the major part of the charge is made up of core electrons, according to Figure 2.1.

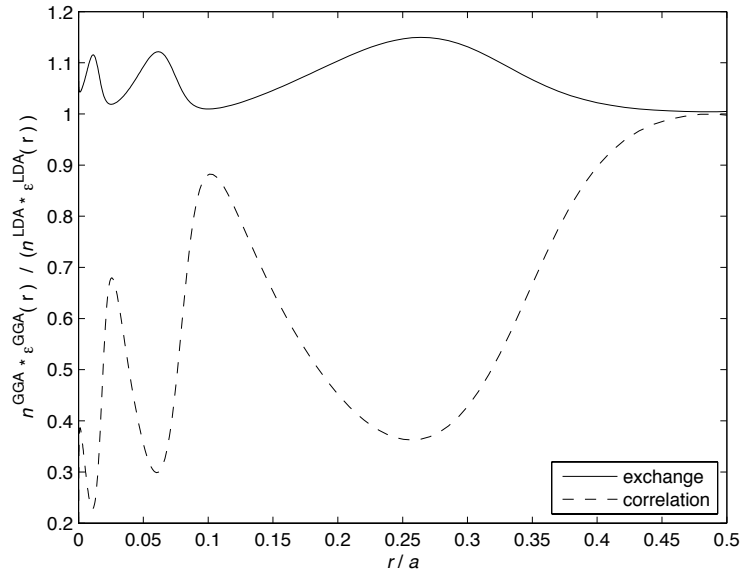
5.5.2 Finite temperature

Compared to its $T = 0$ K counterpart, much less is known about the functional Ω_{xc} , mentioned in Section 5.4, and this an active area of research [104]. In practical calculations, one uses the potential (5.15), assuming it to remain diagonal. Excitations then enter through the Fermi-Dirac function, f_D , in Equation (5.28).

This corresponds to the Stoner excitations discussed in Section 3.6. Such calculations for Fe and Ni typically predict Curie temperatures which roughly are 5 times higher than experimental values [40]. To capture the transverse excitations, one therefore combines DFT calculations with model Hamiltonians for magnetic simulations at finite temperature. In Chapter 8 such models which have been used within this thesis are described.



(a)



(b)

Figure 5.4. (a) reduced gradients s and t in bcc-Fe, with the corresponding exchange-correlation energy (b), based on based on the spherical charge density $n(r)$, plotted in terms of the lattice constant. Calculations were made with the PBE-GGA functional, and in (b), results are shown relative to LSDA results. See Appendix B for computational details.

5.5.3 Strong correlations

Compared to the itinerant electrons in the delocalised s or p orbitals, electrons in d or f states typically show a much higher degree of localisation, and particle-like character. This is a very different situation from the delocalised plane-wave orbitals of the uniform electron gas.

Self-interaction

In the limit where the particle-properties of the electrons reveal themselves, LSDA and the GGAs may not correctly cancel the self-interaction in the Hartree term in Equation (5.17). For the uniform electron gas, this condition is fulfilled by construction, since LSDA it is fitted to that system. Self-interaction correction (SIC) to the LSDA has been investigated by eg, Perdew and Zunger [77], which did improve cohesive energy.

Local Coulomb interaction

Anisimov et al. [105] suggested to describe the Coulomb interaction of the localised states in a different way than in the Kohn-Sham approach. The localised orbitals constitute a subset of orbitals \mathcal{C} , and are described in the orbital and spin basis $|\nu\sigma\rangle$. The Coulomb interaction is then described starting from the general form of Equation (4.5) in this basis:

$$V = \frac{1}{2} \sum_{\sigma_1\sigma_2} \sum_{\nu_1\nu_2\nu_3\nu_4} \langle \nu_3, \nu_4 | V_{ee} | \nu_1, \nu_2 \rangle c_{\nu_3\sigma_1}^\dagger c_{\nu_4\sigma_2}^\dagger c_{\nu_2\sigma_2} c_{\nu_1\sigma_1}, \quad (5.30)$$

where V_{ee} is the *screened* Coulomb interaction.⁶ The Hamiltonian is constructed as:

$$H^{\text{LSDA+U}} = H^{\text{LSDA}} + V^{\text{LSDA+U}}, \quad (5.31)$$

where $V^{\text{LSDA+U}}$ includes a double-counting (DC) correction to avoid counting the same interaction in both terms. The DC-correction cannot be written explicitly in an orbital basis [106], since the LSDA mixes orbitals in a non-linear fashion, and approximate forms are used [106, 107]. One then makes the so-called static mean-field (Hartree-Fock) approximation to the four-operator term [108], which leads to:

$$V^{\text{LSDA+U}} = \sum_{\nu_1\nu_2\sigma} V_{\nu_1\nu_2}^\sigma c_{\nu_1\sigma}^\dagger c_{\nu_2\sigma}, \quad \nu \in \mathcal{C}. \quad (5.32)$$

The expectation value of this operator thus depends on the occupation of each spin-orbital in \mathcal{C} .

There are several parametrisations [109, 110] of the one-electron potential, $V_{\nu_1\nu_2}^\sigma$, of which the one by Dudarev et al. [110] is the most widely used. The matrix elements, involving V_{ee} , are parametrised by averages, frequently referred to as U and J . For this reason, this type of functional has become known as

⁶See Figure 2.3.

L(S)DA+U. Values for U and J can be taken from experiment, based on assuming an atomic character of the real orbitals, or calculated perturbatively [105, 18].

LSDA+U improves on LSDA in many aspects [108]. For the cases of fully occupied and empty orbitals, the one-electron potential takes the values $-U/2$ and $U/2$, respectively. LSDA+U, will lower occupied bands and raise empty bands, which may lead to insulating solutions where LSDA predicts metals. Also, self-interaction error is decreased. However, LSDA+U is still an independent electron method, based on the static Hartree-Fock approximation of the Coulomb interaction in \mathcal{C} [108]. A more extensive use of Equation (5.30), including correlations beyond the static mean-field approximation can be made in quantum Monte-Carlo simulations. This can be performed in electronic structure calculations within the framework described in Chapter 7.

Chapter 6

Computational Methods for the Kohn-Sham Equations

If the external potential has the periodicity in Equation (4.4), Bloch's theorem [111] asserts that the Kohn-Sham orbitals have the form:

$$\psi_{n\mathbf{k}}(\mathbf{r} + \mathbf{R}) = e^{i\mathbf{k}\cdot\mathbf{R}}\psi_{n\mathbf{k}}(\mathbf{r}), \quad (6.1)$$

where n and \mathbf{k} label the eigenvalues as: $\varepsilon_n(\mathbf{k})$. \mathbf{k} can be chosen to lie in the first Brillouin zone (BZ) of reciprocal lattice,¹ which results in a multi-valued function, where the integer n denotes the branch. Equation (6.1) implies that the electronic structure problem only needs to be solved within the unit cell. When calculating integrals over the full BZ, the values of \mathbf{k} can be chosen in a clever way to reduce the required number of points, eg, by the Monkhorst-Pack [112] scheme.

When magnetic interactions bring about a spin-spiral structure, as shown in Figure 3.5, it may seem as if Equation (6.1) would be violated. However, as pointed out by Sandratskii [113]: in the scalar-relativistic limit, the generalised translation operator, T_S , which combines a translation on the lattice by \mathbf{R} with a rotation around the z -axis by the angle $-\mathbf{q}\cdot\mathbf{R}$, has the following effect on the Kohn-Sham orbitals [85]:

$$T_S\psi_{\mathbf{k}}(\mathbf{r}) = e^{-i\mathbf{k}\cdot\mathbf{R}}\psi_{\mathbf{k}}(\mathbf{r}). \quad (6.2)$$

Thus, by applying the associated rotation, translational symmetry is not broken by a spin spiral. This is known as the generalised Bloch theorem [40]. It is thus sufficient to solve the Kohn-Sham equations for the unit cell even for a spin spiral structure.

In order to solve the Kohn-Sham equations, (5.10), 5.12) and (5.14) the Kohn-Sham orbitals can be constructed from a basis set:

$$\psi = \sum_j c_j \nu_j. \quad (6.3)$$

¹ The reciprocal lattice is spanned by the vectors \mathbf{K} , such that $\mathbf{K}_i \cdot \mathbf{a}_j = 2\pi\delta_{ij}$. The first BZ is the WS-cell of the reciprocal lattice.

In addition, the external potential, V^{ext} , which can be very complicated for the case of alloys, must be modelled in an accurate and efficient way. In practice, the sum in Equation (6.3) must be truncated, and the basis orbitals do not form a complete basis. This means that the size of the basis set must be carefully converged.

The choice for the potential and the basis set characterises the computational method. Slater argued already in the youth of electronic structure theory that the wave function would resemble atomic wave functions at the atomic sites, while being rather smooth in between [114]. This led the way to the practice of partitioning space in two kinds of regions, the muffin-tin (MT) spheres of radius R_{MT} , centred on each lattice site; and the interstitial region between the spheres. This is illustrated in Figure 6.1. Suitable basis functions can then be used in the different regions, which are then matched into a well-behaved basis set in the entire space. Depending on the way that the expansion coefficients, c_j , are determined one may divide these computational methods in two categories: Hamiltonian-based methods and Green's function methods.

6.1 Hamiltonian-based methods

In this group of methods, the eigenvalue equation is solved with the basis functions, and takes the form:

$$\sum_j c_{jk} [H_{jk} - \epsilon_k O_{jk}] = 0 \quad \forall j, k, \quad (6.4)$$

in terms of the Hamiltonian matrix:

$$H_{jk} = \langle \nu_j | H^{\text{KS}} | \nu_k \rangle, \quad (6.5)$$

and the overlap integral of the basis functions:

$$O_{jk} = \langle \nu_j | \nu_k \rangle. \quad (6.6)$$

Finding the basis functions which diagonalise the Hamiltonian matrix, one-electron energies and ground state charge density are found.

6.1.1 Augmented Plane Waves

In the interstitial region, the Kohn-Sham wave function can be efficiently expanded in terms of plane waves. However, close to the nuclei, an insurmountable number of plane waves would be needed, since the wave function is strongly oscillatory there. Slater therefore suggested to use plane waves as a basis in the interstitial region, while inside the spheres, the basis set is augmented by a localised radial orbitals; hence the name *augmented plane waves* (APWs) [115, 116].

An APW can be written as:

$$\nu_{\mathbf{K}}^{\mathbf{k}}(\mathbf{r}, \epsilon) = \begin{cases} e^{i(\mathbf{k}+\mathbf{K}) \cdot \mathbf{r}} & \mathbf{r} \notin R_{\text{MT}} \\ \sum_L f_L^{\mathbf{k}+\mathbf{K}}(r, \epsilon) Y_L(\hat{\mathbf{r}}) & \mathbf{r} \in R_{\text{MT}} \end{cases} \quad (6.7)$$

where $L = (\ell, m)$ and Y_L are the spherical harmonics. The radial functions:

$$f_L^{\mathbf{k}+\mathbf{K}} = A_L^{\mathbf{k}+\mathbf{K}} \chi_\ell(r, \epsilon), \quad (6.8)$$

are given by the solutions to the radial Schrödinger equation, χ_ℓ , and the coefficients A . The different solutions then need to be matched into a continuous and differentiable function. A disadvantage of the above expansion is ν depends on the very energy that is being sought, ϵ , through the function $\chi(\epsilon)$. In order to avoid a high number of trial calculations, which would cost computational time [117], it was suggested by Andersen [118] to linearise the energy dependence of the localised orbitals, which makes the system in Equation (6.4) linear. The functions f are thus approximated by a linear expansion:

$$f_L^{\mathbf{k}+\mathbf{K}} = A_L^{\mathbf{k}+\mathbf{K}} \chi_\ell(r, E_\ell) + B_L^{\mathbf{k}+\mathbf{K}} \dot{\chi}_\ell(r, E_\ell) \quad (6.9)$$

where the linearisation energies, E_ℓ , are defined for each orbital. The coefficients A and B are determined by matching the different solutions at the boundary of the muffin-tin sphere. Such a basis function is called a *linearised* augmented plane wave (LAPW) [118].

An alternative way of linearising the APW method was suggested in the work by Sjöstedt, Nordström and Singh [119]. This formalism consists of keeping the form of the APWs in Equation (6.8), which are evaluated at the fixed energies E_ℓ . Local orbitals (lo), g , are then added inside the spheres, defined as:

$$g_L(r) = C_L \chi_\ell(r, E_\ell) + D_L \dot{\chi}_\ell(r, E_\ell), \quad (6.10)$$

at the same fixed energy E_ℓ , as the APWs. This scheme is known as APW+lo. This drastically improves the computational time, as compared to LAPW [120].

Calculations within this thesis based on the Wien2k [121] code employ a combination of these basis functions. A convenient way of specifying the size of the basis set is the product:

$$R_{\text{MT}} \cdot |K|^{\text{max}}, \quad (6.11)$$

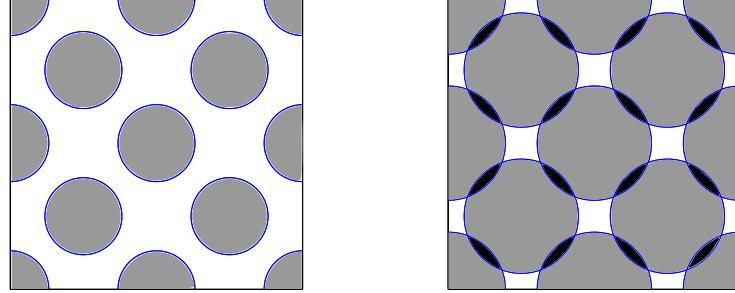
involving the length of the longest reciprocal lattice vector included in the summation of Equation (6.3). This method is a highly accurate expansion of the Kohn-Sham orbitals, and no approximations need to be made for the shape of the potential, which makes it a *full-potential* method.

6.1.2 Projector Augmented Waves

The projector augmented waves (PAW) method, suggested by Blöchl [122], is another way of reducing the number of plane waves needed in the expansion of Equation (6.3). The basic idea is to map wavefunctions onto smooth auxiliary wavefunction, $|\tilde{\psi}\rangle$, as:

$$|\psi\rangle = \mathcal{T}|\tilde{\psi}\rangle, \quad (6.12)$$

with a linear transformation operator, \mathcal{T} [123]. The smooth auxiliary wavefunctions can be efficiently expanded using plane waves.



(a) Non-overlapping muffin-tin spheres

(b) Overlapping muffin-tin spheres

Figure 6.1. Illustration of muffin-tin spheres, drawn as grey circles on a two-dimensional equivalent of the fcc lattice. The region between the spheres, shown as white, is called the interstitial region. In (b), the volume of the muffin-tin spheres equals the unit cell volume, resulting in some overlap regions, indicated in black.

The transformation operator is constructed starting from *partial waves*, χ_ς , defined around a particular lattice site, ς , which are solutions to the radial Schrödinger equation for isolated atoms. Core electrons are handled slightly differently from the valence electrons. In the employed implementation, the frozen core approximation is made, where the core charge density is taken from an atomic calculation.² These atomic calculations can be done once and for all with high accuracy, and then taken from a data base for use in electronic structure calculations. Furthermore, partial waves can be transformed into *auxiliary* partial waves, $|\tilde{\chi}_k\rangle$, which are required to equal the original partial waves outside the MT-region:

$$\chi_i(\mathbf{r}) = \tilde{\chi}_i(\mathbf{r}), \quad |\mathbf{r} - \mathbf{b}_\varsigma| > R_{\text{MT}}, \quad (6.13)$$

as illustrated in Figure 6.2. The local contributions to \mathcal{T} can be defined by:

$$|\chi_k\rangle = (\mathbf{1} + \mathcal{S}_\varsigma)|\tilde{\chi}_k\rangle, \quad k \in \varsigma, \quad (6.14)$$

where the operator is written as:

$$\mathcal{S}_\varsigma|\tilde{\chi}_k\rangle = |\chi_k\rangle - |\tilde{\chi}_k\rangle. \quad (6.15)$$

Inside the MT-spheres, the auxiliary wave function can be expanded in the corresponding auxiliary partial waves:

$$\tilde{\psi}(\mathbf{r}) = \sum_{i \in \varsigma} c_i \tilde{\chi}_i(\mathbf{r}), \quad |\mathbf{r} - \mathbf{b}_\varsigma| < R_{\text{MT}}. \quad (6.16)$$

The expansion coefficients define the so-called projector functions, \tilde{p} , as:

$$c_i = \langle \tilde{p}_i | \tilde{\psi} \rangle, \quad (6.17)$$

²Recent implementations of the PAW method allow this approximation to be relaxed.

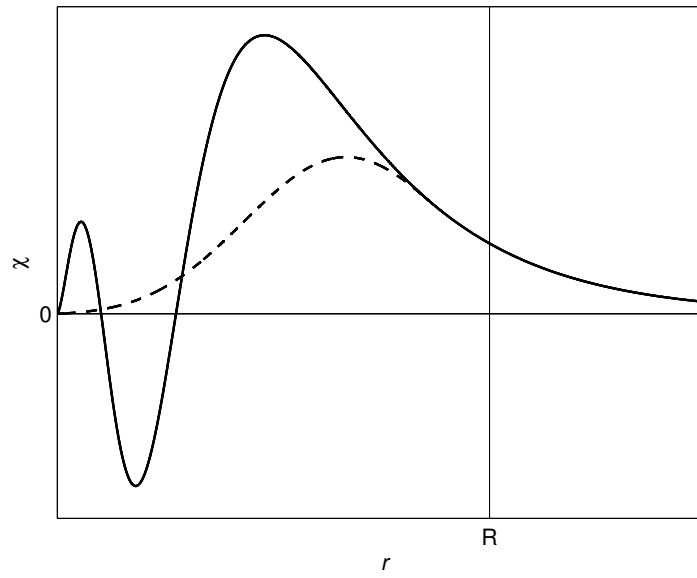


Figure 6.2. Illustration of the pseudopotential transformation of the projector augmented waves method. The strongly oscillating all-electron wave function, (solid line) is replaced by a smooth function (dashed line), which is equal to the all-electron wave function outside the muffin-tin sphere, ie, for $r > R$. The smooth wave function is related to the all-electron wave function by a linear transformation, \mathcal{T}_R .

which are constructed from the auxiliary partial waves [122]. Following Ref. [123], the transformation operator is written as a sum of atomic contributions from each site, ς :

$$\mathcal{T} = \mathbf{1} + \sum_{\varsigma} \mathcal{S}_{\varsigma} \quad (6.18)$$

$$= \mathbf{1} + \sum_{\varsigma} \sum_{i \in \varsigma} (|\chi_i\rangle - |\tilde{\chi}_i\rangle) \langle \tilde{p}_i|. \quad (6.19)$$

With this operator, full Kohn-Sham orbitals can be recovered from the smooth auxiliary wave functions via Equation (6.12). Calculations can thus be performed using smooth functions expanded with plane waves.

PAW-calculations within this thesis have been carried out using the Vienna ab-initio simulation package (VASP) [124, 125, 126, 127, 128]. The size of the basis set is given in terms of the energy of the included plane waves, which is determined by their wave vectors as: $\varepsilon(K) = \frac{1}{2}K^2$. An energy cut-off, ε_{cut} , is chosen such that:

$$|\mathbf{K} + \mathbf{k}| < K_{\text{cut}}, \quad (6.20)$$

where \mathbf{k} denotes the sampled points of reciprocal space [129].

6.2 Green's function method

The method by Korringa, Kohn and Rostocker³ [130, 131] (KKR) was developed as an alternative strategy to solving the Kohn-Sham equations, based on the formalism of scattering-theory [132, 133]. However, for band structure calculations, it suffers the same drawbacks as the APW-method [118, 134, 135], and linear full-potential methods have consequently been developed, originating in the KKR-approach [136].

Another line of development is the Green's function formulation of the KKR-method. The essence is that instead of trying to diagonalise the Hamiltonian matrix, one determines the Green's function, G , associated with the Kohn-Sham Hamiltonian:

$$(\mathcal{H}^{\text{KS}} - \varepsilon_i) G(\mathbf{r}, \mathbf{r}', \varepsilon) = -\delta(\mathbf{r} - \mathbf{r}'). \quad (6.21)$$

To evaluate G , it is practical to relate it to a reference Green's function. The Green's function, G_0 , corresponding to a free-particle Hamiltonian is a suitable choice. Each atomic potential v_i is then considered a scattering center of electron waves. The operator t^i , which can be related to the potential as:

$$t^i = \frac{v_i}{\mathbf{1} - v_i G_0}, \quad (6.22)$$

operates on a wave incident on the site i , to produce a scattered wave [137]. More generally, the *scattering path operator*, τ^{ij} , acts on a wave incident on site i , and describes the wave as it emerges from site j , going through all possible scattering paths in between [138], as illustrated in Figure 6.3. It can be written in terms of

³This method was conceived independently by Korringa before the work of Kohn and Rostocker was published.

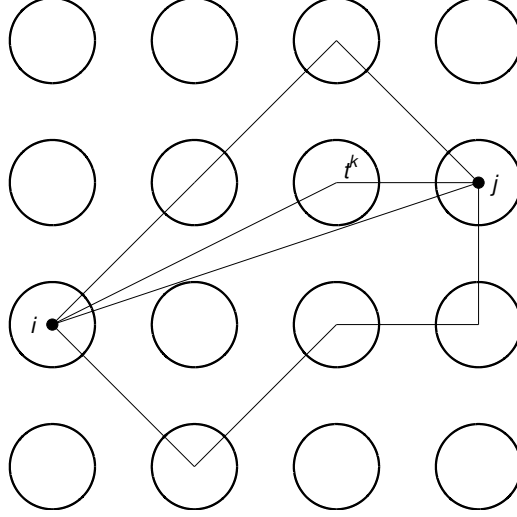


Figure 6.3. Illustration of the multiple scattering formalism. A wave emerges from site i and may go through a number of different scatterings before reaching site j . The influence of all scattering events between i and j is encoded by the scattering path operator, τ^{ij} . Scattering from a single site, k , is described by the t -matrix, t^k , linked to the potential at site k .

the reference Green's function and the t -matrix:

$$\tau_{ij} = t^i \delta_{ij} + \sum_{k \neq j} \tau^{kj} G_0 t^j. \quad (6.23)$$

Summing the scattering paths between all sites, the Green's function can be expressed as:

$$G = G_0 + G_0 \sum_{ij} \tau^{ij} G_0. \quad (6.24)$$

Once the Green's function has been calculated, spectral information, such as DOS, can readily be extracted from its imaginary part. Furthermore, as an alternative to Equation (5.10), the charge density, $n(\mathbf{r})$, can be obtained as [139]:

$$n(\mathbf{r}) = -\frac{2}{\pi} \int_{-\infty}^{\epsilon_F} d\epsilon \operatorname{Im} G(\mathbf{r}, \mathbf{r}, \epsilon), \quad (6.25)$$

and the sum of the eigenvalues, ϵ_i , which are poles of $G(\epsilon)$, can be obtained in a similar integral. Total energy can then be evaluated using Equation (5.17).

Equation (6.25) is most efficiently evaluated for complex energy:

$$z = \varepsilon + iy, \quad (6.26)$$

as a contour integral [134]. In the calculations, the Green's function can be expressed in an energy-dependent basis, and high accuracy may be obtained. Additionally, as will be shown in Section 6.3.2, this approach is highly suited to deal with disordered systems.

6.2.1 Exact Muffin-Tin Orbitals

In the so-called muffin-tin (MT) *potential* approximation, the effective potential is taken as a superposition of spherically symmetric potentials $V(r)$ inside the MT spheres, and a constant potential outside, V_0 , called the muffin-tin zero:

$$V_{\text{eff}}(\mathbf{r}) = V_0 + \sum_{\varsigma} [V^{\varsigma}(r_{\varsigma}) - V_0], \quad (6.27)$$

where r_{ς} is the modulus of the vector $\mathbf{r}_{\varsigma} = \mathbf{r} - \mathbf{b}_{\varsigma}$, following Equation (1.3). The spherically symmetric potentials thus have the property: $V_{\varsigma}(r_{\varsigma}) = V_0$ for $r_{\varsigma} > R_{\text{MT}}^{\varsigma}$. By using overlapping potential spheres, as shown in Figure 6.1(b), the description of the crystal potential can be improved as compared to using non-overlapping potential spheres [140].

If V^{ς} and V_0 are optimised to yield the best possible approximation to V_{eff} , one can construct an exact expansion of the Kohn-Sham orbitals, without linearisation or requiring the core states to be fixed in energy, called exact muffin-tin orbitals (EMTOs). In the employed implementation, the MT radii are kept to predefined values during the self-consistency cycle. These are defined for each site ς and as before, $L = (\ell, m)$, where $\ell = 0, 1, 2, 3, \dots$ denotes s, p, d, f, \dots EMTOs, which are included up to $\ell = \ell_{\text{max}}$ in the expansion of Equation (6.3).

Inside the muffin-tin spheres, another set of spheres called *hard-spheres* with radius R_a^{ς} are defined. The relation of the hard-spheres and the muffin-tin potential spheres is illustrated in Figure 6.4, which shows that the hard-spheres are non-overlapping. Just like the muffin-tin potential spheres, the radii of hard-spheres may be different for different sites in the unit cell, and even for different ℓ -numbers, although this has been omitted in the discussion below for the sake of simplicity. The EMTOs are then formed as a superposition of wave functions defined in different parts of space, as described below.

Partial waves

The partial waves are defined inside the muffin-tin potential spheres, $r \leq R_{\text{MT}}$. For a particular site, ς , they are formed as the product of the solutions, χ , to the radial Schrödinger equation:

$$\left[-\frac{1}{2}\nabla^2 + V(r) \right] \chi_{\ell}(\epsilon, r) = \epsilon \chi_{\ell}(\epsilon, r) \quad (6.28)$$

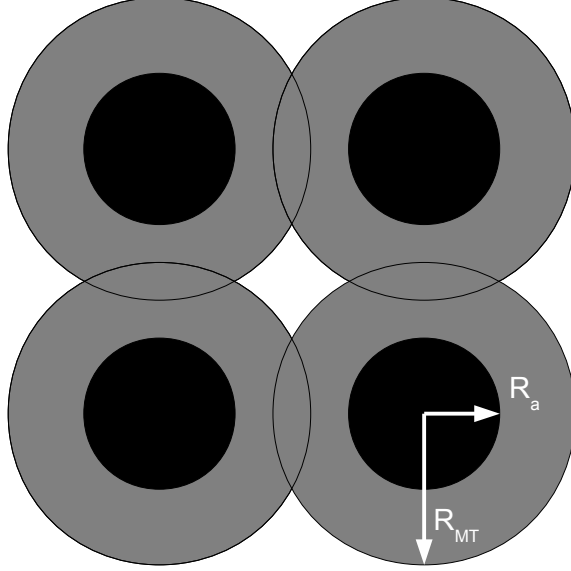


Figure 6.4. Partition of space within the EMTO method. An EMTO basis function is a superposition of several basis sets, defined in different regions of space. The grey circles denote the overlapping potential spheres, which contain the non-overlapping hard-spheres, shown in black. The partial waves, $\bar{\chi}$, are defined within the potential spheres (black and grey regions), and the screened spherical waves, v , are defined outside the hard-spheres (black). In the grey areas, free-electron solutions, φ are defined, which match the screened spherical waves with the partial waves at the potential- and hard-sphere boundaries.

as:

$$\bar{\chi}_L(z, \mathbf{r}) = N_\ell(z) \chi_\ell(z, r) Y_L(\hat{\mathbf{r}}), \quad (6.29)$$

where $Y_L(\hat{\mathbf{r}})$ denotes a so-called real harmonics function, which are linear combinations of the spherical harmonics, and $N_\ell(z)$ is a normalisation function.

Screened spherical waves

The screened spherical waves, $v_L(\mathbf{r}, \kappa^2)$, are defined outside the hard spheres, $r \geq R_a$, as solutions to the equation:

$$\frac{1}{2} \nabla^2 v_L(\mathbf{r}, \kappa^2) = -\kappa^2 v_L(\mathbf{r}, \kappa^2), \quad (6.30)$$

where $\kappa^2 = z - V_0$. They form a complete basis set in the region outside the hard-spheres [141], and can be expanded in terms of spherical harmonics centred

at any site, ς' , as:

$$\begin{aligned} v_L^\varsigma(\mathbf{r}_\varsigma, \kappa^2) &= f_\ell^\varsigma(\kappa^2, r_\varsigma) Y_L(\hat{\mathbf{r}}_\varsigma) \delta_{LL'} \delta_{\varsigma\varsigma'} \\ &+ \sum_{L'} g_{\ell'}^{\varsigma'}(\kappa^2, r_{\varsigma'}) Y_{L'}(\hat{\mathbf{r}}_{\varsigma'}) S_{\varsigma L \varsigma' L'}(\kappa^2), r \geq R_a \end{aligned} \quad (6.31)$$

where f and g are called the head- and tail-functions, respectively, which may be expressed as linear combinations of the spherical Bessel and Neumann functions. The head- and tail-functions ensure that the boundary conditions [141, 142]:

$$\begin{cases} v_L^\varsigma(R_a, \kappa^2) = Y_L(\hat{\mathbf{r}}_{\varsigma'}) & , \varsigma = \varsigma' \\ \int \delta(r_{\varsigma'} - R_a) Y_{L'}^*(\hat{\mathbf{r}}_{\varsigma'}) v_L^\varsigma(\mathbf{r}_\varsigma, \kappa^2) d\mathbf{r}_{\varsigma'} = 0 & , \varsigma \neq \varsigma' \end{cases} \quad (6.32)$$

are fulfilled. \mathbf{S} is called the *slope matrix*, which contains all information needed about the crystal structure.

Joining the solutions

As explained in Figure 6.4, the partial waves and the screened spherical waves co-exist in certain regions, along with the free electron radial orbitals, φ_ℓ^ς . The superposition of these wave functions:

$$v_L^\varsigma(\kappa^2, \mathbf{r}_\varsigma) + [\bar{\chi}_L^\varsigma(z, \mathbf{r}_\varsigma) - \varphi_\ell^\varsigma(z, r_\varsigma) Y_L(\hat{\mathbf{r}}_\varsigma)] \theta(r - R_{\text{MT}}) \quad (6.33)$$

is thus a triple-valued function in the region $R_a < r < R_{\text{MT}}$. The free-electron solutions can be written as:

$$\varphi_\ell^\varsigma(z, \mathbf{r}_\varsigma) = [f_\ell^\varsigma(\kappa^2, r_\varsigma) + g_\ell^\varsigma(\kappa^2, r_\varsigma) D_\ell^\varsigma(\epsilon)] Y_L(\hat{\mathbf{r}}_\varsigma) \quad (6.34)$$

where the elements of the matrix \mathbf{D} is given by the expression:

$$D_\ell^\varsigma(z) = -\frac{f_\ell^\varsigma(R_{\text{MT}}, \kappa^2)}{g_\ell^\varsigma(R_{\text{MT}}, \kappa^2)} \frac{\mathcal{D}\{\chi_\ell^\varsigma(R_{\text{MT}}, z)\} - \mathcal{D}\{f_\ell^\varsigma(R_{\text{MT}}, \kappa^2)\}}{\mathcal{D}\{\chi_\ell^\varsigma(R_{\text{MT}}, z)\} - \mathcal{D}\{g_\ell^\varsigma(R_{\text{MT}}, \kappa^2)\}}, \quad (6.35)$$

in terms of the logarithmic derivatives:

$$\mathcal{D}\{\mathcal{A}(r)\} \equiv \frac{r}{\mathcal{A}} \frac{\partial}{\partial r} \mathcal{A}, \quad (6.36)$$

evaluated at the potential sphere boundary.

The free electron solutions join the partial waves and screened spherical waves continuously at R_a , and continuously and differentially at R_{MT} . It can be shown [141, 143] that this is achieved when following condition is fulfilled:

$$\mathbf{K}(z)\mathbf{c} \equiv R_a [\mathbf{D}(z) - \mathbf{S}(z)] \mathbf{c} = 0. \quad (6.37)$$

The real energies, $z = \epsilon_j$, for which Equation (6.37) has non-trivial solutions are the Kohn-Sham single electron energies for the muffin-tin potential. These energies are the poles of the Green's function.

Obtaining the Green's function

In order to obtain the Green's function, the path operator, $\tau_{LL'}^{\zeta\zeta'}(z)$, can be calculated as:

$$\sum_{\zeta'L'} K_{L'L}^{\zeta\zeta'}(z) \times \tau_{LL'}^{\zeta\zeta'}(z) = \delta_{\zeta\zeta'} \delta_{LL'} \quad (6.38)$$

whereupon the Green's function can be written as:

$$G(z) = \sum_{\zeta L \zeta' L'} \tau_{LL'}^{\zeta\zeta'}(z) \dot{K}_{LL'}^{\zeta\zeta'}(z) - \sum_{\zeta L} \left(\frac{\dot{D}_{\zeta}^{\zeta}(z)}{D_{\zeta}^{\zeta}(z)} - \sum_d \frac{1}{z - \epsilon'_d} \right), \quad (6.39)$$

where overdots denote derivatives with respect to energy, and ϵ'_d are the real-valued energies such that $D(\epsilon'_d) = 0$.

Full charge-density technique

In order to accurately evaluate, eg, total energy, the integrals in Section 5.1 must be taken over the non-spherical and non-overlapping Wigner-Seitz cells [144]. Having determined the charge density as:

$$n(\mathbf{r}) = \sum_{\zeta} n^{\zeta}(\mathbf{r}_{\zeta}), \quad (6.40)$$

where

$$n^{\zeta}(\mathbf{r}_{\zeta}) = \sum_L n_L^{\zeta}(r_{\zeta}) Y_L(\hat{\mathbf{r}}_{\zeta}), \quad (6.41)$$

the MT-approximation to the potential can be used to construct the functional in Equation (5.17) with an accuracy comparable to full-potential methods [143]. This can be accomplished by the full charge-density (FCD) technique [145].

With this formalism, integrals involving the charge density and a function $\mathcal{A}(\mathbf{r})$ may be taken over a sphere of radius S_c , circumscribing the Wigner-Seitz cell, to reproduce integrals over the Wigner-Seitz polyhedron:

$$\int_{\Xi} n(\mathbf{r}) \mathcal{A}(\mathbf{r}) d\mathbf{r} = \sum_L \int_0^{S_c} \tilde{n}(r)_L \mathcal{A}_L(r) r^2 dr, \quad (6.42)$$

where:

$$\mathcal{A}_L(r) \equiv \int \mathcal{A}(\mathbf{r}) Y_L(\hat{\mathbf{r}}) d\hat{\mathbf{r}}. \quad (6.43)$$

In Equation (6.42), \tilde{n} is a radial density function that can be written in terms of the real Gaunt coefficients, C , as [143]:

$$\tilde{n}_L(r) = \sum_{L'L''} C_{LL'L''} n_{L'}(r) \sigma_{L''}(r), \quad (6.44)$$

with the partial components of the so-called shape-functions:

$$\sigma_L(r) \equiv \int \sigma(\mathbf{r}) Y_L(\mathbf{r}) d\hat{\mathbf{r}}. \quad (6.45)$$

The shape functions, σ , are step functions nonzero only inside the Wigner-Seitz cell, and can be calculated once and for all for a particular crystal structure, just like the slope matrix.

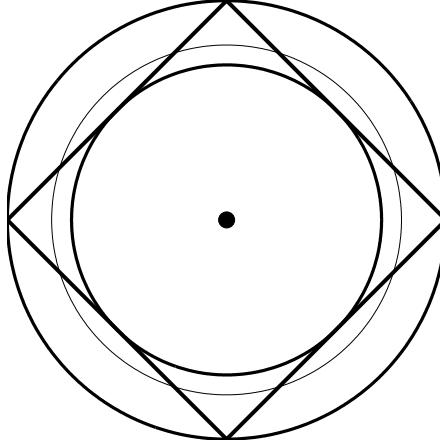


Figure 6.5. Illustration of the relation between the WS cell (bold straight lines) around a lattice site, and the circumscribing sphere of radius S_c . The thin line is the so-called ASA-sphere with radius $S < S_c$. The inscribed sphere of radius $S_i < S$, which is completely contained inside the WS cell is also shown.

6.3 Modelling random alloy potentials

In alloys where the configuration is disordered, as illustrated in Figure 1.1(b), the translational symmetry in Equation (4.4) does not hold, and Bloch's theorem (6.1) is consequently invalidated. There are two common strategies to handle random alloys: supercells and effective medium methods, which restore Equation (6.1).

6.3.1 Special quasirandom structures

In supercell methods, a large unit cell is constructed, which is repeated in space, so that periodic boundary conditions are imposed. To simulate random alloys, an efficient prescription is the special quasirandom structure (SQS) proposed by Zunger et al. [146]. The idea is to construct a single structure that yields configurationally averaged quantities, such as total energy, that resemble those of perfectly random alloys. Constructing such a supercell would require detailed knowledge of the atomic interactions in the solid. It is common to assume that the most significant interactions for total energy around a particular atom decay rather quickly

over distance, a principle known as near-sightedness [86]. Although a rigorous construction of an SQS would start by an investigation of the atomic interactions, the common approach is to ensure that the short-range order parameters are vanishing for the first few coordination shells [6].

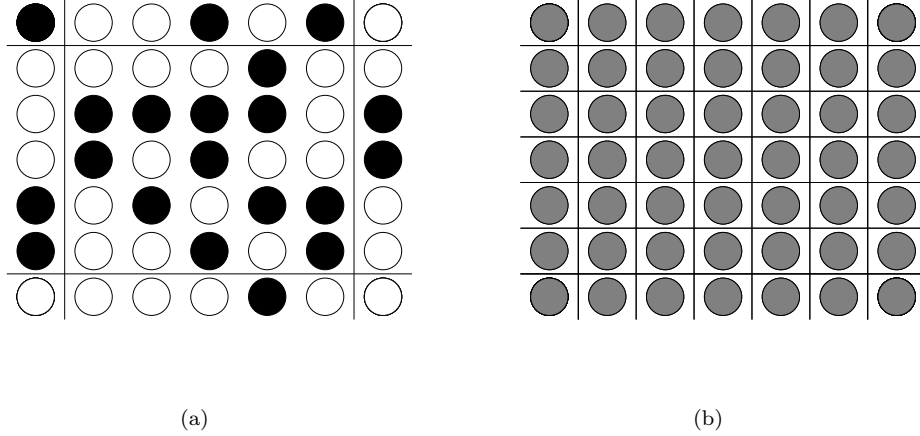


Figure 6.6. Illustration of a random binary alloy within the supercell (a) and effective medium (b) models. In both cases, the unit cell is repeated in space, imposing periodic boundary conditions.

6.3.2 Coherent Potential Approximation

Effective medium methods mean that instead of using a supercell, the atomic potentials are replaced with an effective potential medium, \tilde{v} . This reduces the size of the unit cell, as illustrated in Figure 6.6. In the coherent potential approximation (CPA) [147], the potential is determined self-consistently within the Green's function formalism by considering each potential well as a scatterer of electron waves. The scattering from a single real potential embedded in the effective medium should be coherent with the effective medium. This is accomplished if the scattering-path operator of the medium, $\tilde{\tau}$, fulfils the condition [138]:

$$\tilde{\tau} = \sum_p c_p \tau_p^{nn}, \quad (6.46)$$

where c_p is the concentration of the p :th alloy component. Within the EMTO framework, the potential enters through the D matrices, so that:

$$\tau_p^{nn} = \frac{\tilde{\tau}}{1 + \tilde{\tau} [D_p - \tilde{D}]}. \quad (6.47)$$

This means that the coherent scattering path operator can be calculated as:

$$\tilde{\tau} = \frac{1}{\Omega_{BZ}} \int_{\Omega_{BZ}} \frac{d\mathbf{k}}{S(z, \mathbf{k}) - \tilde{D}(z)}, \quad (6.48)$$

from the slope matrix, S . These equations are solved self-consistently for $\tilde{\tau}$, which replaces the ordinary scattering path operator, τ , in Equation (6.39) [143].

Screened impurity model

In order to derive a functional for the total energy within the CPA, it should be noted that when space is divided in MT-spheres, the spheres will not be electroneutral, and charge is distributed in two regions as

$$Z_p = q_p + \int_S^\infty d\mathbf{r} \frac{n(\mathbf{r})}{|\mathbf{r} - \mathbf{r}'|} \quad (6.49)$$

where q_p is the charge of the MT-sphere:

$$q_p = \int_{\Xi} d\mathbf{r} n_p(\mathbf{r}). \quad (6.50)$$

When the Kohn-Sham equations are solved for the p -th sphere, it will not be electroneutral, the remaining charge will be distributed outside the sphere. However, the missing charge will be absorbed into the surrounding identical spheres with averaged charges. The interaction of the missing charge and q_p will then be missing in the description of total energy, resulting in an error. To remedy this drawback, it was suggested in Refs. [148, 149, 150] to describe q_p as an impurity in the CPA medium, that is screened by the missing charge beyond the first coordination shell.

The potential inside the sphere v^p , can then be corrected with a term, Δv , resulting in the effective potential:

$$\tilde{v}^p = v^p + \Delta v^p. \quad (6.51)$$

The necessary correction to the potential can be written as:

$$\Delta v^p = -\alpha_p^{(1)} \frac{q_p}{S} \quad (6.52)$$

where $\alpha_p^{(1)}$ is called the *on-site* screening constant, and is ≤ 1 . Thus, the energy is given as a screened interaction between a test charge and the net charge q , where α accounts for the effectiveness of the screening. The corresponding shift to the total energy involves a second parameter, β , as:

$$E^{\text{CPA}} = \bar{E} - \sum_p c_p \alpha_p^{(1)} \beta_p \frac{q_p^2}{2S}, \quad (6.53)$$

where \bar{E} is the configurationally averaged energy determined. Just like $\alpha_p^{(1)}$, the second constant, β_p , is determined in supercell calculations.

6.3.3 Locally Self-Consistent Green's function method

In the locally self-consistent Green's function (LSGF) method, suggested by Abrikosov et al. [151, 152], a supercell is constructed with a predetermined set of correlation functions. Around each site in the supercell, a local interaction zone (LIZ) [153] is constructed, and the region outside the LIZ is described by the CPA effective medium, as shown in Figure 6.7. The electronic structure problem is thus decomposed into N locally self-consistent problems [151]. Guided by the principle of near-sightedness, it has been found that good accuracy can be obtained by solving the multiple-scattering problem for a local interaction zone including the first few coordination shells.

Although the local problem scales as $\mathcal{O}(N_{\text{LIZ}}^3)$, the scaling of the whole problem is $\mathcal{O}(N)$, with a prefactor determined by the size of the LIZ. This allows very large supercells to be used at a low computational cost, while local environment effects can be investigated. Limiting the LIZ to only include the central atom corresponds to the single-site approach of CPA, although charge transfer is handled exactly, which lets the accuracy of the screened impurity model to be assessed. The LSGF method was recently implemented in the EMTO basis set [154].

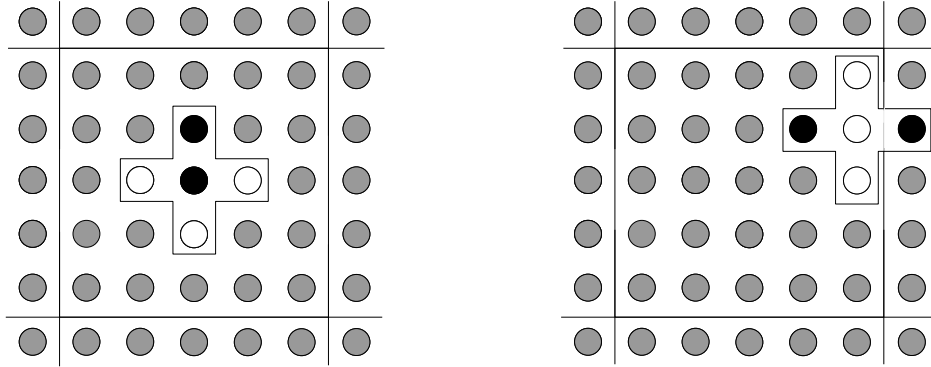


Figure 6.7. Principle behind LSGF method applied to the supercell in Figure 6.6. A LIZ consisting of the first coordination shell is shown for two different sites in the supercell.

Chapter 7

Dynamical Mean Field Theory

In order to handle electron correlations beyond a mean-field level, DFT can be combined with model schemes, such as dynamical mean-field theory (DMFT). This is known as LDA+DMFT, and was developed by Georges et al.[155] A predefined subset of the orbitals are then treated with explicit many-body simulations, to find the equilibrium state at finite temperature.

7.1 Quantum impurity model

In DMFT, one defines a subspace, \mathcal{C} , of the total Hilbert space, to which the correlated orbitals belong. These orbitals thus form a many-body lattice problem. This is mapped onto an auxiliary system of a single impurity atom¹ at \mathbf{R} coupled to a bath, representing the rest of the system. The orbitals of the electrons at the impurity, $|\chi_{\mathbf{R}m}\rangle$, span the subspace, \mathcal{C} , of the full Hilbert space. In \mathcal{C} , many-body interactions are then treated beyond a mean-field level.

7.1.1 The local Green's function

The Green's function of the solid:

$$G(\mathbf{r}t, \mathbf{r}'t'),$$

specifies the probability amplitude of a particle being created at \mathbf{r}' at time t' , and destroyed at \mathbf{r} at later time t . It is convenient to take $t' = 0$, since G only depends on the difference $t - t'$. At finite temperature, $\beta = 1/T$, it is convenient to work with the Matsubara Green's function, which is defined for the imaginary time:

$$\tau = it. \tag{7.1}$$

¹Recent developments of DMFT include *clusters* of atoms, but this method has not been used within this thesis.

The Fourier transformed Green's function, $G(\mathbf{k}, i\omega)$ is non-zero only for:

$$\omega_n = \pi \frac{2n+1}{\beta}, n \in \mathbb{Z}. \quad (7.2)$$

In the basis of non-interacting eigenstates, the full Green's function can be related to a non-interacting reference electron spectrum, $\varepsilon_{\mathbf{k}}$, as:

$$G(\mathbf{k}, z) = \sum_{\mathbf{k}} \frac{1}{i\omega_n + \mu - \varepsilon_{\mathbf{k}} - \Sigma(\mathbf{k}, z)}, \quad (7.3)$$

where μ is the chemical potential and Σ is the self-energy. A reference Green's function can also be written as:

$$G_{\text{KS}}(i\omega_n, \mathbf{k}) = \frac{1}{i\omega_n + \mu - \varepsilon_{\mathbf{k}}}. \quad (7.4)$$

The local part of the Green's function G , corresponding to the subspace \mathcal{C} , can be obtained by the projection:

$$G_{\text{loc}} = P_{\mathbf{R}}^{\mathcal{C}} G P_{\mathbf{R}}^{\mathcal{C}} \quad (7.5)$$

where the projection operator is defined as:

$$P_{\mathbf{R}}^{\mathcal{C}} \equiv \sum_{m \in \mathcal{C}} |\chi_{\mathbf{R}m}\rangle \langle \chi_{\mathbf{R}m}|, \quad (7.6)$$

in terms of the basis $|\chi_{\mathbf{R}m}\rangle$, that spans \mathcal{C} .

7.1.2 The impurity Green's function

The mean-field approximation

As the coordination, d , of the lattice where the electrons may move about reaches infinity, the self-energy in Equation (7.3), becomes independent of \mathbf{k} :

$$\Sigma(\mathbf{k}, i\omega_n) \longrightarrow \Sigma(i\omega_n), d \longrightarrow \infty \quad (7.7)$$

and is purely local, ie, it only depends on the orbitals treated as strongly correlated [156]. This means that the correlated subspace, \mathcal{C} , is an impurity in the mean-field, described by the bath Green's function, $\mathcal{G}_0(z)$, which gives the probability amplitude of an electron being created at the impurity at time τ and destroyed at time τ' . It can be related to the so-called hybridisation function, $\Delta(i\omega)$, as:

$$\Delta(i\omega_n) = i\omega_n - \varepsilon_{\mathbf{k}} - \mathcal{G}_0^{-1}(i\omega_n). \quad (7.8)$$

Quantum impurity problem

The impurity self-energy, Σ_{imp} , is related to the impurity Green's function as:

$$\Sigma_{\text{imp}}(i\omega_n) = \mathcal{G}_0(i\omega_n)^{-1} - G_{\text{imp}}(i\omega_n)^{-1}. \quad (7.9)$$

The impurity Green's function, G_{imp} , describes the temporal correlation between the electrons on the impurity:

$$\mathcal{T} d_{m\sigma}(\tau) d_{m'\sigma'}^\dagger(0).$$

This is equivalent to the Anderson impurity model [157], which in a general form corresponds to the Hamiltonian:

$$\begin{aligned} \mathcal{H} &= \mathcal{H}_{\text{bath}} + \mathcal{H}_{\text{hyb}} + \mathcal{H}_{\text{loc}} \\ &= \sum_{k,\alpha} \varepsilon_{k,\alpha} c_{k,\alpha}^\dagger c_{k,\alpha} \\ &+ \sum_{k,\alpha} \left[\Lambda_{k,\alpha} c_{k,\alpha}^\dagger d_\alpha + \Lambda_{k,\alpha}^* d_\alpha c_{k,\alpha}^\dagger \right] \\ &+ \mu \sum_\alpha d_\alpha^\dagger d_\alpha + \frac{1}{2} \sum_{\nu_1 \nu_2 \nu_3 \nu_4} V_{\nu_1 \nu_2 \nu_3 \nu_4} d_{\nu_3}^\dagger d_{\nu_4}^\dagger d_{\nu_2} d_{\nu_1}, \end{aligned} \quad (7.10)$$

where d^\dagger operates in \mathcal{C} and c^\dagger operates outside \mathcal{C} [158]. Λ is a hybridisation matrix which describes the coupling between the impurity and the bath, which can be related to the hybridisation function as [158]:

$$\Delta_{\alpha\beta}(i\omega_n) = \sum_k \frac{\Lambda_{k,\alpha} \Lambda_{k,\beta}^*}{i\omega_n + \varepsilon_{k,\alpha}}. \quad (7.11)$$

The final term in Equation (7.10) corresponds to Equation (5.32) in the LSDA+U Hamiltonian. However, in DMFT, the Hartree-Fock approximation is not made to the four-operator term. In the employed implementation, the vertex $V_{\nu_1 \nu_2 \nu_3 \nu_4}$ is fully specified by the parameters U and J , which must be calculated in auxiliary calculations [18].

To find the average of the Green's function at temperature β , a quantum Monte-Carlo (QMC) simulation is done, in which the partition function corresponding to the Hamiltonian:

$$Z = \text{Tr} \mathcal{T}_\tau e^{-\mathcal{H}}, \quad (7.12)$$

is sampled stochastically. Within this thesis, the continuous time quantum Monte-Carlo (CT-QMC) [159, 160] has been used.

Once the local self-energy, $\Sigma_{\text{imp}}(i\omega_n)$, has been determined, it is unfolded:

$$\Sigma(\mathbf{k}, i\omega_n) = P^*(\mathbf{k}) \Delta \Sigma(i\omega_n) P(\mathbf{k}), \quad (7.13)$$

where

$$\Delta \Sigma = \Sigma_{\text{imp}} - \Sigma_{\text{DC}}. \quad (7.14)$$

Σ_{DC} is a double-counting correction that needs to be included if the same interaction is treated in both the reference spectrum $\varepsilon_{\mathbf{k}}$ and in \mathcal{C} , in the same way as discussed in Section 5.5.3. The unfolded self-energy in Equation (7.13) is then used to approximate the \mathbf{k} -dependent self-energy in Equation (7.3). In actual calculations these equations are solved iteratively until self-consistency is reached.

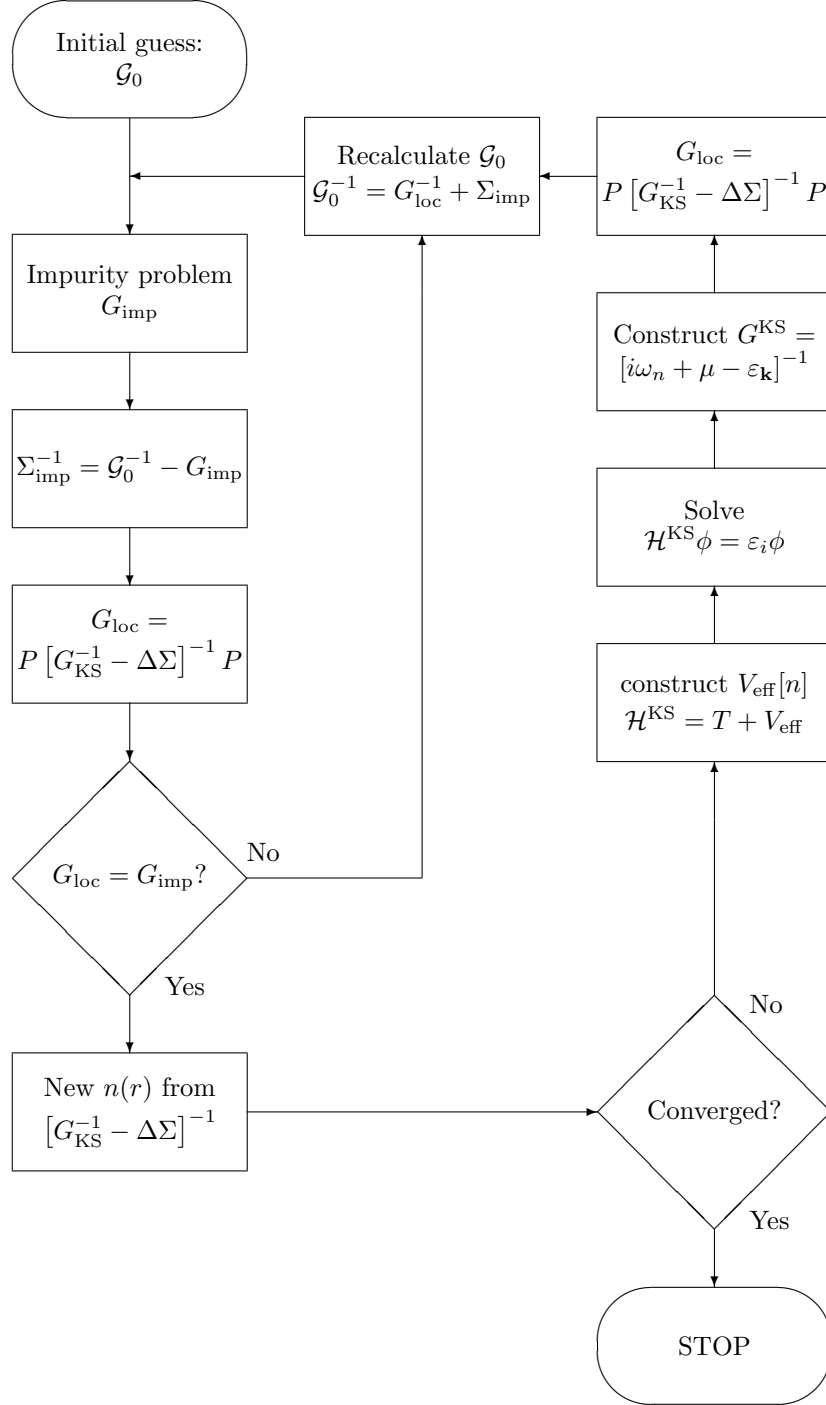


Figure 7.1. Flow scheme illustrating the procedure for solving the LDA+DMFT equations. Two parts are involved, the inner DMFT loop and the outer LDA loop.

7.1.3 Self-consistency cycle

The scheme to solving the DMFT equations is given by the inner loop in Figure 7.1. Starting from an initial guess for the bath: \mathcal{G}_0 , the impurity Green's function, G^{imp} , is then calculated by solving the quantum impurity problem. The impurity self-energy is upfolded according to Equation (7.13), and used to obtain the local Green's function by projection:

$$G_{\text{loc}}(z) = \sum_{\mathbf{k}} P(\mathbf{k}) [i\omega_n + \mu - \varepsilon_{\mathbf{k}} - \Sigma(\mathbf{k}, i\omega_n)]^{-1} P^*(\mathbf{k}) \quad (7.15)$$

Using this result, the bath function is then updated via:

$$\mathcal{G}_{0,\text{new}} = \frac{1}{(G^{\text{loc}})^{-1} + \Sigma_{\text{imp}}} \quad (7.16)$$

This procedure is repeated until self-consistency is reached, ie, when the *impurity* Green's function is equal to the *local* Green's function. When this condition is fulfilled, the dynamical mean field, \mathcal{G}_0 , will also be self-consistent. In the next section it will be outlined how DMFT and DFT can be joined into a self-consistent scheme.

7.2 LDA+DMFT

In the LDA+DMFT framework, the one-electron part of DMFT, ie, interactions between electrons outside \mathcal{C} , are described by DFT. From the full Green's function, charge density can be extracted:

$$n(\mathbf{r}) = \frac{1}{\beta} \sum_n G(\mathbf{r}, \mathbf{r}, i\omega_n) e^{i\omega_n 0^+}, \quad (7.17)$$

where $e^{i\omega_n 0^+}$ ensures the convergence of the Matsubara sum [161]. This charge density can be used to construct an effective potential for the Kohn-Sham Hamiltonian. By solving the Kohn-Sham equations, the electronic structure, $\varepsilon(\mathbf{k})$ is determined, which is used in the procedure of finding the local Green's function, G_{loc} . Then mean-field, \mathcal{G}_0 , is then updated as in Equation (7.16). Figure 7.1 illustrates the self-consistency cycle for electronic structure calculations within LDA+DMFT.

It should be noted that all orbitals are affected by the DMFT treatment of correlations, not just those belonging to \mathcal{C} . The set $|\chi_{\mathbf{R}m}\rangle$, can be constructed from muffin-tin orbitals [162, 136]. Calculations within this thesis were performed using the implementation of the TRIQS package [158], which features an interface with the Wien2k code [163, 164] and a Wannier function basis for $|\chi_{\mathbf{R}m}\rangle$. For the double-counting correction, the so-called “around mean field” (AMF) [107] form has been used for the weakly correlated metals that have been studied.

Chapter 8

Model Hamiltonians for finite temperature simulations

8.1 Statistical simulations of configurations

Within the language of thermodynamics, the relative stability of different phases discussed in Section 1.4, is given by the Gibb's free energy:

$$G = E + pV - TS, \quad (8.1)$$

in terms of (from right to left) internal energy, pressure, volume, temperature, and entropy. The sum:

$$H = E + pV, \quad (8.2)$$

is called the enthalpy. From a statistical physics point of view, S is related to the number of microstates, Ω_r , compatible with the energy E_r , as:

$$S = \beta \log \Omega_r. \quad (8.3)$$

For constant number of particles on a lattice of constant volume, the alloy configuration can be found by minimising the Helmholtz free energy:

$$F = E - TS. \quad (8.4)$$

In order to calculate F from *ab initio* theory, one makes use of the fact that in many systems, the time scale of atomic diffusion in an alloy is typically very long compared to electronic, magnetic, and even vibrational degrees of freedom. At equilibrium, the configurational degree of freedom, ξ , associated with the occupancy of each lattice site, as shown in Figure 1.1, can thus be separated from the faster degrees of freedom [165].

In order to find the equilibrium configuration at a particular temperature, one may then begin by averaging the free energy over the fast degrees of freedom and

thus obtaining a constrained free energy associated with the alloy configuration, F_ξ , which yields the partition function:

$$Z(T, V, N) = \sum_{\xi} \exp[-\beta F_\xi(V, N)]. \quad (8.5)$$

Once Z is determined, the Helmholtz free energy can be obtained as:

$$F(T, V, N) = -\frac{1}{\beta} \ln[Z(T, V, N)]. \quad (8.6)$$

What remains is then a purely configurational problem of evaluating the partition function, Z , which is a formidable task. A practical method is to sample configuration space in Monte-Carlo simulations. However, this still requires the energy of any configuration to be efficiently evaluated.

8.2 The Heisenberg Hamiltonian

In the limit of localised magnetic moments at the lattice sites, that are insensitive to the actual arrangements of surrounding moments, a Hamiltonian for magnetic energy can easily be constructed by an effective classical expression:

$$\mathcal{H} = - \sum_{i \neq j} J_{ij} (\hat{\mathbf{e}}_i \cdot \hat{\mathbf{e}}_j), \quad (8.7)$$

where i and j runs over all sites, and the coefficients J_{ij} are called the pair exchange-parameters. $\hat{\mathbf{e}}_i$ is a unit vector pointing in the direction of the magnetic moment at site i . Following Ref. [166], the physical meaning of the exchange-parameters, J_{ij} , can be thought of as the cost in energy of deviating the magnetic moments at sites i and j by a small angle from each other in an FM environment, as illustrated in Figure 8.1. In the same way, the quantity:

$$J_0 = \sum_{j \neq 0} J_{0j}, \quad (8.8)$$

can be thought of as the cost in energy to deviate a single magnetic moment at site $i = 0$ by a small angle, in a reference system with FM order.

A method to calculate the exchange parameters within the Green's function method, based on the above definitions, was proposed by Liechtenstein et al.[166] This is known as the LKG(M) method, and is based on the Andersen local force theorem [167]. The central equation has the form:

$$J_{ij} = \frac{1}{4\pi} \int^{\epsilon_F} \text{Im Tr} \left\{ \Delta_i \tau_{ij}^\uparrow \Delta_j \tau_{ji}^\downarrow \right\}, \quad (8.9)$$

where

$$\Delta_i = \left(t_i^\uparrow \right)^{-1} - \left(t_i^\downarrow \right)^{-1}. \quad (8.10)$$

In finite temperature calculations, it is highly nontrivial to take into account both transverse and longitudinal fluctuations of magnetic moments in an *ab initio* scheme, although several interesting schemes have been suggested [168, 169].

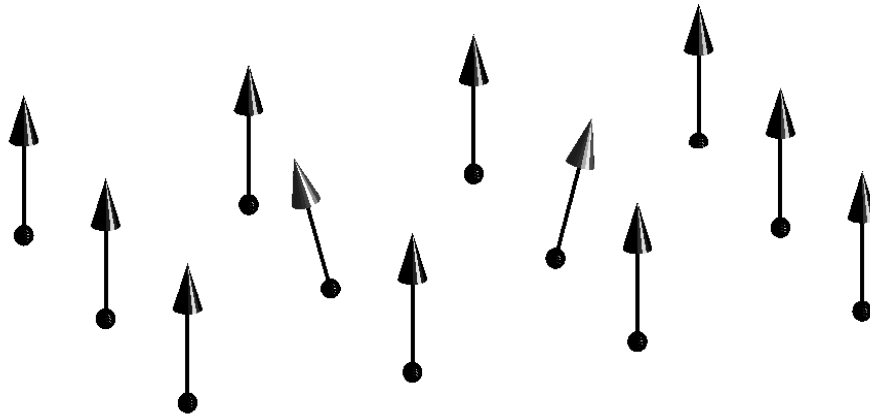
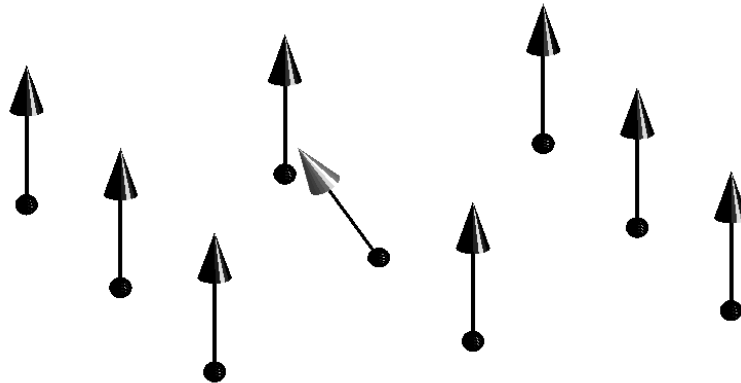
(a) J_{ij} (b) J_0

Figure 8.1. Illustration of the physical meaning of J_{ij} (a) and J_0 (b). In (a) magnetic moments at sites i and j are being deviated from each other. In (b), a single magnetic moment is deviated from the rest of the lattice.

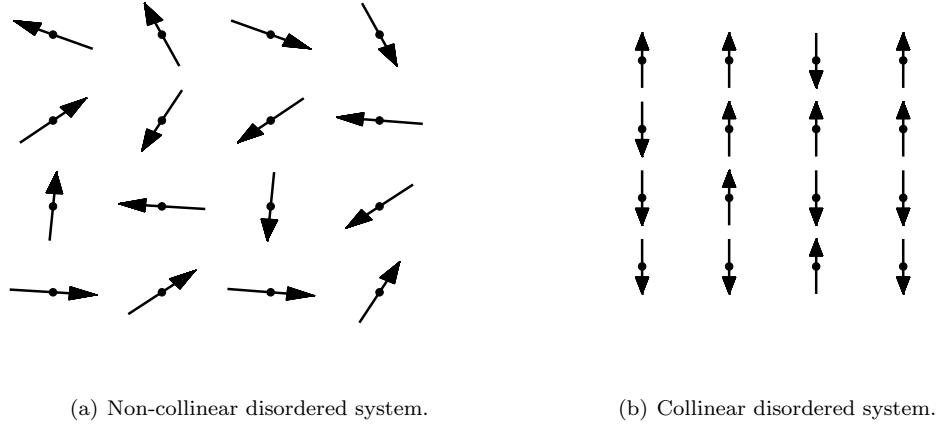


Figure 8.2. Illustration of the principle behind the DLM model. A completely disordered system of non-collinear magnetic moments can be modelled by a completely disordered collinear system.

8.2.1 Disordered Local Moments

As discussed in the previous section, in a Heisenberg system, the local magnetic moments are insensitive to the local environment. It can be shown that a completely disordered system of non-collinear local magnetic moments, can be modelled by a collinear state of disordered up and down local moments [170], as shown in Figure 8.2. This is called the disordered local moment model (DLM) [170], which provides a good representation of the Heisenberg picture of the paramagnetic state, shown in Figure 3.6(b). A magnetic atom, A , is then substituted by a disordered mixture of spin up and spin down atoms:

$$A \rightarrow A_{0.5}^{\uparrow} A_{0.5}^{\downarrow} \quad (8.11)$$

This fictitious alloy is efficiently modelled with the CPA medium.

However, not many systems can be considered Heisenberg systems, and this approximation has its limitations. Ni is more difficult than Fe in *ab initio* calculations because the exchange-interactions are more sensitive to the local environment. The experimentally verified paramagnetic state of Ni actually collapses in DLM, but has been shown to be stabilised by inclusion of longitudinal spin fluctuations [169].

8.3 Cluster expansion of configurational energy

In order for the total energy of the system to be calculated efficiently in each Monte-Carlo cycle it is convenient to expand the configurational part of the total

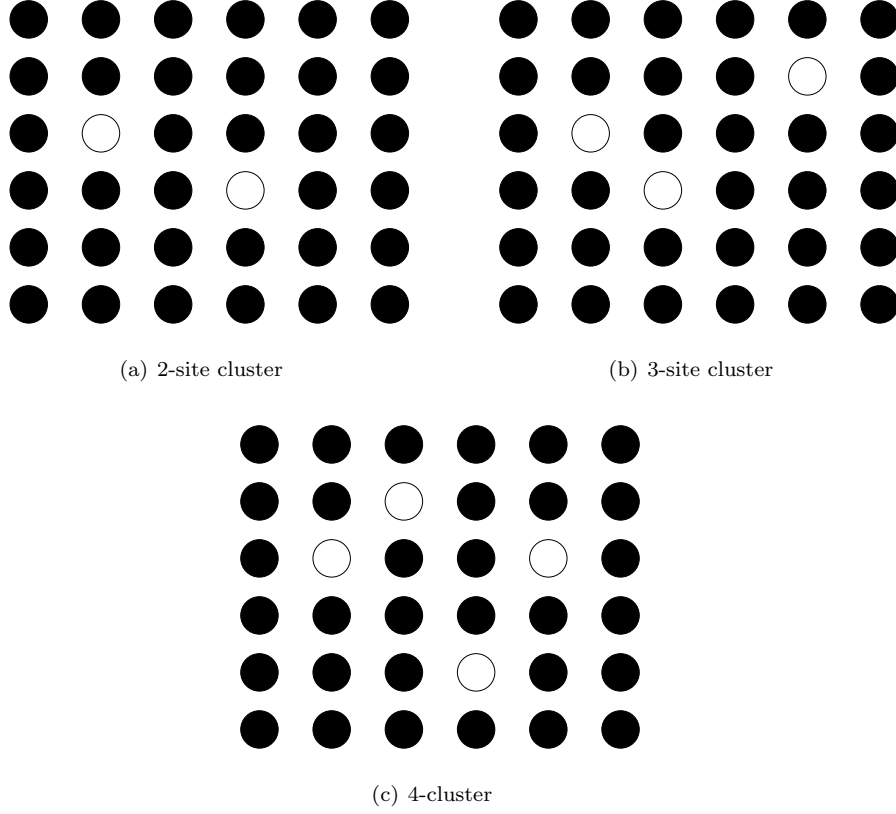


Figure 8.3. Two-dimensional illustration of 2-site, 3-site and 4-site clusters on a lattice.

energy in the basis functions:

$$\Phi_f^{(n)}(\sigma) = \prod_{i \in f} \sigma_i, \quad (8.12)$$

which are defined for each combination of n atoms in the system, called clusters, f , in terms of the spin variables σ_i . In a binary AB -system, $\sigma = \pm 1$, depending on if site i is occupied by an A - or a B -atom. Figure 8.3 illustrates clusters of different orders.

Defining a correlation function, $\xi_f^{(n)}$, for each type of cluster containing n sites as the average:

$$\xi_f^{(n)} = \frac{1}{N_f} \sum_f \Phi_f^{(n)}(\sigma), \quad (8.13)$$

the cluster expansion of total energy can be written:

$$E_r = \sum_f V_f^{(n)} \xi_f^{(n)}. \quad (8.14)$$

The expansion coefficients, V , are called effective cluster interactions (ECI). They can be written in terms of the n -site interatomic potentials as:

$$V_f^{(n)} = \frac{1}{2^n} \sum_{\bar{\sigma}} v_f^{(n)}(\bar{\sigma}) \prod_{i=1}^n \sigma_i \quad (8.15)$$

where a vector $\bar{\sigma} = \{\sigma_1, \sigma_2, \dots, \sigma_n\}$ describes a particular configuration of the n -site cluster, and the sum is taken over all possible occupations. For a fixed global concentration of A -atoms, c , one may use the basis of concentration fluctuation numbers, which are defined for each site in the cluster as:

$$\delta c_i = c_i - c, i \in f \quad (8.16)$$

where c_i is the on-site occupation of A -atoms. The configurational Hamiltonian can then be written on the form:

$$\begin{aligned} \mathcal{H}_{\text{conf}} &= \frac{1}{2} \sum_p V_p^{(2)} \sum_{i,j \in p} \delta c_i \delta c_j \\ &+ \frac{1}{3} \sum_q V_q^{(3)} \sum_{i,j,k \in q} \delta c_i \delta c_j \delta c_k \\ &+ \frac{1}{4} \sum_r V_r^{(4)} \sum_{i,j,k,l \in r} \delta c_i \delta c_j \delta c_k \delta c_l + \dots, \end{aligned} \quad (8.17)$$

where (p, q, r) are indices running over specific types of the clusters denoted as f above, containing 2, 3 and 4 sites, respectively. The ECI are determined from *ab initio* methods within DFT, as described in the following section.

8.3.1 Screened Generalised Perturbation Method

The screened generalised perturbation method (SGPM), proposed by Ruban et al. [171], builds on the older GPM method [172]. As pointed out in the previous section, the ECI are related to the interatomic potentials by Equation (8.15). The potential of the n -site cluster f with configuration σ can in turn be determined by calculating the total energy of the system for the $N - n$ possible configurations in the remaining clusters, and taking the average:

$$v_f^{(n)}(\bar{\sigma}) = \frac{1}{2^{N-n}} \sum_{\bar{\sigma}'} E_f(\bar{\sigma}, \bar{\sigma}'). \quad (8.18)$$

Due to the vast number of terms in the sum, direct calculations become impractical. Averaging only over the configurations $\bar{\sigma}'$ having a particular composition, the ECI become concentration-dependent. However, considering the thermodynamic limit $N \rightarrow \infty$, the averaging can be performed within the CPA, which is a highly efficient approach.

A particular effective cluster interaction can be obtained as the difference in energy between two systems with the same configurations outside the cluster f ,

but with an even and an odd number of A -atoms inside the cluster f , respectively. Using the Andersen force theorem [167], the pair ECI can then be computed as the sum of two terms:

$$V^{(2)} = V_{\text{KS}}^{(2)} + V_{\text{C}}^{(2)} \quad (8.19)$$

The first part is the change in the Kohn-Sham one-electron energy, which may be obtained from the CPA scattering path operators and matrices. For a binary alloy, the expression is:

$$V_{\text{KS}}^{(n)} = -\frac{1}{2^n} \frac{1}{\pi} \text{Im} \int \sum_{\odot \in f}^{E_F} \text{Tr} (\Delta t_i \tilde{\tau}_{ij} \Delta t_j \cdots \Delta t_k \tilde{\tau}_{ki})_f \quad (8.20)$$

where $\Delta t_i = t^A - t^B$ and the sum is taken over the $(n-1)!/2$ paths in the cluster starting and ending on the same site, going through each site only once.

The second term, $V_{\text{C}}^{(n)}$, originates in Coulomb interactions between the atomic spheres, due to the fact that the charges of the atomic spheres are unlikely to equal the nuclear charges, Z , thus carry net charges, q^p . For a binary alloy, the difference in Coulomb potential between the two systems is then given in terms of the charges q^p as:

$$V_{\text{C}}^{(2)} = (q^A - q^B)^2 \frac{\alpha^{(2)}(\mathbf{R})}{2S}, \quad (8.21)$$

where $\alpha^{(2)}(\mathbf{R})$ is called the *intersite* screening constant and describes how efficiently the electrons outside the atomic spheres screen the Coulomb interaction for pairs at distance R . In practice, $\alpha^{(2)}$ is determined from LSGF supercell calculations, where charge transfer effects are handled explicitly in large systems.

The paramagnetic regime

As discussed in Section 1.4, the time scales of magnetic fluctuations and atomic diffusion are very different. On the time scale of atomic diffusion, which is the interesting time scale in phase stability simulations, the magnetic arrangement of the system in the paramagnetic state changes a great number of times. This can be used to one's advantage, by means of averaging out the different magnetic configurations that the system goes through [6]. As discussed in Section 8.2.1, the electronic structure of the Heisenberg paramagnetic state can be modelled by the DLM model in the scalar-relativistic limit. The pair-ECI is then determined for an alloy in the DLM state, which is related to the pair-ECI in the FM state as:

$$V^{\text{DLM}} = V^{\text{FM}} + 2J, \quad (8.22)$$

where J is an exchange-interaction, introduced in Section 8.2.

Part III

Discussion

Chapter 9

Results

In this chapter, a summary is given of the key results in the articles from page 133 and onward. The theoretical descriptions of magnetism introduced in Part I and II are used to study transition metals and their alloys. More specifically, the Fe-Mn, Fe-Ni, and NiMnSb-based alloy systems have been chosen. These systems are not only interesting for their complex magnetic properties, but they are also highly important components in modern technological applications.

FeMn alloys are presently the subject of great interest, due to the development of new advanced high-strength steels with Mn as a key component [173]. Such steels show significantly improved mechanical properties due to the so-called twinning induced plasticity (TWIP) and transition induced plasticity (TRIP) effects during deformation [173, 174]. At a smaller scale, FeMn at the equiatomic composition can be used in spintronic read heads due to its AFM properties [175, 176, 177, 178].

Experimentally, alloy properties can be efficiently screened with a *combinatorial* approach [179] of synthesising a large number of alloys with varying compositions [180]. Parameter-free DFT-calculations can provide a valuable complement to such high-throughput experiments, by revealing insight about magnetism, phase stability and elasticity at a low time cost.

Among the Fe-Ni alloys, one finds the well-known permalloy,¹ or supermalloy, on the Ni-rich side. On the Fe-rich side one finds the very interesting Fe_{0.65}Ni_{0.35} Invar alloy. Permalloy is used as a reliable material for advanced spintronic devices [182], and being a soft magnetic material, it is also used in cores in power and distribution transformers [181]. NiMnSb was the first material to be predicted half-metallic [42], and has since then been a prime candidate for spintronics.

¹ Originally, *Permalloy* was a registered trademark for certain Ni-Fe alloys, but has now become a generic term [181].

9.1 Fe-Mn

Fe-Mn alloys can be found in the fcc-phase with 3–68% Mn content [7]. The magnetic properties of FeMn were long debated in both theory and experiment. Early experiments concluded AFM ordering [183], but were inconclusive about the exact type: and 1Q, 2Q, or 3Q. In particular, close to the equiatomic $\text{Fe}_{0.5}\text{Mn}_{0.5}$ composition has been the subject of numerous studies [184, 185, 186, 187, 188]. Previous theoretical work has been based on LSDA for a fixed lattice, with the experimental lattice spacing. These calculations have yielded varying results depending on the description of the alloy system: ordered structures, CPA or supercells. However, the presently accepted view seems to be that close to the equiatomic composition, the magnetic state is 3Q-AFM, with local relaxations of the magnetic moments from the ideal 3Q directions [189].

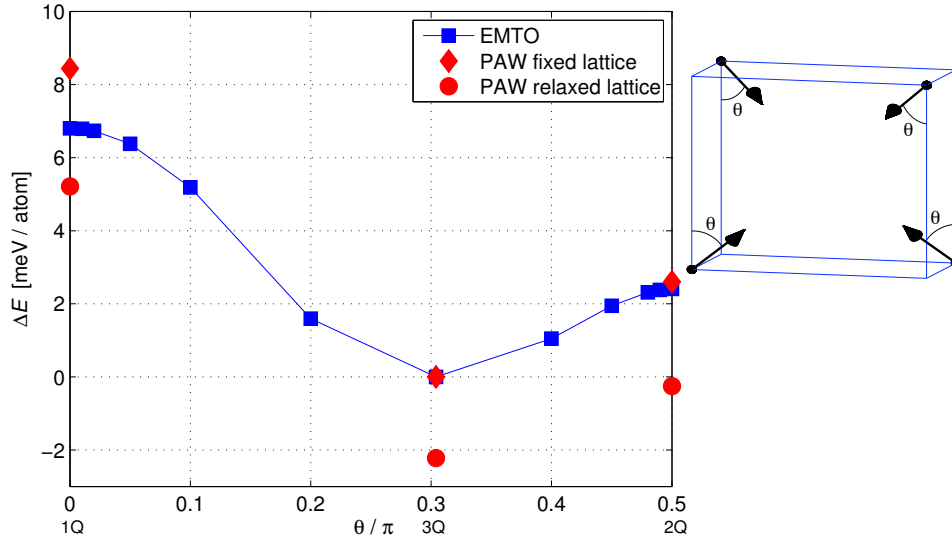


Figure 9.1. Total energy for fcc- $\text{Fe}_{0.5}\text{Mn}_{0.5}$ as a function of the tilt angle θ , at the experimental room-temperature lattice constant of 3.63 Å. Figure taken from Article I. Copyright (2011) by the American Physical Society.

In Article I, local environment effects were included by using SQS-supercells, which allows both the magnetisation and ion positions to be relaxed. Figure 9.1 shows results obtained with LSDA at the experimental room-temperature lattice constant of 3.63 Å. Calculations have been performed with the PAW and EMT0-CPA methods, and is shown as a function of the tilt angle, θ , which is illustrated in Figure 9.1. As θ increases from zero, the magnetic moments are tilted toward a common center in the magnetic unit cell, going from 1Q through the 2Q- and 3Q-configurations. Total energy is seen to be minimised for 3Q, and local environment effects do not to change the qualitative picture. Including local lattice relaxations shifts total energy by approximately 2 meV. Once relaxed, the directions of the

local magnetic moments were found to be distributed around the 3Q-directions, deviating on average 9°.

This minor role of local environment effects motivates the EMTO-CPA method to be used. More complex magnetic states were also considered with this method, such as spin-spiral configurations along the $K-W-X-\Gamma-K-L-\Gamma$ lines. These calculations show that such spiral states are over 50 meV higher in energy than 1Q. Calculations also agree qualitatively with those of Mankovsky et al. [190] along the ΓX -line.

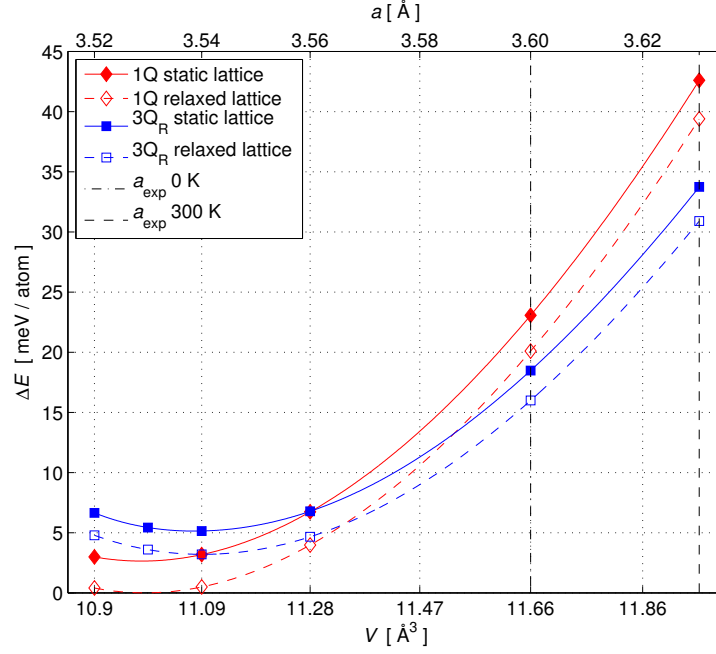
Relaxing the volume with the LSDA functional yields the lattice constant $a_0^{\text{LSDA}} = 3.42 \text{ \AA}$, and magnetic moments in the order of $0.3 \mu_B$. Experimentally, the Fe-Mn alloy is known to show Invar behaviour, with a very small thermal lattice expansion coefficient, below the Néel temperature, which is 450–500 K at this composition [191, 192, 193]. Still, the Invar effect is weaker in this system than for the prototypical $\text{Fe}_{0.65}\text{Ni}_{0.35}$ Invar system. Based on data by Stamm, Kübler extrapolated the 0 K lattice constant to 3.60 \AA [194].

Compared to this value, the LSDA severely underestimates the equilibrium volume. In addition, at a_0^{LSDA} , total energy for the 1Q, 2Q and 3Q states was found to be within approximately 1 meV, with the 1Q state being favoured. These results remind of the case of pure Fe, discussed in Section 5.5.1, where LSDA also underestimates the lattice constant and predicts different magnetic states at experimental and theoretical equilibrium volumes. However, a significant difference is seen in Figure 9.2, which shows energy as a function of the unit cell volume as obtained by the PBE and PW91 GGA-functionals. Although these GGA-functionals improve the volume, giving $a_0^{\text{GGA}} \approx 3.53 \text{ \AA}$, it is still very much underestimated. It is interesting that these GGA parametrisations do not give consistent results concerning the magnetic ground state at the theoretical equilibrium. PBE-GGA results in 1Q, while PW91 slightly favours 3Q for a static lattice. With PW91, local lattice relaxations make 1Q and 3Q degenerate. Such discrepancy between the PBE- and PW91 parametrisations have previously been reported in the literature [195, 196]. The more recent PBEsol-GGA functional slightly improves on LSDA to give $a_0^{\text{sol}} = 3.47 \text{ \AA}$, which is in line with previous observations for magnetic transition metals: PBEsol equilibrium volumes are intermediate between LSDA and PBE-GGA [95].

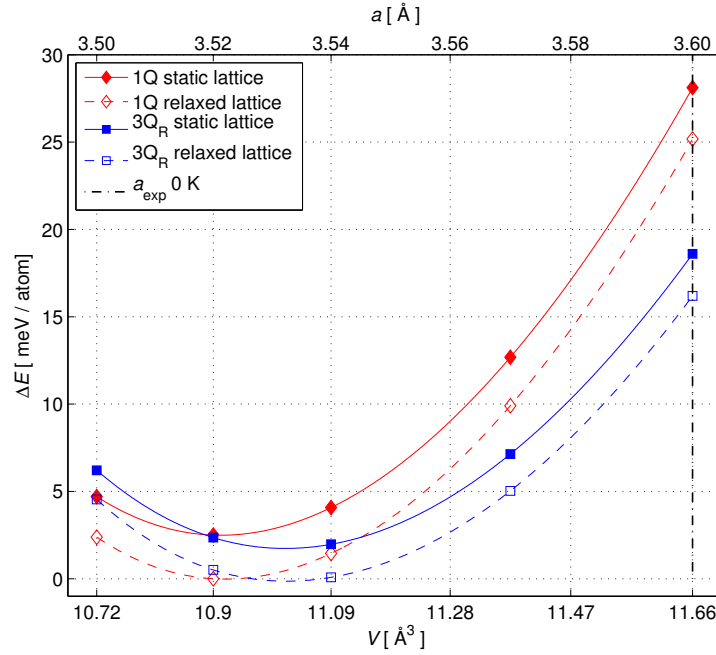
The essential point here is that all exchange-correlation functionals tested give a different magnetic ground state at the theoretical and experimental volumes. Based on these investigations, one may draw the conclusion that the most frequently used exchange-correlation functionals within condensed matter theory do not simultaneously describe equilibrium volumes and magnetic properties at a satisfactory level of accuracy.

9.1.1 Elastic properties FeMn alloys

As shown above, the most widespread non-empirical exchange-correlation functionals do not self-consistently give a satisfactory description of structural and magnetic properties. Due to the great interest in these alloys, reliable computational tools are needed to supplement the combinatorial approach to screen for



(a) PBE



(b) PW91

Figure 9.2. Total energy as a function of volume for fcc-Fe_{0.5}Mn_{0.5} the 1Q (diamonds) and 3Q (squares) magnetic configurations, calculated on a static lattice (filled symbols) and including lattice relaxations (unfilled symbols). The PBE-GGA functional has been used in (a), while the PW91-GGA functional has been used in (b). Figure from Article I. Copyright (2011) by the American Physical Society.

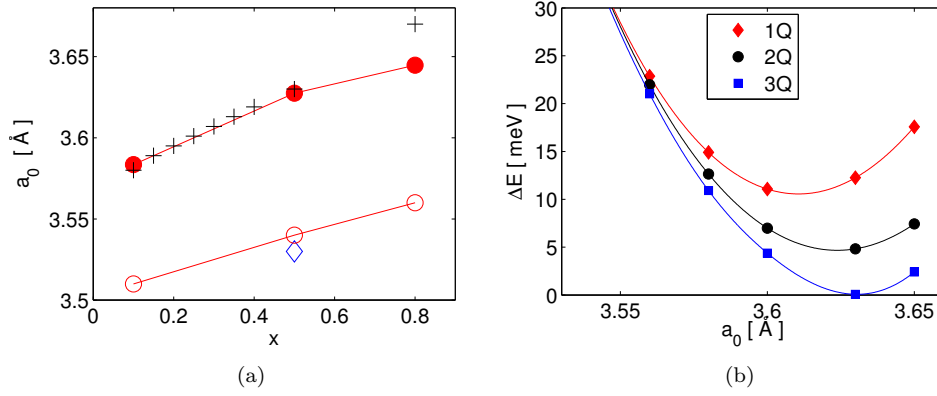


Figure 9.3. Lattice constants (a) and total energy (b) of fcc-FeMn alloys. In (a), lattice constants of $\text{Fe}_{1-x}\text{Mn}_x$ are shown as obtained with different descriptions: EMTO-CPA with frozen-core approximation (filled circles), without frozen core approximation (open circles), and PAW (open diamond). The experimental room-temperature lattice constants are shown by crosses. In (b), total energy is shown for $\text{Fe}_{0.5}\text{Mn}_{0.5}$ as a function of the lattice constant in the 1Q, 2Q, and 3Q configurations, as obtained with EMTO-CPA and the frozen core approximation. corresponds partially to Figure 17(a) in Article I.

alloy properties. In Article I, it was shown that an internally consistent scheme is provided by the EMTO method used in combination with the frozen core approximation. This is a computational approximation, but one which does not need any further adjustable parameters, which can be used for such practical purposes as describe above.

As seen from the results in Figure 9.3, the frozen core approximation corrects the apparent overbinding, restores the experimental volume and therefore also equilibrium magnetic properties. In addition, by using the LSDA functional to calculate the equilibrium charge density and magnetic moments, M_c , and then using this charge density in the GGA-functional, Equation (5.21), also improves magnetic moments. An advantage of the EMTO method is that CPA can be used to for quick scans over composition. As seen above, this is justified since local lattice relaxations have been found to be of minor importance. The same scheme of approximations has been used by other authors for calculating various Fe-based alloys [197].

Bulk modulus

Figure 9.4 shows bulk modulus:

$$B(\Omega) = \Omega \frac{\partial^2 \mathcal{E}(\Omega)}{\partial \Omega^2}, \quad (9.1)$$

evaluated at the ground state volume, Ω_0 , for fcc- $\text{Fe}_{1-x}\text{Mn}_x$ alloys at various compositions, in comparison with measurements reported in Article II. These cal-

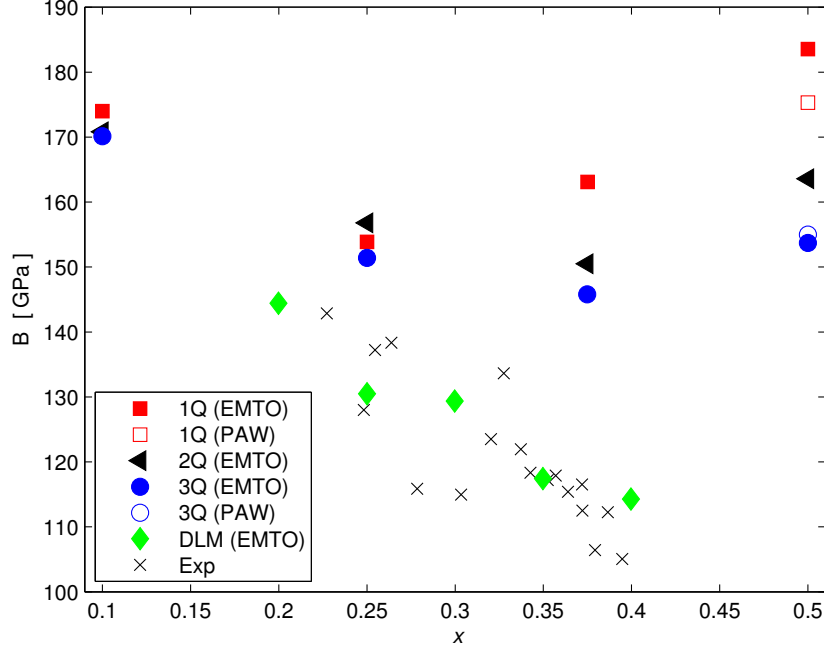


Figure 9.4. Summary of bulk moduli for fcc-Fe_{1-x}Mn_x alloys, calculated with the EMTO-CPA (filled symbols) and PAW-SQS (unfilled symbols) methods. Different magnetic states are assumed: 1Q (squares), 2Q (triangles), 3Q (circles), and DLM (diamonds). Crosses indicate experimental data.

culations have been carried out with EMTO (using the frozen core approximation), and also by PAW supercell calculations. It is seen by comparing the 1Q, 2Q and 3Q values, that in general, non-collinearity as a softening effect on the lattice. Local lattice relaxations lower bulk modulus somewhat for 1Q, but for 3Q they are quite similar, and in fact even shows a slight increase in the figure.

Compared with experiment, the AFM-structures seem to overestimate the bulk modulus. The best agreement is rather obtained by assuming the DLM state, although the measurements are performed below T_N . Since a *practical* scheme is sought in this context, we conclude that this scheme gives a good description of elastic properties at room temperature conditions. This scheme was therefore used in Article V to explore the influence of Al- and Si-additions on elastic properties in FeMn alloys.

fcc-hcp lattice stability

In FeMn alloys, the fcc-hcp relation is of great interest, since the stacking-fault energy of the fcc-phase has been suggested to be directly proportional to the lattice

stability of these phases [198]. Stacking-fault energy is furthermore believed to govern the competing TRIP and TWIP effects [199]. In Article III, the hcp phase was described as magnetically disordered at room temperature using the DLM state. It was found that by assuming an AFM-ordered fcc-phase, there is a cross-over at $\sim 23\%$ Mn content, where the fcc-phase becomes stable with respect to hcp. However, by describing the magnetic state of the fcc-phase by DLM, corresponding to above the Néel temperature, the fcc-phase is destabilised with respect to hcp in the entire considered composition interval, of 15–40%. The effect of small amounts of Al- and Si-additions on these properties was further studied in Article IV.

9.2 Fe-Ni

9.2.1 Influence of the local environment on hyperfine fields

Measurements of the hyperfine field is a powerful method to investigate magnetic properties of alloys at a microscopic level. The hyperfine field has been a test subject of *ab initio* methods for a long time, which started with non-relativistic calculations for the transition metals [200, 201]. LSDA-calculations with this approach for fcc-Ni and fcc-Co agreed within a few per cent with experiment, but for bcc-Fe the calculated field was 23 % lower than the experimental value. As discussed in Section 3.3.3, the hyperfine field is related to the spin polarisation at the nucleus, where relativistic effects can be expected to be significant. Consequently, scalar-relativistic [202] and fully relativistic investigations [203] have been applied to these metals.

In summary, the fully relativistic calculations yielded a significant difference as compared to non-relativistic, or scalar-relativistic studies. However, the agreement with experiment was in fact better with the scalar-relativistic approach, which most likely is due to cancellation of errors [204]. Self-interaction errors have also been investigated by means of the LSDA SIC-functional [77], which only resulted in a minor correction to LSDA results [205, 206]. In alloys, eg, fcc-FeNi, the hyperfine fields have been investigated based on the CPA description [207], and by large clusters embedded into the CPA medium [208, 209]. With the latter approach, it is possible to probe the influence of the local environment on the central atom of the cluster.

In Article VI, the hyperfine field in Fe-Ni alloys was investigated by means of supercell calculations. This allows local environment effects to be studied, since each atom in the cell is in a unique environment. Based on the discussion above, the scalar-relativistic description was adopted, where the field is evaluated as:

$$H_S = C \int m_s(\mathbf{r}) \delta_T(r) d\mathbf{r}, \quad (9.2)$$

in terms of the *s*-electron spin density, m_s , and the radial function:

$$\delta_T(r) = \frac{1}{4\pi r^2} \frac{R_T/2}{((1 + \varepsilon/2c_0^2)r + R_T/2)^2}, \quad (9.3)$$

where ε is the binding energy, and

$$R_T = Z\alpha_0^2, \quad (9.4)$$

in terms of the nuclear charge, Z , and the fine-structure constant, α_0 [202, 204]. The proportionality constant has the value:

$$C = \frac{2}{3} \frac{\mu_0 \mu_B}{a_0^3} \approx 52.4 \text{ T}. \quad (9.5)$$

Equation (9.2) was implemented in the EMTO-based LSGF method, setting $\varepsilon/c_0^2 = 0$, as commonly used [210]. Figure 9.5 shows the hyperfine field obtained

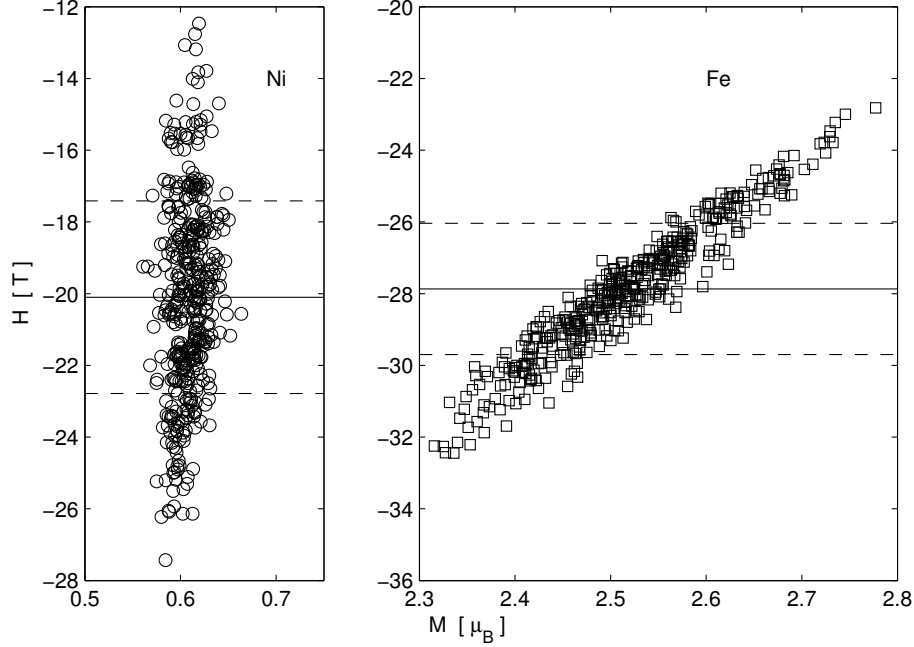


Figure 9.5. Total hyperfine field in $\text{Fe}_{0.5}\text{Ni}_{0.5}$, as obtained in an 864-atom supercell calculation. The fields are shown for the Ni- (circles) and Fe-atoms (squares) as a function of the on-site magnetic moments (top panel) and the average magnetic moments of the nearest and next-nearest neighbour shells. Figure from Article VI.

with the EMT-LSGF method for an SQS supercell consisting of 864 atoms. It should be noted that the field is anti-parallel to local magnetic moment. One can see that for Fe, larger magnetic moments tend to diminish the hyperfine field. For the Ni-atoms, the distribution of magnetic moments is very narrow around the mean value, and the hyperfine fields show a weaker dependence on the local magnetic moment.

Figure 9.6 shows the hyperfine field as a function of the average magnetic moment in the first coordination shell, and as a function of the average magnetic moment in the first two coordination shells. A large (negative) hyperfine field is seen to be connected to a large average magnetic moment in the first coordination shell. Taking instead the average over both the first and second shell, this relation becomes more unclear.

Having seen the dependence of the hyperfine field on the local magnetic moments in the alloy, we next turn to the relation between the s -electron magnetic moment, M_s , and the hyperfine field, which is shown in Figure 9.7. As may be expected, a rather well-defined linear correlation is found. M_s is seen to be anti-parallel to the total onsite moment for all Ni-atoms and for almost all Fe-atoms.

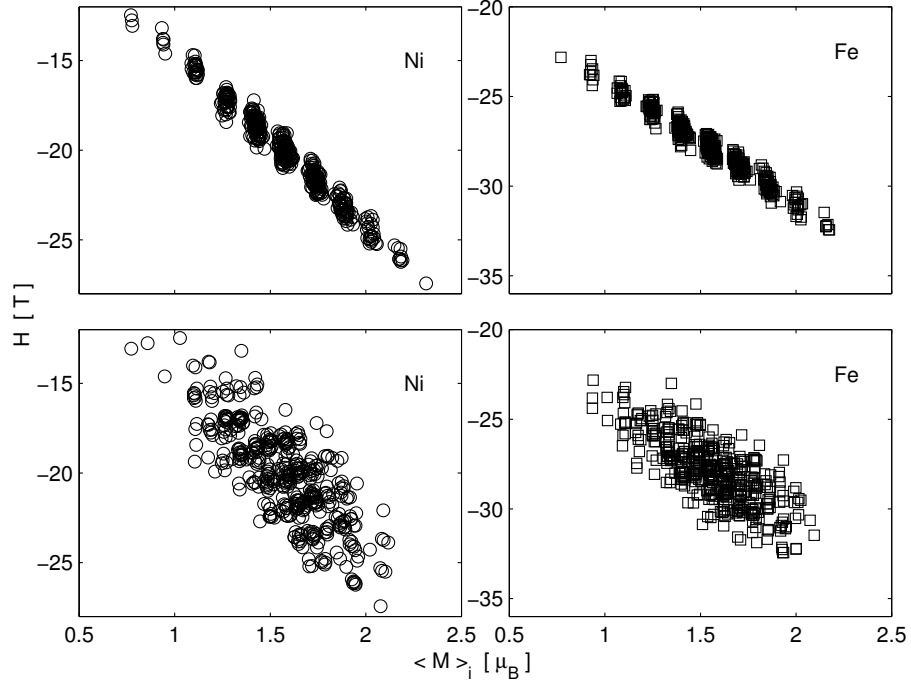


Figure 9.6. Hyperfine field as a function of the average magnetic moment in the first (top panel) coordination shell for Ni- (left) and Fe- (right) atoms in fcc-Fe_{0.5}Ni_{0.5}, as obtained in an 864-atom supercell calculation. Bottom panel shows the field as a function of the average magnetic moment in the first two coordination shells. Figure from Article VI.

Evidently, even for Fe-atoms with $M_s = 0$, there is a local s -electron polarisation giving rise to the hyperfine field. As the polarisation in the Wigner-Seitz cell decreases, so does the contact charge polarisation.

9.2.2 Magnetic excitations and chemical phase stability

The calculation presented in Article VII for Fe-Cr-Ni shows that a description of the paramagnetic state beyond the simple Stoner model is needed. For this system, a non-magnetic description of the paramagnetic state erroneously predicts a dramatic increase in bulk modulus above the Curie temperature. If the paramagnetic state is instead described by the DLM model, featuring finite local moments, the obtained bulk modulus agrees very well with experiment.

For chemical ordering in the paramagnetic state, the difference between results based on these descriptions have shown equally dramatic differences [211]. An even more complicated case is below the Curie or Néel temperature, where the magnetic state is neither paramagnetic nor completely ordered. A prime example of such a system is the Ni-rich Fe-Ni alloy. As seen in Figure 1.2, close to

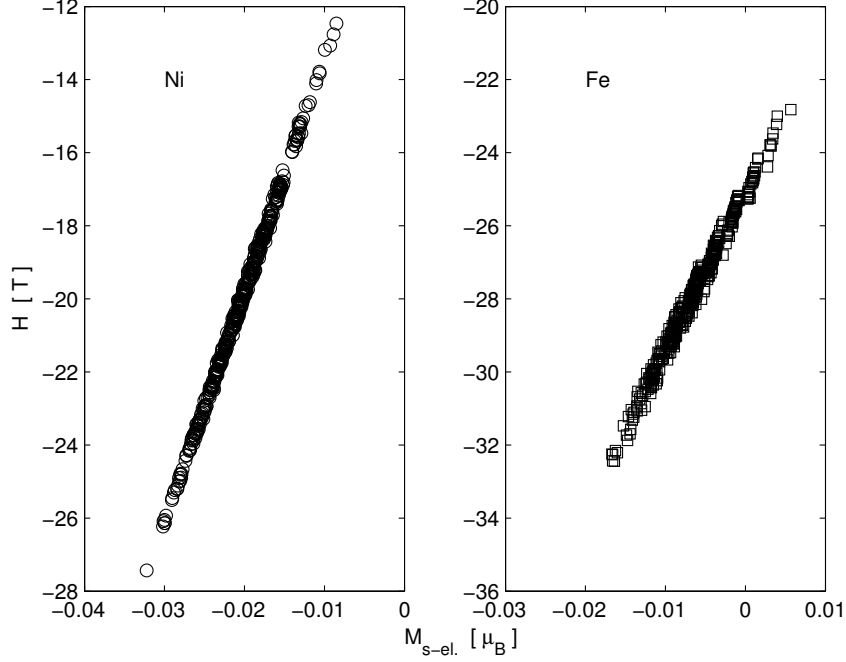


Figure 9.7. Hyperfine field as a function of the on-site s -electron magnetic moment for Ni- (left) and- Fe (right) atoms in fcc-Fe_{0.5}Ni_{0.5}, as obtained in an 864-atom supercell calculation. Figure from Article VI.

the permalloy composition, the Curie temperature, T_C , is just 100 K above the chemical order-disorder transition temperature, T_K . This alloys is thus the perfect model system to develop schemes to study the complex interplay between magnetic and chemical degrees of freedom, as well as developing methods to handle these effects in practical phase stability simulations.

In Article VIII, the Fe_{1-c}Ni_c alloy was modelled as a three-component alloy:

$$\left(\text{Fe}_{\frac{1-m}{2}}^{\uparrow} \text{Fe}_{\frac{1+m}{2}}^{\downarrow} \right)_{1-c} \text{Ni}_c. \quad (9.6)$$

The parameter m determines the degree of global magnetisation, where $m = 1$ corresponds to a completely ordered FM state, and $m = 0$ corresponds to the DLM state. This partial DLM state was previously used in Ref. [165] for Fe-Cr.

With this description of the underlying magnetic state, the ECI were determined by the SGPM method, which allows a configurational Monte-Carlo simulation to be carried out. Figure 9.8(a) shows the obtained transition temperature as a function of composition, c , for various underlying magnetic states, in comparison with experiment. Assuming a completely ordered FM state, the transition temperature is significantly overestimated. On the other extreme, assuming a DLM state

in this regime results in a very underestimated transition temperature. The difference in final transition temperature between these descriptions is approximately 500 K, and in addition, the shape of the phase boundary is not well described either one. Thus, it is clearly seen that neither FM- nor DLM-states provide an adequate description in this temperature regime.

However, it is seen in the figure that the phase boundary is quite well described as a state with global magnetisation $0.6 < m < 0.7$. This degree of global magnetisation corresponds to the experimentally reported reduced magnetisation at T_K . In order to predict the transition temperature self-consistently, the degree of global magnetisation needs to be calculated at T_K . A scheme to self-consistently determine the degree of global magnetisation at T_K can be obtained by simulating the magnetisation, m , in a Heisenberg Monte-Carlo simulation, as discussed in Article VIII. This value of m can then be used as an input to recalculate the ECI, and obtain a new order-disorder transition temperature in a configurational simulation. Figure 9.9 illustrates this procedure.

Our Heisenberg Monte-Carlo simulations yield a Curie temperature in good agreement with experiment, as shown in Figure 9.8(b) for the $\text{Fe}_{0.25}\text{Ni}_{0.75}$ composition. These calculations also predict the magnetisation $m(T_K) \approx 0.61$, and $T_K = 747$ K, which is in agreement with experimental data. It should be noted that this scheme has been demonstrated for a moderately itinerant electron system, and can thus be expected to perform well also in a “good” Heisenberg system.

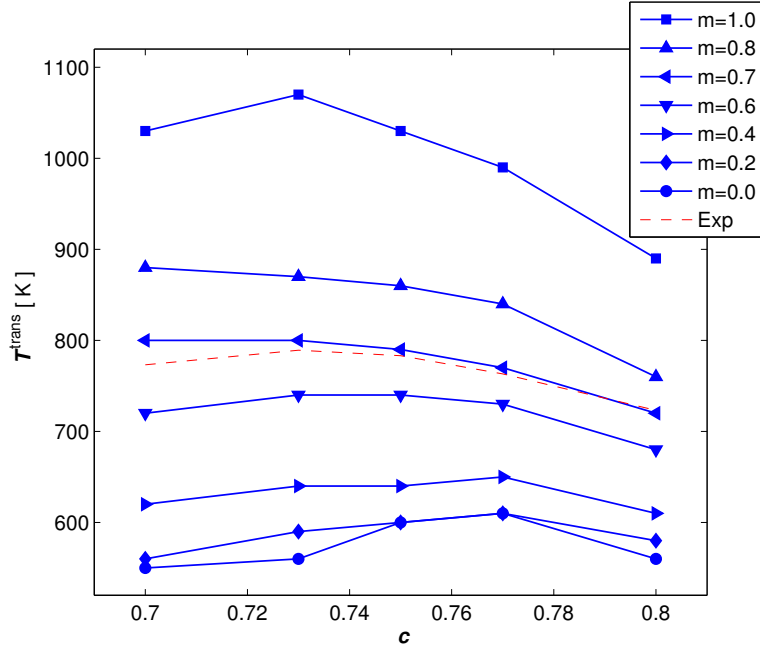
9.2.3 High pressure

At the pressure of about 13 GPa, pure Fe transforms from bcc to the hcp-based ϵ -phase [212]. The magnetic state of the hcp-phase is not entirely clear. Early experiments concluded a Stoner-type non-magnetic state [213], while theoretical work subsequently explained measurements, such as the equation of state, by various AFM- or spiral-configurations [59, 214, 215, 216]. However, the Néel temperature for such states has been estimated to be as low as 69 K at the transition pressure, and decreasing further at higher pressure [217].

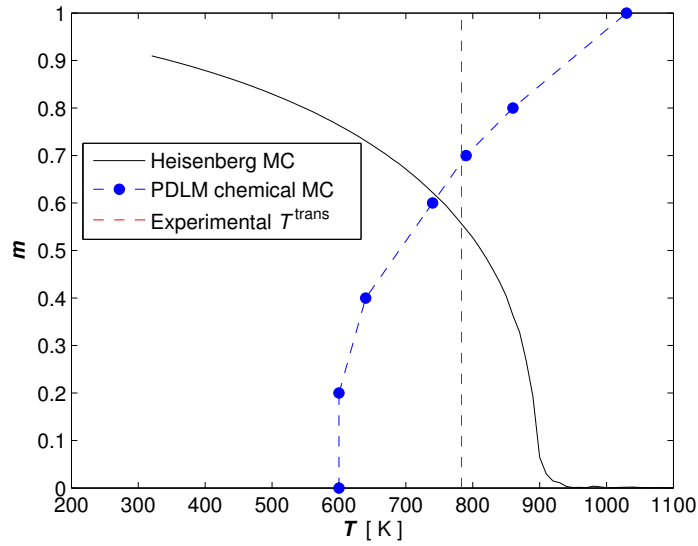
Figure 9.10 shows measured Mössbauer central shift in Fe as a function of pressure, reported in Article IX. As seen in the figure, the reconfiguration of atomic environment associated with the bcc-hcp transition shows up as a jump in the central shift. However, one can also see an anomaly in the central shift around 65 a.u.³. To investigate this anomaly, the isomer shift was calculated as a function of pressure in Article IX. As seen in Equation (3.6), the central shift is composed of two parts: the isomer shift and the relativistic second-order Doppler shift. Changes in the isomer shift as a sample is subjected to external pressure is easily calculated within the scalar-relativistic approximation, since changes in the measured isomer shift can be related to changes in the contact charge density:

$$\delta^{\text{IS}} = \alpha [|\rho_a(0)|^2 - |\rho_s(0)|^2] \quad (9.7)$$

where $\rho_i(0)$ is the contact charge density in the source and absorber [50]. α is an empirical calibration constant.



(a)



(b)

Figure 9.8. (a) shows results for the order-disorder transition temperature in Fe_{1-c}Ni_c alloys for various degrees of global magnetisation m . (b) shows a graphical solution to the self-consistency procedure for m and transition temperature for Fe_{0.25}Ni_{0.75}. Experimental values from the phase diagram in Figure 1.2 are shown by the dashed lines. Figures from Article VIII. Copyright (2010) by the American Physical Society.

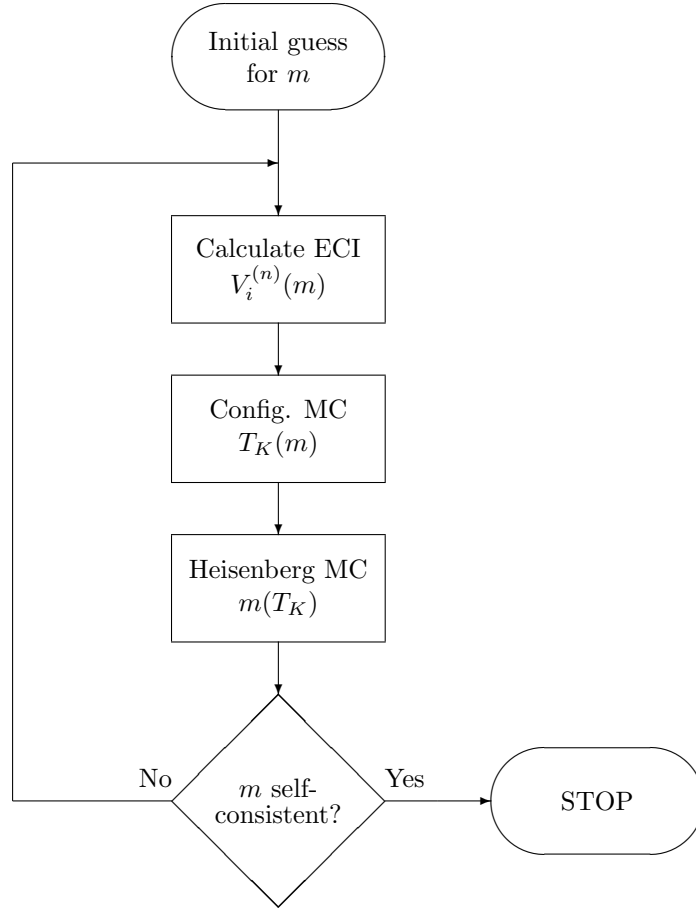


Figure 9.9. Flow chart showing the self-consistency procedure in Article VIII to find degree of global magnetisation, m , and chemical order-disorder temperature, T_K .

To calculate δ^{IS} from *ab initio* calculations, contact charge calculations were implemented in the framework of the EMTO method. The so-called finite nucleus model [218] was adopted, in which the nuclear charge is assumed to be distributed uniformly in a sphere of radius R_n :

$$\rho_{\text{nuc}}(r) = \begin{cases} \rho_0 & r \leq R_n \\ 0 & r > R_n \end{cases} \quad (9.8)$$

where the radius for a nucleus of mass number A is taken from the empirical relation:

$$R_n = D \cdot A^{1/3}, \quad (9.9)$$

with $D = 1.20\text{--}1.30 \cdot 10^{-5}$ a.u. [219]. The contact charge can then be evaluated as the mean of the radial charge density inside the finite nucleus:

$$\langle \rho \rangle = \frac{4\pi}{V_n} \int_{R_0}^{R_n} n(r) r^2 dr. \quad (9.10)$$

Here, $V_n = 4\pi R_n^3/3$, and R_0 is the first point on the radial grid.

Using Equation (9.10), the change in the contact charge as a function of unit cell volume was then calculated. The calibration constant, α , was assigned the value $|\alpha| = 0.27$ mm/s, to simultaneously describe the volume dependence of the isomer shift in the α -phase, and the low-volume behaviour in the ϵ -phase. To describe the paramagnetic hcp-phase, several calculations were performed assuming both the Stoner paramagnetic state and the Heisenberg state of disordered local moments. The magnitude of these moments was fixed to various different values, as well as self-consistent values obtained with the method in Ref. [169], including longitudinal spin fluctuations. In order to include the effect of correlations for the 3d-electrons at a level beyond LSDA, calculations were also performed using LDA+DMFT.

It is seen in Figure 9.10 that none of these calculations reproduce the anomaly. However, as further discussed in Article IX, calculations of the Fermi surface, ϵ_F based on LDA+DMFT indicate an electronic topological transition at the pressure of the observed anomaly. Experimental measurements of sound velocity and the c/a -ratio also indicate a peculiarity in this region. Such anomalies have previously been discussed to be associated with electronic topological transitions in other materials [20]. These results suggest that the anomaly in the central shift is not related to the isomer shift, but rather the second-order Doppler shift in Equation (3.6), due to a pressure induced electronic topological transition, which affects the phonon spectrum. The failure of LSDA to reproduce the transition is an interesting indication of correlation effects actually becoming more pronounced at elevated pressure.

Paramagnetic states

At ultra-high pressure, such as that of the Earth core, one may expect the Stoner criterion to be violated for Fe, resulting in a Stoner paramagnetic state, as discussed in 3.5. At this pressure, the bcc-, fcc-, and hcp-phases have been suggested

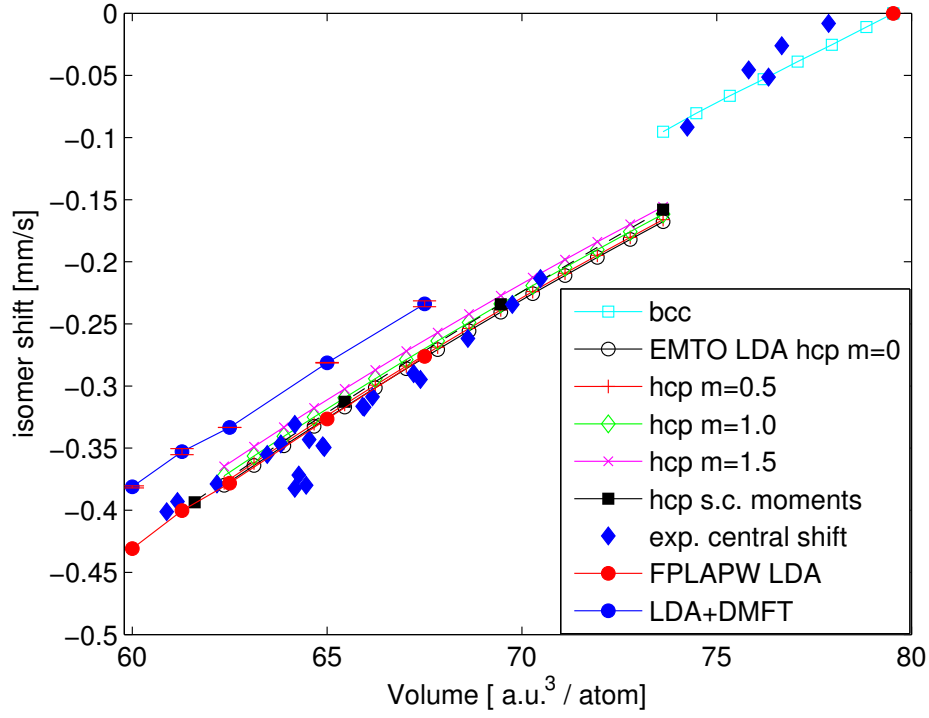


Figure 9.10. Measured Mössbauer isomer shifts (free-standing diamonds) compared to calculated central shifts in Fe. Calculations are shown for bcc (open squares) and hcp structure at low volume. The hcp-phase has been calculated using LDA with the EMT0 method for non-magnetic and paramagnetic phases. In the paramagnetic phase, local moments have been fixed to 0.5, 1.0 and 1.5 μ_B . Additionally, local moments calculated self-consistently as a function of volume have been used (filled squares). Calculations done with the full-potential LAPW method are also shown (filled grey circles). In the hcp-phase, LDA+DMFT calculations are shown by black filled circles with errorbars. The experimental data for the central shift shows an anomalous drop at 65 a.u.³, which is not reproduced by any calculations of the isomer shift.

as candidate crystal structures of the Earth inner core [220, 221]. Recent calculations based on LDA+DMFT have probed the magnetic susceptibility as a function of temperature at ultra-high pressure [222]. These calculations reported a Stoner-type paramagnetic state of the fcc- and hcp-phases, while a Curie-Weiss behaviour of the magnetic moments was found in the bcc-phase at 5000 K.

The Earth core is believed to be composed of Fe, with a 10–15% concentration of Ni. In modelling FeNi-alloys, it should also be pointed out that the fcc–hcp energy difference is on the same scale as the *chemical* ordering energy of the fcc-phase, which is found in ordered structures at ambient conditions. This was pointed out in Article X, where it was also found that the addition of Ni has a different impact on the hcp–fcc phase relation depending on temperature. Calculations up to 4000 K indicated the fcc-phase to become more stable with increasing Ni content up to 20 %. At 6600 K, additions of Ni were instead seen to favour the hcp-phase.

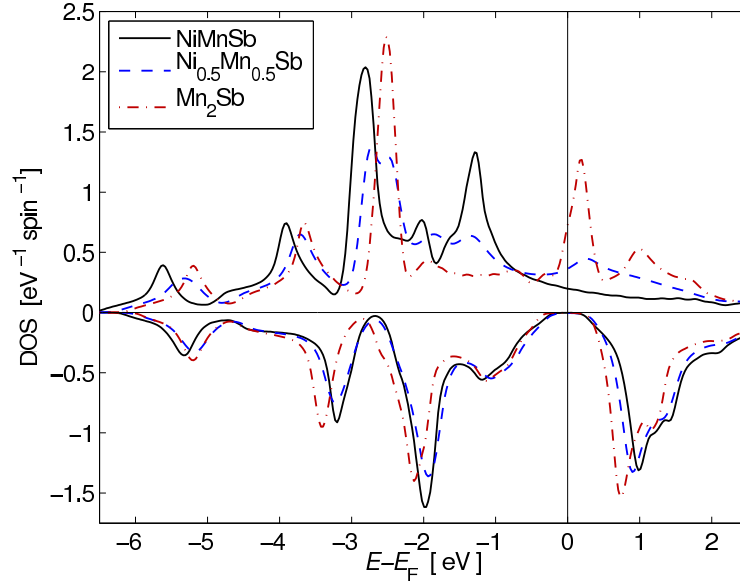


Figure 9.11. Spin-resolved density of electron states for $\text{Ni}_{1-x}\text{Mn}_{1+x}\text{Sb}$. The gap in the minority spin channel around E_F is clearly seen at all compositions. Reprinted with permission from Article XII. Copyright 2010, American Institute of Physics.

9.3 NiMnSb

In combination with Sb, Ni and Mn can be stabilised in the half-Heusler crystal structure shown in Figure 3.3. The ordered NiMnSb-compound was the first material to be predicted as a half-metallic ferromagnet, as discussed in Section 3.3.2. However, half-metallicity at room temperature has not been achieved.

Figure 9.11 shows the half-metallic density of states, with a band gap in the minority spin channel. The magnetic moments are shown in Figure 9.12(a) and are seen to be largest for the Mn atoms. Ni carries only a small magnetic moment. The total magnetic moment is $4.0 \mu_B$ / unit cell, as required for a half-metallic system. The magnetic exchange interactions, shown in Figure 9.13(a) are also seen to be dominated by Mn-Mn interactions, with only a small Ni-Mn interaction. Ni-Ni coupling is vanishingly small.

It has been suggested that the reason for the apparent loss of half-metallicity at $T^* \approx 70\text{--}100$ K is spin-wave excitations, which would induce states in the band gap. From this perspective it is interesting to study how the magnetic exchange-interactions are affected if the Ni-atom is replaced with another 3d-atom, X , so that the composition is altered to:

$$(\text{Ni}_{1-c}\text{X}_c)\text{MnSb}, \quad (9.11)$$

while constraining the crystal structure to C1_b . Replacing Ni with a more magnetically robust atom could be used to manipulate the spin-wave spectrum and increase the transition temperature, T^* . Such doping was considered in Article XI

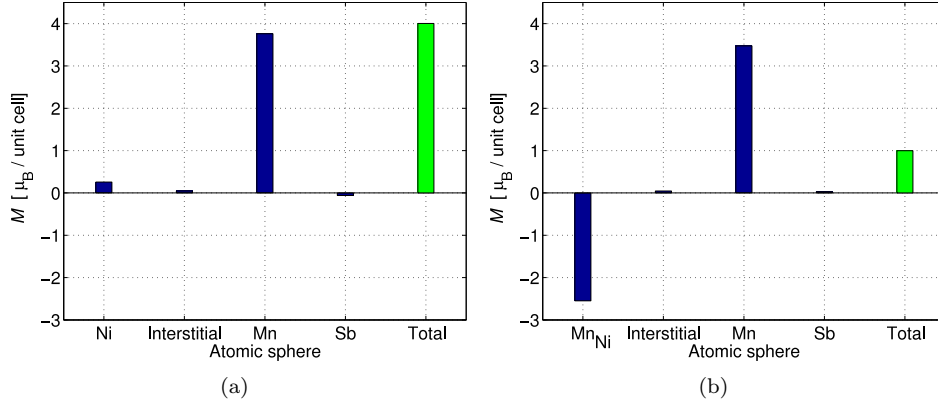


Figure 9.12. Magnetic moments in C1b-NiMnSb and C1b-Mn2Sb. Reprinted with permission from Article XII. Copyright 2010, American Institute of Physics.

for $c = 0.05$, where all magnetic atoms in the 3d-series were tested. Out of all 3d-metal dopants on the Ni sublattice, Cr and Mn show a very strong magnetic exchange coupling to the rest of the lattice. In particular, Mn as a replacement for Ni does not destroy half-metallicity at any composition, as shown in Figure 9.11, It is seen that even the end compound, C1_b-Mn₂Sb, is half-metallic, which is in agreement with previous theoretical reports [40].

Figure 9.13(b) shows the exchange-couplings for the alloy C1_b-Ni_{0.75}Mn_{1.25}Sb. We see that Mn-atoms sitting on the Ni-sublattice (A) becomes AFM-coupled to Mn on sublattice B. Replacing the Ni atom with Mn removes 3 majority electrons from the unit cell, so that the magnetic moment of Mn-B is $-3 \mu_B$. Mn-A is virtually unaffected, and as the concentration of Mn-atoms is increased, the total magnetisation actually decreases linearly with composition from $4 \mu_B$ to $1 \mu_B$. Since it seems possible to replace the weak link in this magnetic system without destroying half-metallicity, it is interesting to investigate if this alloy system can be stable at room temperature.

9.3.1 Stability of (Ni,Mn)MnSb-alloys

The stability of the C1_b-Ni_{1-x}Mn_{1+x}Sb system with respect to the crystal structure was investigated in Article XII both theoretically and experimentally. The Gibb's free energy, Equation (8.1), was calculated within the half-Heusler structure, as well as the C38 structure, which is the ground state structure of Mn₂Sb, which is an ordinary metal [223]. These results are shown in Figure 9.14, which also shows the Gibb's common tangent construction at room temperature. According to this data, the room-temperature solubility is 32 %.

Ni, Mn and Sb was then deposited by means of direct-current (DC) magnetron sputtering on MgO(100) substrates. By using three sputtering targets: NiMn,

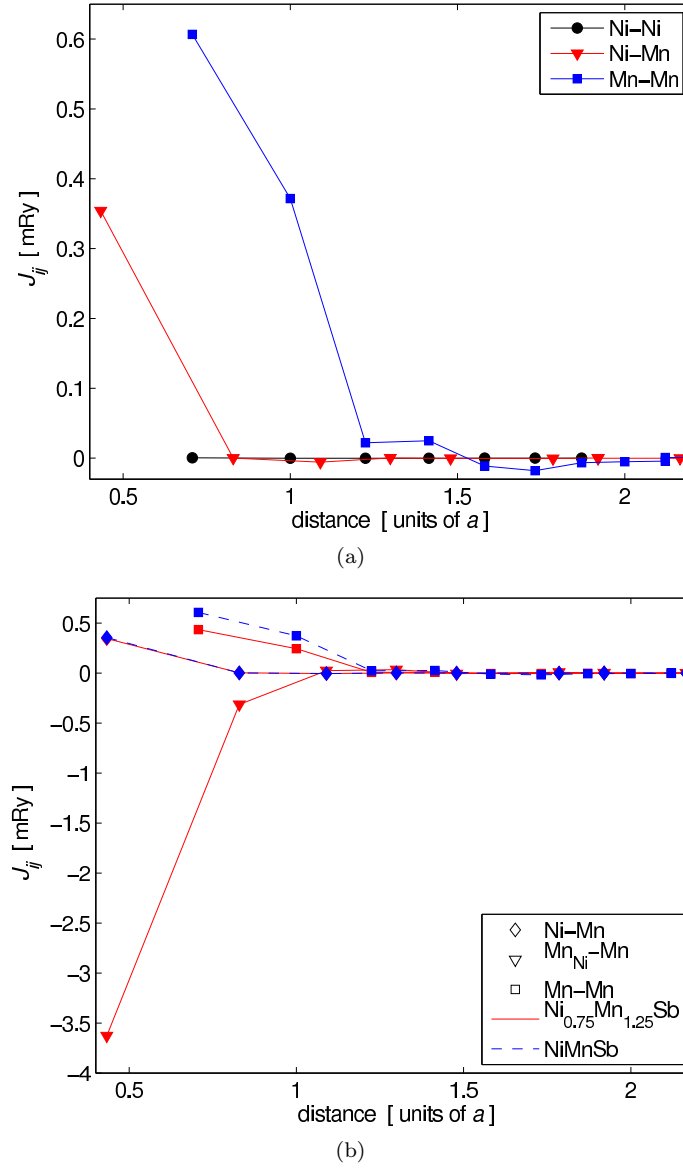


Figure 9.13. Exchange interactions in (a) NiMnSb and (b) $\text{Ni}_{0.75}\text{Mn}_{1.25}\text{Sb}$. Reprinted with permission from Article XII. Copyright 2010, American Institute of Physics.

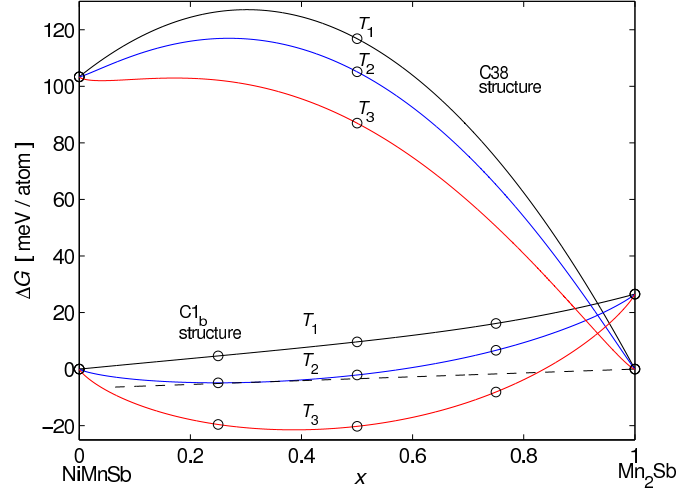


Figure 9.14. From Article XII. Calculated Gibb's free energy in the $\text{Ni}_{1-x}\text{Mn}_{1+x}\text{Sb}$ alloy at various temperatures, within two different crystal structures, the half-Heusler C1_b structure and the tetragonal C38 structure of Mn_2Sb . The Gibb's common tangent construction is also shown for the room temperature curves. Reprinted with permission from Article XII. Copyright 2010, American Institute of Physics.

MnSb and Mn , the combination can yield any composition of $\text{Ni}_{1-x}\text{Mn}_{1+x}\text{Sb}$:

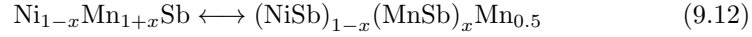


Figure 9.15 illustrates the confocal arrangement of the magnetrons in the vacuum chamber.

By placing the MgO substrates on different positions on the substrate table, different compositions can be obtained in the same run. The compositions were measured by means of energy-dispersive x-ray spectroscopy (EDX), which indicated that $x = 0.05$ and $x = 0.19$ could be achieved. Figure 9.16 shows X-ray diffraction performed with grazing incidence (GIXRD) for the films with $\text{Ni}_{0.95}\text{Mn}_{1.05}\text{Sb}$ - and $\text{Ni}_{0.81}\text{Mn}_{1.19}\text{Sb}$ -composition. Both diffraction patterns clearly show peaks belonging to the NiMnSb -structure. Also, no signs of any peaks belonging to the competing C38 structure could be observed. These measurement confirm the theoretical predictions of a stable half-Heusler $(\text{NiMn})\text{MnSb}$ alloy at room temperature.

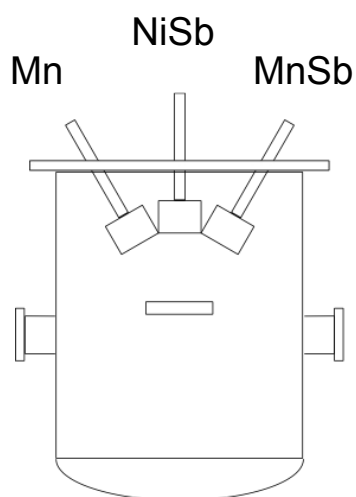


Figure 9.15. Illustration of the confocal arrangement of magnetrons in the vacuum chamber above the substrate table. Artwork by P. Larsson.

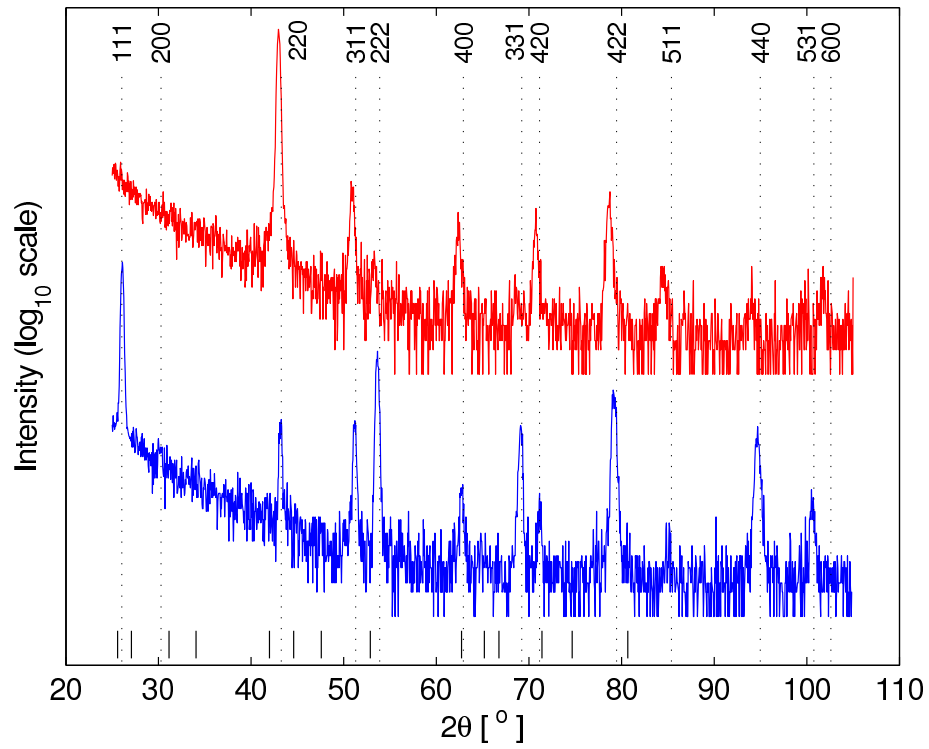


Figure 9.16. X-ray diffraction patterns for $\text{Ni}_{0.95}\text{Mn}_{1.05}\text{Sb}$ - and $\text{Ni}_{0.81}\text{Mn}_{1.19}\text{Sb}$ -films (bottom and top curves, respectively). The dashed vertical lines and Miller indices indicate tabulated diffraction peaks for the ideal NiMnSb half-Heusler structure. The marks above the x-axis indicate tabulated diffraction peaks for the competing C38 structure. Reprinted with permission from Article XII. Copyright 2010, American Institute of Physics.

Chapter 10

Conclusions and outlook

Within this thesis, we have seen examples of how the interplay between magnetic degrees of freedom and the structural and chemical properties of transition metal alloys reveal themselves. The effect of the local environment has been shown to be of paramount importance in transition metals in a wide range of problems, such as the magnetic environment for hyperfine magnetic fields, or the chemical ordering for structural stability at Earth core conditions. The work concerning half-metals also suggests how the magnetic interactions can be modified in NiMnSb by changing the composition to obtain the demonstrated stable (NiMn)MnSb alloy system.

It has also been shown how standard DFT descriptions, in terms of local and semi-local exchange-correlation functionals, are challenged by these materials. Transition metals are thus very complex magnetic systems, where even different GGA-functionals may give internally inconsistent results. In particular, the high-pressure phase of Fe was also found to show qualitatively new features when going beyond the one-electron description.

As an outlook for further research regarding the theoretical description of transition metal magnetism, two particularly interesting themes can be identified throughout this thesis: electron correlations and magnetic excitations. The results point out the importance of further developing descriptions of exchange- and correlation-effects, as well as other methods for treating Coulomb interactions, such as LDA+DMFT.

Finite temperature magnetism of these systems, especially at high pressure, is also a highly important aspect. The demonstrated interplay with chemical interactions emphasises the need for the simultaneous description of these degrees of freedom, as exemplified by the scheme suggested for FeNi permalloy. This is important not only for a fundamental understanding, but also for the future development of transition metal alloys in advanced functional materials.

Appendix A

Units

Unless specified, Hartree atomic units (a.u.) [224] have been used for equations. In this system, the electron mass, charge, reduced Planck constant, and the Bohr radius for atomic hydrogen are assigned the value:

$$m_e = e = \hbar = a_0 = 1. \quad (\text{A.1})$$

The Bohr magneton then takes the value:

$$\mu_B = \frac{e\hbar}{2m_e} = \frac{1}{2}. \quad (\text{A.2})$$

The fine structure constant:

$$\alpha_0 \approx 1/137.036, \quad (\text{A.3})$$

gives the speed of light as:

$$c_0 = \frac{1}{\alpha_0}, \quad (\text{A.4})$$

which in turn gives the value of the permeability of free space:

$$\mu_0 = \frac{4\pi}{c_0^2} = 4\pi\alpha_0^2. \quad (\text{A.5})$$

The atomic energy unit is sometimes called Hartree (Ha), and is related to more well known units as:

$$1 \text{ Ry} = 0.5 \text{ Ha} = 13.605698 \text{ eV} = 2.1799 \cdot 10^{-18} \text{ J}. \quad (\text{A.6})$$

The atomic length unit is:

$$1 \text{ a.u.} = 0.529177 \text{ \AA} = 0.529177 \cdot 10^{-10} \text{ m}. \quad (\text{A.7})$$

In addition, the Planck unit has been used for the Boltzmann constant, in which:

$$k_B = 1. \quad (\text{A.8})$$

Appendix B

Computational details of unpublished calculations

B.1 Charge density and DOS

Radial charge density (Fig. 2.1) and DOS (Fig. 3.2) were calculated at the experimental lattice constant using the LSDA exchange-correlation functional, with the PZ-parametrisation. The Wigner-Seitz radius was set to 2.65 a.u. for bcc-Fe, 2.60 for fcc-Ni, 2.67 for fcc-Cu, and 2.7574 for $\text{C1}_b\text{-NiMnSb}$. The EMTO-FCD code was used, including s, p, d, f muffin-tin orbitals. The \mathbf{k} -points were chosen from a grid of $33 \times 33 \times 33$ points, using then using the Monkhort-Pack scheme. DOS was evaluated with the setting:

`IMAGZ = 0.002 - 0.005` .

The gradients and energy densities in Figure 5.4 were calculated with the same method.

B.2 Comparing LSDA and PBE for Fe

Calculations presented in Figure 5.3 were performed with the PAW method (VASP) using:

`ENCUT = 370`

and using the Monkhorst-Pack scheme to choose \mathbf{k} -points from a $35 \times 35 \times 35$ grid. $3p$ -states were treated as core-states.

Appendix C

Spin matrices

Rotation matrix

The spin-1/2 rotation matrix is [85]:

$$U(\theta, \varphi) = \begin{pmatrix} \cos(\theta/2)e^{i\varphi/2} & \sin(\theta/2)e^{-i\varphi/2} \\ -\sin(\theta/2)e^{i\varphi/2} & \cos(\theta/2)e^{-i\varphi/2} \end{pmatrix}, \quad (\text{C.1})$$

in terms of the angles θ and φ described in Figure 3.5.

Pauli spin matrices

The density matrix can be expressed with the magnetisation density as:

$$\mathbf{n}(\mathbf{r}) = \frac{1}{2} \begin{pmatrix} n(\mathbf{r}) + m_z(\mathbf{r}) & m_x(\mathbf{r}) - im_y(\mathbf{r}) \\ m_x(\mathbf{r}) + im_y(\mathbf{r}) & n(\mathbf{r}) - m_z(\mathbf{r}) \end{pmatrix}, \quad (\text{C.2})$$

where the components of the magnetisation can be recovered using the Pauli spin matrices:

$$\sigma_x = \begin{pmatrix} 0 & 1 \\ 1 & 0 \end{pmatrix}, \sigma_y = \begin{pmatrix} 0 & -i \\ i & 0 \end{pmatrix}, \sigma_z = \begin{pmatrix} 1 & 0 \\ 0 & -1 \end{pmatrix}, \quad (\text{C.3})$$

as:

$$m_\xi = \text{Tr} \{ \sigma_\xi \mathbf{n} \}. \quad (\text{C.4})$$

The Pauli spin matrices also occur in the 4×4 α -matrices:

$$\alpha_x = \begin{pmatrix} 0 & \sigma_x \\ \sigma_x & 0 \end{pmatrix}, \alpha_y = \begin{pmatrix} 0 & \sigma_y \\ \sigma_y & 0 \end{pmatrix}, \alpha_z = \begin{pmatrix} 0 & \sigma_z \\ \sigma_z & 0 \end{pmatrix}. \quad (\text{C.5})$$

Bibliography

- [1] Werner Heisenberg. *The physical principles of the quantum theory*. Dover, 1930. Translated reprint.
- [2] E. Wigner and F. Seitz. *Physical Review*, 43:804, 1933.
- [3] N. W. Ashcroft and N. D. Mermin. *Solid State Physics*. Brooks/Cole, Thomson Learning, 1976.
- [4] J. M. Cowley. *Physical Review*, 77:669, 1950.
- [5] C. Zener. *Transactions AIME*, 203:619–630, 1955.
- [6] A V Ruban and I A Abrikosov. Configurational thermodynamics of alloys from first principles: effective cluster interactions. *Reports on Progress in Physics*, 71:046501, 2008.
- [7] T. B. Massalski et al., editors. *Binary Alloy Phase Diagrams*. America Society for Metals, Metals Park, OH, 1986.
- [8] D. Pines and P. Nozières. *Normal Fermi Liquids*, volume I of *The Theory of Quantum Liquids*. Westview Press - Advanced Book Program, 1989.
- [9] E. Wigner. On the interaction of electrons in metals. *Phys. Rev.*, 46:1002–1011, 1934.
- [10] K. Burke. The ABC of DFT. <http://chem.ps.uci.edu/~kieron/dft/book>, April 2007.
- [11] G. F. Giuliani and G. Vignale. *Quantum Theory of the Electron Liquid*. Cambridge University Press, 2005.
- [12] Richard D. Mattuck. *A guide to Feynman diagrams in the many-body problem*. Dover, 2nd edition, 1992.
- [13] A. B. Migdal. *Soviet Phys. JETP*, 5:333, 1957.
- [14] J. M. Luttinger. *Phys. Rev.*, 119:1153, 1960.

- [15] E. Daniel and S. H. Vosko. *Phys. Rev.*, 120:2041, 1960.
- [16] Simo Huotari, J. Aleksi Soininen, Tuomas Pytkänen, Keijo Hämäläinen, Arezki Issolah, Andrey Titov, Jeremy McMinis, Jeongnim Kim, Ken Esler, David M. Ceperley, Markus Holzmann, and Valerio Olevano. Momentum distribution and renormalization factor in sodium and the electron gas. *Phys. Rev. Lett.*, 105:086403, 2010.
- [17] P. Nozières. *Theory of Interacting Fermi Systems*. Westview Press - Advanced Book Program, 1997.
- [18] Takashi Miyake, Ferdi Aryasetiawan, and Masatoshi Imada. *Phys. Rev. B*, 80:155134, 2009.
- [19] I. M. Lifshitz. *Zh. Eksp. Teor. Fiz.*, 38:1569, 1960.
- [20] M. I. Katsnelson and Trefilov A. V. Naumov, I. I. *Phase Transitions*, 49:143–191, 1994.
- [21] L. D. Landau. The theory of a fermi liquid. *Soviet Physics JETP*, 3(6):920–925, 1957.
- [22] J. H. Van Vleck. *The Theory of Electric and Magnetic Susceptibilities*. Oxford University press, London, 1st edition, 1932. reprinted by Lowe & Brydone Ltd., London.
- [23] W. Gerlach and O. Stern. *Z. Physik A*, 9:353–355, 1922.
- [24] O. Stern. The method of molecular rays. Nobel lecture, December 12 1946. www.nobelprize.org, last accessed Dec. 2011.
- [25] Niels Bohr. Letter to Ralph Kronig. AIP: Niels Bohr library & archives, March 26 1926. http://www.aip.org/history/nbl/collections/goudsmit/colls/print/Box_59/Goudsmit59_48/Goudsmit59_480009.html, last accessed Dec. 2011.
- [26] A. Pais. *Physics Today*, 42:34, December 1989.
- [27] A. Wright. The spinning electron. *Nature Milestones: Spin*, page 57, March 2008.
- [28] Edmund C. Stoner. *Philosophical Magazine*, 48:719–736, 1924.
- [29] W. Pauli. *Z. Physik A*, 31:373–385, 1925.
- [30] W. Pauli. *Z. Physik A*, 31:765–783, 1925.
- [31] G. E. Uhlenbeck and S. A. Goudsmith. *Naturwissenschaften*, 17 October 1925. Reproduced in *Phys. Today* 29:43–48, 1976.
- [32] G. E. Uhlenbeck and S. Goudsmith. Spinning electrons and the structure of spectra. *Nature*, 117:264–265, 1926.

- [33] A. Rich and J. C. Wesley. *Rev. Mod. Phys.*, 44:250–283, 1972.
- [34] D. Hanneke, S. Fogwell Hoogerheide, and G. Gabrielse. *Phys. Rev. A*, 83:052122, 2011.
- [35] E. C. Stoner. *Philosophical Magazine*, 15:1018–1034, 1933.
- [36] J. C. Slater. Cohesion in monovalent metals. *Phys. Rev.*, 35:509–529, 1930.
- [37] H. Bruus and K. Flensberg. *Many-Body Quantum Theory in Condensed Matter Physics: An Introduction*. Oxford University Press, 2004.
- [38] E. C. Stoner. *Proceedings of the Royal Society A*, 165:372–414, 1938.
- [39] E. C. Stoner. *Rep. Prog. Phys.*, 11:43–112, 1947.
- [40] J. Kübler. *Theory of Itinerant Electron Magnetism*. London, 2000.
- [41] P. Mohn. *Magnetism in the Solid State*. Springer, 2003.
- [42] R. A. de Groot, F. M. Mueller, P. G. van Engen, and K. H. J. Buschow. *Phys. Rev. Lett.*, 50:2024–2027, 1983.
- [43] M. I. Katsnelson, V. Yu. Irkhin, L. Chioncel, A. I. Lichtenstein, and R. A. de Groot. Half-metallic ferromagnets: From band structure to many-body effects. *Rev. Mod. Phys.*, 80:315–378, 2008.
- [44] F. Heusler. *Verhandl. Deuts. Phys. Ges.*, 5:219, 1903.
- [45] F. Heusler et al. *Verhandl. Deuts. Phys. Ges.*, 5:220, 1903.
- [46] L. M. Sandratskii. *Phys. Rev. B*, 78:094425, 2008.
- [47] Igor Žutić, Jaroslav Fabian, and S. Das Sarma. *Rev. Mod. Phys.*, 76:323–410, 2004.
- [48] C. Hordequin, D. Ristiou, L. Ranno, and J. Pierre. *Eur. Phys. J. B*, 16:287, 2000.
- [49] E. Fermi. *Z. Phys.*, 60:320, 1930.
- [50] N. N. Greenwood and T. C. Gibb. *Mössbauer Spectroscopy*. Chapman and Hall Ltd, London, 1971.
- [51] J. F. Janak. *Phys. Rev. B*, 20:2206–2208, 1979.
- [52] P. C. Riedi. *Phys. Rev. B*, 20:2203–2205, 1979.
- [53] Lars Nordström and David J. Singh. *Phys. Rev. Lett.*, 76:4420–4423, 1996.
- [54] Elisabeth Sjöstedt and Lars Nordström. *Phys. Rev. B*, 66:014447, 2002.
- [55] Knöpfle. *J. Phys. F: Met. Phys.*, 14:2659–2671, 1984.

- [56] L Dobrzynski, R. J. Papoular, and Sakata M. *Journal of the Physical Society of Japan*, 65:255–263, 1996.
- [57] C. Kittel. *Introduction to Solid State Physics*. John Wiley & Sons, Inc., 7th edition, 1996.
- [58] Raquel Lizárraga, Lars Nordström, Lars Bergqvist, Anders Bergman, Elisabeth Sjöstedt, Peter Mohn, and Olle Eriksson. *Phys. Rev. Lett.*, 93:107205, 2004.
- [59] Raquel Lizárraga, Lars Nordström, Olle Eriksson, and John Wills. *Phys. Rev. B*, 78:064410, 2008.
- [60] K. Yosida. *Theory of Magnetism*. Springer, 1996.
- [61] T. Moriya. *Spin Fluctuations in Itinerant Electron Magnetism*. Springer-Verlag, 1985.
- [62] Daniel C. Mattis. *Phys. Rev.*, 151:278–279, 1966.
- [63] G Barnea and G Horwitz. *Journal of Physics C: Solid State Physics*, 6:738, 1973.
- [64] Conyers Herring and Charles Kittel. On the theory of spin waves in ferromagnetic media. *Phys. Rev.*, 81:869–880, 1951.
- [65] H. A. Mook, R. M. Nicklow, E. D. Thompson, and M. K. Wilkinson. *Journal of Applied Physics*, 40:1450–1451, 1969.
- [66] H. A. Mook and R. M. Nicklow. *Phys. Rev. B*, 7:336–342, 1973.
- [67] E. D. Thompson and H. A. Mook. Energy bands, stoner modes, and spin waves in iron. *Journal of Applied Physics*, 41:1227–1228, 1970.
- [68] P. Rhodes and E. P. Wohlfarth. *Proc. R. Soc. Lond. A*, 273:247–258, 1963.
- [69] E.M. Lifshitz and L. P. Pitaevskii. *Statistical Physics part 2*, volume 9 of *Landau and Lifshitz Course of Theoretical Physics*. Reed Educational and Professional Publishing Ltd, 1980.
- [70] M. Born and J. R. Oppenheimer. *Ann. Physik*, 84, 1927.
- [71] John P. Perdew and Stefan Kurth. Density functionals for non-relativistic coulomb systems in the new century. In *A Primer in Density Functional Theory*, chapter 1, pages 1–55. Springer, 2003.
- [72] D. M. Ceperley and B. J. Alder. *Phys. Rev. Lett.*, 45:566–569, 1980.
- [73] G. Ortiz, M. Harris, and P. Ballone. Zero temperature phases of the electron gas. *Phys. Rev. Lett.*, 82:5317–5320, 1999.
- [74] Jianwei Sun, John P. Perdew, and Michael Seidl. *Phys. Rev. B*, 81:085123, 2010.

- [75] J. P. Perdew, K. Burke, and Y. Wang. *Physical Review B*, 46:6671, 1992.
- [76] S. H. Vosko, L. Wilk, and M. Nusair. Accurate spin-dependent electron liquid correlation energies for local spin density calculations: a critical analysis. *Canadian Journal of Physics*, 58:1200, 1980.
- [77] J. P. Perdew and Alex Zunger. *Phys. Rev. B*, 23:5048–5079, 1981.
- [78] U. von Barth and L. Hedin. *J. Phys. C*, 5:1629, 1972.
- [79] M. Gell-Mann and K. A. Brueckner. *Physical Review*, 106:364, 1957.
- [80] W. Kohn. Nobel lecture: Electronic structure of matter — wave functions and density functionals. *Rev. Mod. Phys.*, 71:1253–1266, 1999.
- [81] P. Hohenberg and W. Kohn. *Phys. Rev.*, 136:B864–B871, 1964.
- [82] W. Kohn and L. J. Sham. *Phys. Rev.*, 140:A1133–A1138, 1965.
- [83] Mel Levy. *Proc. Natl. Acad. Sci. USA*, 76:6062–6065, 1979.
- [84] N. David Mermin. *Phys. Rev.*, 137:A1441–A1443, 1965.
- [85] L. M. Sandratskii. *Advances in Physics*, 47:19–160, 1998.
- [86] W. Kohn. *Phys. Rev. Lett.*, 76:3168–3171, 1996.
- [87] R. O. Jones and O. Gunnarsson. *Rev. Mod. Phys.*, 61:689, 1989.
- [88] S.-K. Ma and K. A. Brueckner. *Physical Review*, 165(18), 1968.
- [89] P. R. Antoniewicz and Leonard Kleinman. *Phys. Rev. B*, 31:6779–6781, 1985.
- [90] P. S. Svendsen and U. von Barth. *Phys. Rev. B*, 54:17402–17413, 1996.
- [91] K. Burke, J. P. Perdew, and Y. Wang. Derivation of a generalized gradient approximation: The PW91 density functional. In J. F. Dobson, G. Vignale, and P. Das Mukunda, editors, *Electronic Density Functional Theory: Recent Progress and New Directions*. Plenum Press, New York, 1998.
- [92] J. P. Perdew, K. Burke, and M. Ernzerhof. *Physical Review Letters*, 77:3865, 1996.
- [93] John P. Perdew, Adrienn Ruzsinszky, Gábor I. Csonka, Oleg A. Vydrov, Gustavo E. Scuseria, Lucian A. Constantin, Xiaolan Zhou, and Kieron Burke. *Phys. Rev. Lett.*, 100:136406, 2008.
- [94] John P. Perdew, Adrienn Ruzsinszky, Gábor I. Csonka, Oleg A. Vydrov, Gustavo E. Scuseria, Lucian A. Constantin, Xiaolan Zhou, and Kieron Burke. *Phys. Rev. Lett.*, 102:039902, 2009.
- [95] M. Ropo, K. Kokko, and L. Vitos. *Phys. Rev. B*, 77:195445, 2008.

- [96] R. Armiento and A. E. Mattsson. *Phys. Rev. B*, 72:085108, 2005.
- [97] Ann E. Mattsson, Rickard Armiento, and Thomas R. Mattsson. *Phys. Rev. Lett.*, 101:239701, 2008.
- [98] Ann E. Mattsson and Rickard Armiento. *Phys. Rev. B*, 79:155101, 2009.
- [99] R. Dreizler. Relativistic density functional theory. In *A Primer in Density Functional Theory*, chapter 3, pages 123–143. Springer, 2003.
- [100] Rajagopal and Callaway. *Physical Review B*, 7:1912, 1973.
- [101] A. K. Rajagopal. *J. Phys. C*, 11:L943, 1978.
- [102] A. H. MacDonald. *J. Phys. C*, 12:2977, 1979.
- [103] D D Koelling and B N Harmon. *Journal of Physics C: Solid State Physics*, 10:3107, 1977.
- [104] S. Pittalis, C. R. Proetto, A. Floris, A. Sanna, C. Bersier, K. Burke, and E. K. U. Gross. *Phys. Rev. Lett.*, 107:163001, 2011.
- [105] Vladimir I. Anisimov, Jan Zaanen, and Ole K. Andersen. *Phys. Rev. B*, 44:943–954, 1991.
- [106] A. G. Petukhov, I. I. Mazin, L. Chioncel, and A. I. Lichtenstein. *Phys. Rev. B*, 67:153106, 2003.
- [107] Erik R. Ylvisaker, Warren E. Pickett, and Klaus Koepernik. *Phys. Rev. B*, 79:035103, 2009.
- [108] V. Anisimov and Y. Izyumov. *Electronic Structure of Strongly Correlated Materials*. Springer, 2010.
- [109] A. I. Liechtenstein, V. I. Anisimov, and J. Zaanen. *Phys. Rev. B*, 52:R5467–R5470, 1995.
- [110] S. L. Dudarev, G. A. Botton, S. Y. Savrasov, C. J. Humphreys, and A. P. Sutton. *Phys. Rev. B*, 57:1505–1509, 1998.
- [111] F. Bloch. *Z. Phys.*, 52:555, 1928.
- [112] Hendrik J. Monkhorst and James D. Pack. *Phys. Rev. B*, 13:5188–5192, 1976.
- [113] L. M. Sandratskii. *Phys. Stat. Sol. B*, 135:167, 1986.
- [114] J. C. Slater. *Phys. Rev.*, 51:846–851, 1937.
- [115] J. C. Slater. *Phys. Rev.*, 92:603–608, 1953.
- [116] M. M. Saffren and J. C. Slater. *Phys. Rev.*, 92:1126–1128, 1953.

- [117] S. Cottenier. Density functional theory and the family of (L)APW-methods: a step-by-step introduction. http://www.wien2k.at/reg_user/textbooks, Instituut voor Kern- en Stralingsfysica, K.U.Leuven, Belgium, 2002. ISBN 90-807215-1-4.
- [118] O. Krogh Andersen. *Phys. Rev. B*, 12:3060–3083, 1975.
- [119] E Sjöstedt, L Nordström, and D.J Singh. *Solid State Communications*, 114:15–20, 2000.
- [120] Georg K. H. Madsen, Peter Blaha, Karlheinz Schwarz, Elisabeth Sjöstedt, and Lars Nordström. *Phys. Rev. B*, 64:195134, 2001.
- [121] P. Blaha, K. Schwarz, G. K. H. Madsen, D. Kvasnicka, and J. Luit. *WIEN2k, An Augmented Plane Wave + Local Orbitals Program for Calculating Crystal Properties*. Karlheinz Schwarz, Techn. Universität Wien, Austria, 2001. ISBN 3-9501031-1-2.
- [122] P. E. Blöchl. *Phys. Rev. B*, 50:17953–17979, 1994.
- [123] Peter Blöchl. *The LDA+DMFT approach to strongly correlated materials*, chapter 2: Theory and Practice of Density-Functional Theory. Forschungszentrum Jülich GmbH, Institute for Advanced Simulations, 2011.
- [124] G. Kresse and J. Hafner. *Phys Rev. B*, 47:558, 1994.
- [125] G. Kresse and J. Hafner. *Phys Rev. B*, 49:14251, 1994.
- [126] G. Kresse and J. Furthmüller. *Comput. Mat. Sci*, 6:15, 1996.
- [127] G. Kresse and J. Furthmüller. *Phys. Rev. B*, 54:11169, 1996.
- [128] G. Kresse and D. Joubert. *Phys. Rev. B*, 59:1758, 1999.
- [129] Georg Kresse, Martinj Marsman, and Jürgen Furthmüller. Vasp the guide. <http://cms.mpi.univie.ac.at/VASP>, 2011. Last accessed May, 2012.
- [130] J. Korringa. *Physica*, 13:392, 1947.
- [131] W. Kohn and N. Rostoker. *Phys. Rev.*, 94:1111–1120, 1954.
- [132] Lord Rayleigh. *Phil. Mag.*, 23:481, 1892.
- [133] B. A. Lippmann and Julian Schwinger. *Phys. Rev.*, 79:469–480, 1950.
- [134] R. Zeller, J. Deutz, and P. H. Dederichs. *Solid State Communications*, 44:993–997, 1982.
- [135] Richard M. Martin. *Electronic Structure: Basic Theory and Practical Methods*. Cambridge, 2004.
- [136] John. M. Wills, Mebarek Alouani, Per Andersson, Anna Delin, Olle Eriksson, and Oleksiy Grechnev. *Full-Potential Electronic Structure Method*. Springer, 2010.

- [137] Jan Zabloudil. *The full-potential screened KKR method*. PhD thesis, Technischen Universität Wien, 2000.
- [138] B. L. Gyorffy. *Phys. Rev. B*, 5:2382–2384, 1972.
- [139] N Papanikolaou, R Zeller, and P H Dederichs. *Journal of Physics: Condensed Matter*, 14:2799, 2002.
- [140] L. Vitos, H.L. Skriver, B. Johansson, and J. Kollár. *Computational Materials Science*, 2000.
- [141] O. K. Andersen, O. Jepsen, and G. Krier. Exact muffin-tin orbital theory. In *Lectures in Methods of Electronic Structure Calculations*. World Sci. Publ. Co, 1994.
- [142] Oleg E. Peil. *Theory of Disordered Magnets*. PhD thesis, Uppsala Universitet, 2009.
- [143] Levente Vitos. *Computational Quantum Mechanics for Materials Engineers: The EMTO Method and Applications*. Springer, 2007.
- [144] A. Svane and O. K. Andersen. 34:5512–5517, 1986.
- [145] L. Vitos, J. Kollár, and H. L. Skriver. *Phys. Rev. B*, 49:16694–16701, 1994.
- [146] Alex Zunger, S.-H. Wei, L. G. Ferreira, and James E. Bernard. *Phys. Rev. Lett.*, 65:353–356, 1990.
- [147] Paul Soven. *Phys. Rev.*, 156:809–813, 1967.
- [148] I.A. Abrikosov, Yu. H. Veklov, P.A. Korzhavyi, A.V. Ruban, and L.E. Shilkrot. *Solid State Communications*, 83:867, 1992.
- [149] A. V. Ruban and H. L. Skriver. Screened coulomb interactions in metallic alloys I: Universal screening in the atomic-sphere approximation. *Phys. Rev. B*, 66:024201, 2002.
- [150] A. V. Ruban, S. I. Simak, P. A. Korzhavyi, and H. L. Skriver. Screened coulomb interactions in metallic alloys II: Screening beyond the single-site and atomic-sphere approximations. *Phys. Rev. B*, 66:024202, 2002.
- [151] I. A. Abrikosov, A. M. N. Niklasson, S. I. Simak, B. Johansson, A. V. Ruban, and H. L. Skriver. *Phys. Rev. Lett.*, 76:4203–4206, 1996.
- [152] I. A. Abrikosov, S. I. Simak, B. Johansson, A. V. Ruban, and H. L. Skriver. *Phys. Rev. B*, 56:9319–9334, 1997.
- [153] Yang Wang, G. M. Stocks, W. A. Shelton, D. M. C. Nicholson, Z. Szotek, and W. M. Temmerman. *Phys. Rev. Lett.*, 75:2867–2870, 1995.
- [154] Oleg E. Peil, Andrei V. Ruban, and Börje Johansson. arXiv:1110.6354v1 [cond-mat.mtrl-sci], March 2012.

- [155] Antoine Georges, Gabriel Kotliar, Werner Krauth, and Marcelo J. Rozenberg. *Rev. Mod. Phys.*, 68:13–125, 1996.
- [156] Walter Metzner and Dieter Vollhardt. *Phys. Rev. Lett.*, 62:324–327, 1989.
- [157] P. W. Anderson. *Phys. Rev.*, 124:41–53, 1961.
- [158] Michel Ferrero and Olivier Parcollet. TRIQS: a Toolbox for Research in Interacting Quantum Systems. <http://ipht.cea.fr/triqs>.
- [159] Philipp Werner, Armin Comanac, Luca de’ Medici, Matthias Troyer, and Andrew J. Millis. *Phys. Rev. Lett.*, 97:076405, 2006.
- [160] E. Gull, P. Werner, O. Parcollet, and M. Troyer. 82:57003, 2008.
- [161] F. Lechermann, A. Georges, A. Poteryaev, S. Biermann, M. Posternak, A. Yamasaki, and O. K. Andersen. *Phys. Rev. B*, 74:125120, 2006.
- [162] L. V. Pourovskii, B. Amadon, S. Biermann, and A. Georges. *Phys. Rev. B*, 76:235101, 2007.
- [163] Markus Aichhorn, Leonid Pourovskii, Veronica Vildosola, Michel Ferrero, Olivier Parcollet, Takashi Miyake, Antoine Georges, and Silke Biermann. *Phys. Rev. B*, 80:085101, 2009.
- [164] Markus Aichhorn, Leonid Pourovskii, and Antoine Georges. *Phys. Rev. B*, 84:054529, 2011.
- [165] A. V. Ruban, P. A. Korzhavyi, and B. Johansson. *Phys. Rev. B*, 77:094436, 2008.
- [166] A I Liechtenstein, M I Katsnelson, and V A Gubanov. Exchange interactions and spin-wave stiffness in ferromagnetic metals. *Journal of Physics F: Metal Physics*, 14:L125, 1984.
- [167] M. Methfessel and J. Kübler. *J. Phys. F*, 12:141, 1982.
- [168] Michael Uhl and Jürgen Kübler. *Phys. Rev. Lett.*, 77:334–337, 1996.
- [169] A. V. Ruban, S. Khmelevskyi, P. Mohn, and B. Johansson. *Phys. Rev. B*, 75:054402, 2007.
- [170] B L Gyorffy, A J Pindor, J Staunton, G M Stocks, and H Winter. *Journal of Physics F: Metal Physics*, 15:1337, 1985.
- [171] A. V. Ruban, S. Shallcross, S. I. Simak, and H. L. Skriver. Atomic and magnetic configurational energetics by the generalized perturbation method. *Phys. Rev. B*, 70:125115, 2004.
- [172] F. Ducastelle and F. Gautier. *J. Phys. F: Met. Phys*, 6:2039, 1976.
- [173] WorldAutoSteel. *Advanced High Strength Steel (AHSS) Application Guidelines Version 4.0*, 2009.

- [174] U. Brück, G. Frommeyer, O. Grässel, L. W. Mayer, and A. Weise. *Steel Research*, 73:294, 2002.
- [175] B. Dieny, V. S. Speriosu, S. S. P. Parkin, B. A. Gurney, D. R. Wilhoit, and D. Mauri. *Phys. Rev. B*, 43:1297–1300, 1991.
- [176] J.C.S. Kools. *IEEE Transactions on Magnetics*, 32:3165–3184, 1996.
- [177] C. Mitsumata, A. Sakuma, and Fukamichi K. *IEEE Transactions on Magnetics*, 39:2738–2740, 2003.
- [178] Chiharu Mitsumata, Akimasa Sakuma, and Kazuaki Fukamichi. *Journal of the Physical Society of Japan*, 76:024704, 2007.
- [179] X.-D. Xiang. *Annu. Rev. Mater. Sci.*, 29:149, 1999.
- [180] Thomas Gebhardt. *Ab initio lattice stability and elastic properties of Fe-Mn based alloys*. PhD thesis, RWTH Aachen University, 2012. Materials Chemistry Dissertation No.: 15 (2012).
- [181] Robert C. O’Handley. *Modern Magnetic Materials: Principles and Applications*. John Wiley & Sons, Inc., 2000.
- [182] Stuart S. P. Parkin, Masamitsu Hayashi, and Luc Thomas. *Science*, 320:190–194, 2008.
- [183] J.S. Kouvel and J.S. Kasper. Long-range antiferromagnetism in disordered Fe—Ni—Mn alloys. *Journal of Physics and Chemistry of Solids*, 24(4):529 – 536, 1963.
- [184] H. Umebayashi and Y. Ishikawa. *Journal of the Physical Society of Japan*, 21(7):1281, 1966.
- [185] Y. Endoh and Y. Ishikawa. *Journal of the Physical Society of Japan*, 30(6):1614, 1971.
- [186] P. Bisanti et al. *J. Phys. F: Met. Phys*, 17:1425–1435, 1987.
- [187] S. J. Kennedy and T. J. Hicks. *J. Phys. F: Met. Phys*, 17:1599–1604, 1987.
- [188] S. Kawarazaki, Y. Sasaki, K. Yasuda, T. Mizusaki, and A. Hirai. The triple-q-spin-density wave in the face-centred cubic antiferromagnetic Fe₅₄Mn₄₆ alloy. *Journal of Physics: Condensed Matter*, 2(26):5747–5752, 1990.
- [189] G. Malcolm Stocks, W. A. Shelton, Thomas C. Schulthess, Balazs Újfalussy, W. H. Butler, and A. Canning. *J. Appl. Phys*, 91(10):7355–7357, 2002.
- [190] S. Mankovsky, G. H. Fecher, and H. Ebert. *Phys. Rev. B*, 83:144401, 2011.
- [191] W. Stamm, H. Zäres, M. Acet, K. Schletz, and E. F. Wassermann. *Journal de Physique*, C8:315–316, december 1988.

- [192] M. Cankurtaran, G. A. Saunders, P. Ray, Q. Wang, U. Kawald, J. Pelzl, and H. Bach. *Phys. Rev. B*, 47:3161–3170, 1993.
- [193] T. Schneider, M. Acet, B. Rellinghaus, E. F. Wassermann, and W. Pepperhoff. *Phys. Rev. B*, 51:8917–8921, 1995.
- [194] J. Kubler, K H Hock, J Sticht, and A R Williams. *J. Phys F: Met. Phys.*, 18(3):469–483, 1988.
- [195] Ann E. Mattsson, Rickard Armiento, Peter A. Schultz, and Thomas R. Mattsson. *Phys. Rev. B*, 73:195123, 2006.
- [196] I. A. Abrikosov, A. E. Kissavos, F. Liot, B. Alling, S. I. Simak, O. Peil, and A. V. Ruban. *Phys. Rev. B*, 76:014434, 2007.
- [197] Hualei Zhang, Marko P Punkkinen, Börje Johansson, and Levente Vitos. *Physical Review B*, 85, 2012.
- [198] G. B. Olson and M. Cohen. *Metall. Trans. A*, 7:1897, 1976.
- [199] O. Grassel, L. Kruger, Frommeyer G., and L. W. Meyer. *Int. J. Plast.*, 16:1391, 2000.
- [200] C. S. Wang and J. Callaway. *Phys. Rev. B*, 15:298–306, 1977.
- [201] J. Callaway and C. S. Wang. *Phys. Rev. B*, 16:2095–2105, 1977.
- [202] S. Blügel, H. Akai, R. Zeller, and P. H. Dederichs. *Phys. Rev. B*, 35:3271–3283, 1987.
- [203] H Ebert, P Strange, and B L Gyorffy. *Journal of Physics F: Metal Physics*, 18(7):L135, 1988.
- [204] H. Ebert and H. Akai. *Hyperfine Interactions*, 78:361–375, 1993.
- [205] Marco Battocletti, H. Ebert, and H. Akai. *Phys. Rev. B*, 53:9776–9783, 1996.
- [206] L. Severin, M. Richter, and L. Steinbeck. *Phys. Rev. B*, 55:9211–9214, 1997.
- [207] M. Battocletti and H. Ebert. *Phys. Rev. B*, 64:094417, 2001.
- [208] H Ebert, H Winter, B L Gyorffy, D D Johnson, and F J Pinski. *Journal of Physics F: Metal Physics*, 18:719, 1988.
- [209] Diana Guenzburger and Joice Terra. *Phys. Rev. B*, 72:024408, 2005.
- [210] R. Coehoorn. *J. Magn. Mag. Mat.*, 159:55–63, 1996.
- [211] A. V. Ponomareva, A. V. Ruban, N. Dubrovinskaia, L. Dubrovinsky, and I. A. Abrikosov. *Applied Physics Letters*, 94:181912, 2009.
- [212] T. Takahashi and W. A. Basset. *Science*, page 483, 145.

- [213] G. Cort, R. D. Taylor, and J. O. Willis. *Journal of Applied Physics*, 53:2064–2065, 1982.
- [214] Gerd Steinle-Neumann, Lars Stixrude, and Ronald E. Cohen. *Phys. Rev. B*, 60:791–799, 1999.
- [215] Gerd Steinle-Neumann, R E Cohen, and Lars Stixrude. *Journal of Physics: Condensed Matter*, 16:S1109, 2004.
- [216] A. B. Papandrew, M. S. Lucas, R. Stevens, I. Halevy, B. Fultz, M. Y. Hu, P. Chow, R. E. Cohen, and M. Somayazulu. *Phys. Rev. Lett.*, 97:087202, 2006.
- [217] V. Thakor, J. B. Staunton, J. Poulter, S. Ostanin, B. Ginatempo, and Ezio Bruno. *Phys. Rev. B*, 67:180405, 2003.
- [218] T. Hannesson and S. M. Blinder. *International Journal of Quantum Chemistry*, XV:7–14, 1979.
- [219] S. Fernbach. *Rev. Mod. Phys.*, 30, 1958.
- [220] L. Dubrovinsky, N. Dubrovinskaia, O. Narygina, I. Kantor, A. Kuznetsov, V. B. Prakapenka, L. Vitos, B. Johansson, A. S. Mikhaylushkin, S. I. Simak, and I. A. Abrikosov. *Science*, page 1880, 2007.
- [221] S. Tateno, K. Hirose, Y. Ohishi, and Y. Tatsumi. *Science*, 330:339, 2010.
- [222] L. V. Pourovskii, T. Miyake, S. I. Simak, A. V. Ruban, L. Dubrovinsky, and I. A. Abrikosov. arXiv:1204.3954v1 [cond-mat.str-el], April 2012.
- [223] J. H. Wijnngaard, C. Haas, and R. A. de Groot. *Phys. Rev. B*, 45:5395–5405, 1992.
- [224] C. Nordling and J. Österman. *Physics Handbook for Science and Engineering*. Studentlitteratur, 6th edition, 1999.

Index

Symbols	
1Q, 2Q, 3Q	23

A

a.u.	111
AFM	23
AM05	46
AMF	73
APW	54
ASA	23

B

bcc	4
BZ	53

C

C1 _b	19
CA	37
CPA	65
CT-QMC	71

D

DC	51
DFT	41
DLM	78
DMFT	69
DOS	17

E

ECI	80
EDX	105
EMTO	60
ETT	14

F

fcc	4
-----------	---

FCD	63
FM	23

G

GEA	45
GGA	45
GIXRD	105

H

Ha	111
hcp	4
HMFM	19

K

KKR	58
-----------	----

L

L2 ₁	19
L(S)DA	45
LAPW	55
LDA+DMFT	69
LIZ	67
LKG(M)	76
lo	55
LSGF	67

M

MT	54, 60
----------	--------

P

PAW	55
PBE	45
PBEsol	45
PhD	xi
PW	37

PW91.....	45
PZ.....	37

Q

QMC	71
-----------	----

R

RPA	37
-----------	----

S

SDFT.....	41
SeRC	xii
SGPM.....	80
SIC	51
SQS	64
SRL	xii
SSF	xii

T

TRIP	85
TRIQS.....	73
TWIP	85

V

VASP	58
VWN	37

W

Wien2k	55
WS	4